

OKINAWA INSTITUTE OF SCIENCE AND TECHNOLOGY  
GRADUATE UNIVERSITY

Thesis submitted for the degree

Doctor of Philosophy

---

# Atom-light interactions via evanescent fields

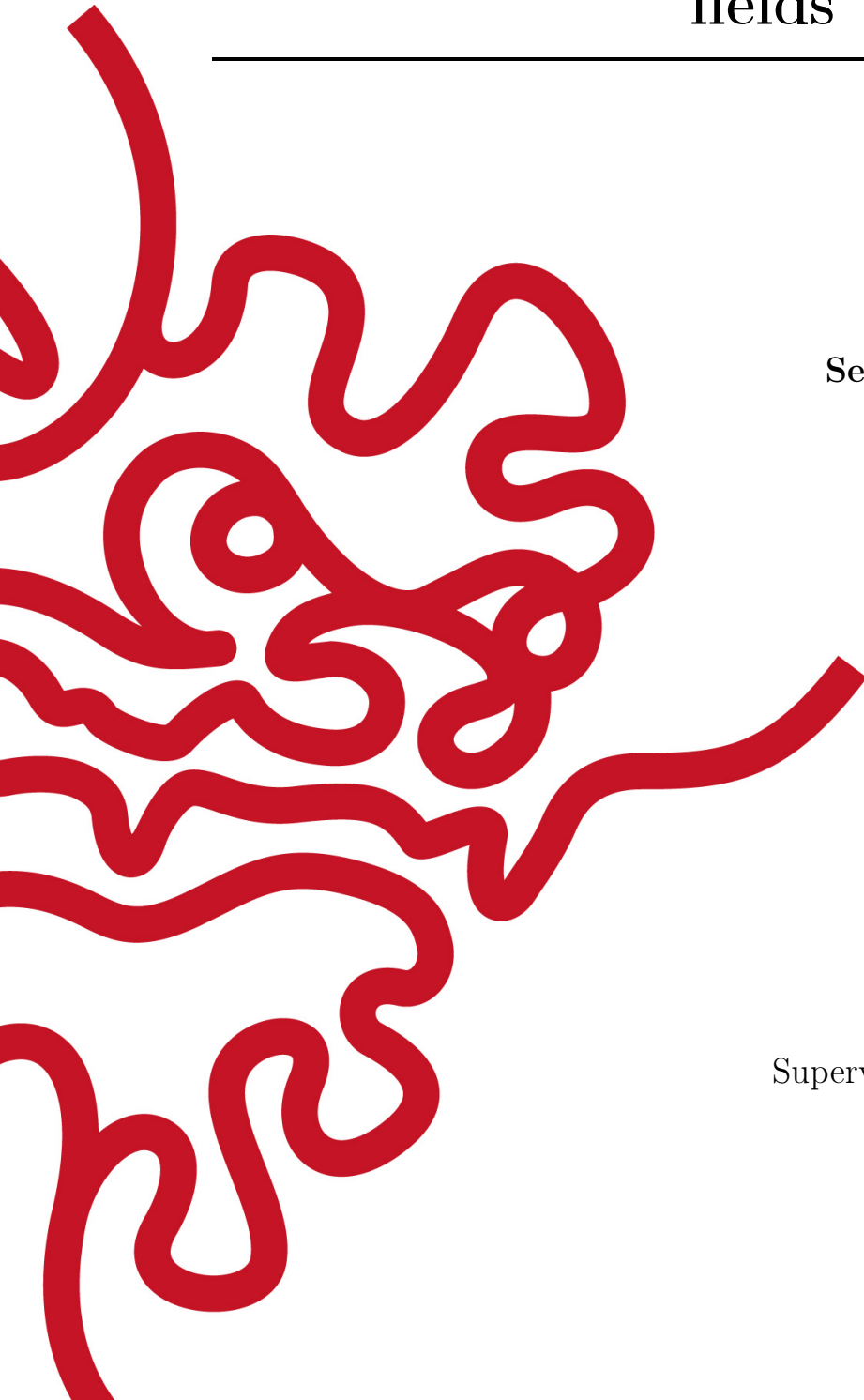
---

by

Seyedeh Sahar Seyed Hejazi

Supervisor: **Prof. Thomas Busch**

April 2021





# Declaration of Original and Sole Authorship

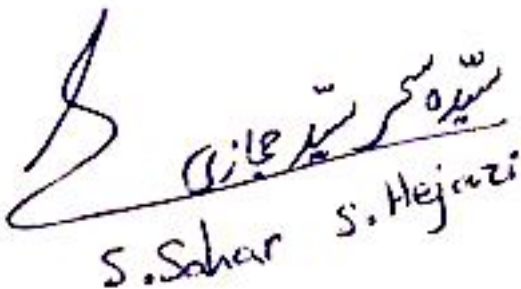
I, Seyedeh Sahar Seyed Hejazi, declare that this thesis entitled *Atom-light interactions via evanescent fields* and the data presented in it are original and my own work.

I confirm that:

- No part of this work has previously been submitted for a degree at this or any other university.
- References to the work of others have been clearly acknowledged. Quotations from the work of others have been clearly indicated, and attributed to them.
- In cases where others have contributed to part of this work, such contribution has been clearly acknowledged and distinguished from my own work.
- None of this work has been previously published elsewhere, with the following exceptions:
  - The work presented in Chapter 4 has been published as Phys. Rev. A **96**, 043859 (2017).
  - The work presented in Chapter 5 has been published partly as Phys. Rev. A **97**, 063849 (2018) and partly as New J. Phys. **20**, 093031 (2018).
  - The work presented in Chapter 6 has been published as Phys. Rev. A **102**, 053309 (2020).

Date: April 2021

Signature:



سید سحر سید هجازی  
S. Sahar S. Hejazi



# Abstract

Recently developed techniques to operate, control and measure atomic systems on the micro- and nano-meter scale have created a tremendous interest in exploring how the presence of surfaces affects their quantum properties. This is partly driven by the interest to explore further fundamental physics, but on the practical side, atom-chips and other nano-scale devices are poised to become important in our daily lives. In this thesis, I present results obtained by studying how an evanescent field in the vicinity of a dielectric medium affects various quantum systems, namely one and two atom systems, as well as multi-component Bose-Einstein condensates.

An evanescent field corresponds to an exponentially decaying mode above a surface, which emerges due to propagation of an electromagnetic wave inside a confined dielectric medium, such as a flat half-plane, an optical nano-fiber, or a prism. By bringing atoms close to the surface, the coupling to the evanescent field can strengthen the coupling between the atoms, resulting in multiple effects on their properties: frequency shifts can appear, emission rates can be modified and the dipole-dipole interaction between atoms can be enhanced.

In the first project presented in this thesis, I show that the decay rate of two atoms near a flat dielectric surface is different compared to free space and can have oscillatory decaying behavior. This includes directional propagation of information between the atoms with a strength depending on the orientation of the two electric dipole moments, and on the relative location of the atoms to one another and to the surface of the dielectric medium. I also discuss the modification of the spontaneous emission rate when a multi-level atom is placed in the vicinity of an optical nano-fiber. Here the modifications do not only depend on the optical modes of the fiber, but also on the magnetic sub-levels and orientation of the electric dipole moment of the atom.

A very interesting feature of atom-fiber systems is the possibility for spontaneous emission to be chiral. This effect again depends on the form of the available modes of the fiber and the orientation of electric dipole moment of the atom. In a second project I show that chiral emission also leads to a chiral recoil force on the atom and present a closed form expression for it. I then extend my studies to go beyond small systems and consider Bose-Einstein condensates of neutral atoms in the mean field limit. Exposing such systems to evanescent fields can be described as exposure to an artificial gauge field and be used to induce spatially inhomogeneous rotation into the condensate. In this part of the thesis, I show how localised rotation can affect the miscible to immiscible phase transition in two-component systems.



# Acknowledgments

I would like to thank my supervisor, Thomas Busch, who has been very supportive since the beginning. He was so patient over last few years and guided me through my studies. I will forever be grateful to him. I wish one day, I will become someone that he can be proud of.

I really appreciate all the generous help and support from my kind and caring mother who endured my absence; My motivated, determined and very positive father who sadly departed before I could finish my studies; My cute little brother Sina who I missed his wedding by one day and when he had Vala-kocholoo; My kind and caring friend, Alemeh, who was happy to eat sushi with me against her will and invited Seyed to have Matcha latte to make her happy; My loving and caring cousins who laughed with me and stood with me in my darkest times: Zahra, Shirin, Shayan, Vikki-joon and captain Mohamad; My affable and attentive friends who always been there for me, Priscila, Leilee, Rike, Amine and Florian; My odd friend Pedro who was always listening to me and reminded me why I need to stand on my feet again and finish my battle; All my friends across the globe: Loretta, Laura, Juan, Tayebah, Matthew, Max, Alan-chan, Ivan, Adi, Shachiko-chan, Albert, Angela, Arthur, Seb, Sandrine, Rux, Jing, Bijita, William, Kim and who are in my heart; OIST staff and all of my colleagues specially Juan, Rashid and Fam.

All projects presented below were designed and developed in close collaboration and with the guidance of my supervisor Prof. Thomas Busch. The studies related to the characteristic feature of atoms in the vicinity of an optical nanofiber, which are presented in Chapters 3 and 4 originated from ideas by Dr. Fam Le Kien and were strongly guided by him. All other collaborators are also co-authors of the papers presented here and my specific contributions to each project are detailed in the relevant chapters.





# Abbreviations

BEC	Bose–Einstein Condensate
TCBEC	Two Component Bose–Einstein Condensate
TF	Thomas-Fermi
GPE	Gross-Pitaevskii Equations
FFT	Fast Fourier Transform
TCGPE	Two Component Gross-Pitaevskii Equations



# Nomenclature

$c$	Speed of light ( $2.997\,924\,58 \times 10^8 \text{ ms}^{-1}$ )
$\hbar$	Planck constant ( $1.054\,572\,66 \times 10^{-34} \text{ Js}$ )
$Z_0$	Impedance of free space ( $376.730\,313\,461 \text{ } \Omega$ )
$\mu_0$	Permeability of free-space ( $4\pi \times 10^{-7} \text{ Hm}^{-1}$ )
$\epsilon_0$	Permittivity of free-space ( $1/\mu_0 c^2$ )



*Where symmetry breaks, maths ends and  
physics starts!*  
**To my father...**



# Published articles

- F. Le Kien, S. Sahar S. Hejazi, Th. Busch, V. G. Truong, and S. Nic Chormaic. Channeling of spontaneous emission from a multi-level atom into a nano-fiber, *Phys. Rev. A* **96**, 043859 (2017).
  - This work was done in close collaboration with Dr. Fam Le Kien, who is a staff scientist in the Quantum Systems Unit. Since I was familiar with the mode function method for a system consisting of atoms and a dielectric medium, I contributed to the analytical calculations, including the calculations of the decay rates of the atom into the fundamental and higher order modes. In addition, I investigated the possibility of asymmetric spontaneous emission rates for a multi-level atom. I also checked some of the limits to make sure that the obtained results are valid, since I wrote codes in MATLAB for a single atom in the vicinity of a flat dielectric surface. This easily allowed me to check the limit when the radius of fiber is large enough for atom to not experience the curvature of the fiber. Throughout the project, I was involved in all discussions and in the preparation of the published manuscript.
- F. Le Kien, D. F. Kornovan, S. Sahar S. Hejazi, V. G. Truong, M. I. Petrov, S. Chormaic, and Th. Busch. Force of light on a two-level atom near an ultrathinoptical fiber. *New J. Phys.* **20**, 093031 (2018), and
- F. Le Kien, S. Sahar S. Hejazi, V. G. Truong, S. Nic Chormaic, and Th. Busch. Chiral force of guided light on an atom. *Phys. Rev. A* **97**, 063849 (2018).
  - These two projects were carried out in close collaboration with Dr. Fam Le Kien. For the study using the mode function method, I carried out the analytical calculations for the force and the comparisons between the forward and backward forces to determine the chirality of the system. Since the mode function method has limitations and does not allow one to calculate the force in all directions, I then switched to using the Green's function method. In this second part of the project I performed the analytical calculations that enabled the construction of the mathematical model as well as the detailed comparisons between the two methods. I was involved in all discussions at all stages of these two project and also in the writing of the manuscripts.

- S. Sahar S. Hejazi, J. Polo, R. Sachdeva, and Th. Busch. Symmetry breaking in binary Bose-Einstein condensates in the presence of an inhomogeneous artificial gauge field. *Phys. Rev. A* **102**, 053309 (2020).
  - For this study, I carried out all the numeric calculations related to the coupled Gross-Pitaevskii equations for the realistic setup and for the toy model. Since I was conducting the main part of project, I was fully involved in developing the project, interpreting the results and writing the manuscript.



# Contents

<b>Declaration of Original and Sole Authorship</b>	<b>iii</b>
<b>Abstract</b>	<b>v</b>
<b>Acknowledgment</b>	<b>vii</b>
<b>Abbreviations</b>	<b>ix</b>
<b>Nomenclature</b>	<b>xi</b>
<b>Publications</b>	<b>xv</b>
<b>Contents</b>	<b>xvii</b>
<b>List of Figures</b>	<b>xix</b>
<b>Introduction</b>	<b>1</b>
<b>1 Mathematical methods</b>	<b>7</b>
1.1 Maxwell's equations and electromagnetic fields . . . . .	7
1.2 Mode function method . . . . .	8
1.2.1 Electromagnetic field in the presence of a dielectric medium . .	8
1.2.2 Boundary conditions and Fresnel relation . . . . .	9
1.2.3 Interaction between atoms and vacuum fields . . . . .	11
1.3 Guided modes of a step-index optical fiber . . . . .	11
1.3.1 TE modes . . . . .	15
1.3.2 TM modes . . . . .	16
1.3.3 Hybrid modes . . . . .	17
1.3.4 Radiation modes of an optical fiber . . . . .	19
1.4 Green's function method . . . . .	20
1.4.1 Green's tensor of an optical fiber . . . . .	22
<b>2 Cooperative behavior of two atoms</b>	<b>25</b>
2.1 Quantization of the EM field near a dielectric surface . . . . .	26
2.2 Spontaneous emission rate . . . . .	28
2.2.1 Spontaneous emission into the evanescent mode . . . . .	29

2.2.2	Spontaneous emission into the radiation mode . . . . .	31
2.3	Cooperative angular density . . . . .	32
2.4	Asymmetry of collective spontaneous emission . . . . .	37
2.4.1	Asymmetry of spontaneous emission into evanescent modes . . . . .	37
2.4.2	Asymmetry of spontaneous emission into radiation modes . . . . .	39
2.5	Conclusions . . . . .	41
<b>3</b>	<b>"Channeling of spontaneous emission from a multi-level atom into a nanofiber" originally published as [1]</b>	<b>43</b>
3.1	introduction . . . . .	43
3.2	Mathematical model of a multi-level atom in the vicinity of an optical nanofiber . . . . .	44
3.3	Spontaneous emission of the atom . . . . .	46
3.4	Publication . . . . .	47
3.5	Summary and conclusions . . . . .	47
<b>4</b>	<b>"Chiral force of guided light on an atom" originally published as [2, 3]</b>	<b>49</b>
4.1	Introduction . . . . .	49
4.2	Model, Hamiltonian and optical force of light on an atom . . . . .	50
4.3	Publication . . . . .	53
4.4	Summary and conclusions . . . . .	53
4.5	My contributions . . . . .	54
<b>5</b>	<b>"Symmetry breaking in binary Bose-Einstein condensates" originally published as [4]</b>	<b>55</b>
5.1	Introduction . . . . .	55
5.2	Mathematical model and artificial gauge fields . . . . .	56
5.3	Publication . . . . .	58
5.4	Results and conclusions . . . . .	58
	<b>Conclusion</b>	<b>59</b>
	<b>Bibliography</b>	<b>61</b>

# List of Figures

1	Schematic illustration of (a) a standard optical fiber with the core and cladding; (b) examples of multi-mode and single-mode fibers with their refractive index profiles and a sketch of the light path through them, reprinted from [5]; (c) schematic of a tapered optical nano-fiber where the core has vanished at the waist due to tapering, reprinted from [6]. .	3
2	Schematic of a prism configuration which is embedded in a typical near-field scanning optical microscopy setup. Around the critical angle, counter propagating beams, which meet at the surface of the prism, create an interference pattern in the evanescent field. By bringing particles close to the surface of the prism, they can be trapped in the evanescent field and can be observed with the Microscope Objective. Reprinted from [7]. . . . .	4
1.1	Schematic of all possible beam propagations at a dielectric surface. (a) The propagated field inside of the dielectric medium (red arrow) gets fully reflected at the interface between the vacuum and dielectric surface (dashed blue arrow). (b) The same as (a), however, since the angle is greater than critical angle for complete reflection, the propagating beam inside the dielectric medium is partially reflected and partially transmitted (dashed blue arrows). (c) The field propagates in free space (red arrow) and is partially reflected and transmitted at the surface of the dielectric medium (blue dashed arrows). Figure reproduced from [8].	10
1.2	Schematic of the Cartesian and cylindrical coordinate systems used for an optical nanofiber setup. The radius of the fiber is given by $a$ . . . . .	12
1.3	(a) Bessel functions of first kind, $J_l(x)$ and (b) modified Bessel functions of second kind, $K_l(x)$ . . . . .	13
1.4	Schematic plot of the mode pattern for the $TE_{01}$ mode in the azimuthal plane. The first plot on the left represents the electric field (full lines), the middle plot represents the magnetic field (dashed lines), and the one on the right represents the $TE_{01}$ mode. Figure taken from [9]. . . . .	16
1.5	Schematic plot of the mode pattern for $TM_{01}$ mode in the azimuthal plane. The first plot on the left represents the electric field (full lines), the middle plot represents the magnetic field (dashed lines), and the one on the right represents the $TE_{01}$ mode. Graph taken from [9]. . . . .	17

- 1.6 Examples of hybrid modes: the plots in the left column represent the electric field (solid lines), the ones in the middle column represent the magnetic field (dotted lines) and the column on the right shows the full hybrid modes. Figure taken from [9]. . . . . 18
- 2.1 Schematic of two neutral atoms in the vicinity of a flat dielectric surface. The atoms are located in the positive half-space,  $x > 0$  at  $\mathbf{r}_A$  and  $\mathbf{r}_B$ . The projection of the vacuum field vector  $\mathbf{K}$  onto the interface is characterized by the angle  $\varphi$ . . . . . 27
- 2.2 Absolute values of the cooperative angular densities  $|F_{\text{evan}}^{(AB)}|$  and  $|F_{\text{rad}}^{(AB)}|$  of the spontaneous emission into the evanescent and radiation modes for atoms with the electric dipole moments  $u_A$  and  $u_B$ . The atoms are separated by 200 nm from each other, and the atom-interface distance is  $x_A = x_B = 200$  nm. (I)  $\mathbf{u}_A = \mathbf{u}_B = \hat{x}$ , (II)  $\mathbf{u}_A = \mathbf{u}_B = \hat{z}$ , (III)  $\mathbf{u}_A = \mathbf{u}_B = \frac{1}{\sqrt{2}}(\hat{x} + \hat{z})$ , and (IV)  $\mathbf{u}_A = \mathbf{u}_B = \frac{1}{\sqrt{2}}(\hat{x} + i\hat{z})$ . (a) Absolute values of the angular density of the collective decay coefficient into the evanescent modes, (b) into the radiation modes, (c) the projection of the angular densities into the  $\kappa_y$ , and (d)  $\kappa_z$  direction. . . . . 33
- 2.3 Coefficients of spontaneous emission into the evanescent modes  $\gamma_{\text{evan}}^{(AB)}/\gamma_0$  (blue solid line), the radiation modes  $\gamma_{\text{rad}}^{(AB)}/\gamma_0$  (red dashed-dotted line) and their sum  $\gamma^{(AB)}/\gamma_0$  (black dashed line) as a function of atom-interface distance for varying interatomic separation (a)  $|z_1 - z_2| = 0$  nm, (b)  $|z_1 - z_2| = 50$  nm, (c)  $|z_1 - z_2| = 100$  nm and (d)  $|z_1 - z_2| = 150$  nm and varying orientation of dipole moments (I)  $\mathbf{u}_A = \mathbf{u}_B = \hat{x}$ , (II)  $\mathbf{u}_A = \mathbf{u}_B = \hat{z}$ , (III)  $\mathbf{u}_A = \mathbf{u}_B = \frac{1}{\sqrt{2}}(\hat{x} + \hat{z})$ , and (IV)  $\mathbf{u}_A = \mathbf{u}_B = \frac{1}{\sqrt{2}}(\hat{x} + i\hat{z})$ . 35
- 2.4 Coefficients of spontaneous emission into the evanescent (blue solid lines) and radiation (red dashed-dotted lines) modes for  $x_A = x_B = 200$  nm as a function of the inter-atomic separation  $|z_A - z_B|$  (I)  $\mathbf{u}_A = \mathbf{u}_B = \hat{x}$ , (II)  $\mathbf{u}_A = \mathbf{u}_B = \hat{z}$ , (III)  $\mathbf{u}_A = \mathbf{u}_B = \frac{1}{\sqrt{2}}(\hat{x} + \hat{z})$  and (IV)  $\mathbf{u}_A = \mathbf{u}_B = \frac{1}{\sqrt{2}}(\hat{x} + i\hat{z})$ . 36
- 2.5 Asymmetry parameters for cooperative spontaneous emission into the evanescent modes  $\zeta_{\text{evan}}$  (blue dashed line), radiation modes  $\zeta_{\text{rad}}$  (red dash-dotted line), and both type of modes  $\zeta$  (black solid line) as a function of atom-interface distance  $x_A = x_B = 0 - 800$  nm for different values of inter-atomic distance (a)  $|z_A - z_B| = 0$  nm, (b)  $|z_A - z_B| = 100$  nm, (c)  $|z_A - z_B| = 500$  nm, and (d)  $|z_A - z_B| = 1000$  nm. The atomic dipole moment matrix elements for both atoms are taken as complex quantities  $\mathbf{u}_A = \mathbf{u}_B = \frac{1}{\sqrt{2}}(\hat{x} + i\hat{z})$ . . . . . 41

- 
- 3.1 (a) Schematic plot of the atom in the vicinity of an optical nanofiber. The atom interacts with the guided and radiation modes via its electric dipole moment. The fiber-based Cartesian coordinate system  $\{x, y, z\}$  and also the corresponding cylindrical coordinate system  $\{r, \varphi, z\}$ , where  $r$  and  $\varphi$  are the polar coordinates in the transverse  $x - y$  plane of the fiber, are indicated. The energy levels of the atom are specified in a Cartesian coordinate system  $\{x_Q, y_Q, z_Q\}$ , where  $z_Q$  is the direction of the quantization axis. (b) Schematic of the hyperfine-structure of the atomic levels of the  $5P_{3/2}$  and  $5S_{1/2}$  states of the  $^{87}\text{Rb}$  atom and the allowed transitions. These levels are specified with respect to the quantization axis  $z_Q$  [1]. The fiber has radius of  $a$  and refractive index of  $n_1$ . . . . . 45
- 5.1 Schematic representation of a two-component BEC trapped in a potential  $V(x, z)$  (geometry indicated by the dashed circle) just above the surface of a dielectric prism.[4] . . . . . 57



# Introduction

Quantum science and its practical applications have seen significant progress recently. This has partly been driven by, and led to, great enthusiasm in the area of atomic, molecular, and optical (AMO) physics to design, manufacture and employ quantum hybrid systems. One example of such systems is trapped neutral atoms in the vicinity of miniaturized devices [10–14], where due to close proximity, the interactions between the atoms and the surface fields are enhanced and become dominant. Such tightly integrated systems, which are also desirable to fulfil the increased stability requirements of potential commercial applications, pose the need for the careful study of effects stemming from the van der Waals or surface-induced force [15–26], the quantum friction forces [27–32] and also the Purcell effect [33]. All these phenomena result from the fact that fluctuations of the vacuum field have a measurable effect on macroscopic and microscopic objects. The vacuum field [34–37] can also be used to explain other fundamental physical phenomena, such as the natural decay of an excited atom [38–40] and shifts of the atomic energy levels [41, 42]. Implementing boundary conditions on optical and vacuum fields leads to new induced forces on particles close to their surfaces [43] and in this thesis I explore how the presence of a dielectric medium affects few-body and many-body quantum systems.

Neutral atoms which are located in the vicinity of a dielectric substrate experience certain changes in their properties, for instance frequency shifts of the atomic transitions and changes in the spontaneous decay rate. In addition they can also experience optical forces from guided light. For cases with more than one atom, the dielectric medium also modifies the coupling strength between atoms.

To study the effect of the dielectric medium on atomic properties, I consider a perfect dielectric medium and neutral atoms with an electric dipole moment. These atoms interact with one another through the various optical modes of dielectric medium. In many cases the internal structure of the atoms can be reduced to a two-level system, and the electric dipole moment of the atom is allowed to have complex matrix dipole elements [44], in contrast to previous studies [45, 46]. The presence of a dielectric medium then profoundly affects the spontaneous emission rate, and in particular can lead to chirality (unidirectional propagation) of spontaneously emitted and absorbed light. This effect has recently been observed experimentally [12, 47].

Finally, the inhomogeneous structure of the evanescent field can also act as an effective artificial gauge field for many-body systems in the mean-field limit. For an atomic Bose-Einstein condensate close to a surface these fields can therefore be used to induce local rotation and create systems with inhomogeneously distributed vorticity. This has been achieved by exploring how the emerging evanescent field from a dielectric prism

could affect an ultra-cold atomic gases such as Bose-Einstein condensate. These studies lead to the possibility of creating line vortices in the miscible regime and the symmetry breaking of two-components Bose-Einstein condensate in the phase separation regime.

In the following section, I introduce the different systems that I will use in my work and give a brief overview of the area of cold atoms close to dielectric surfaces.

## Evanescent fields

Electromagnetic fields are produced by moving electric charges, and can freely propagate in various media as continuous wavelike fields. However, an electromagnetic field propagating inside of a dielectric medium also creates a field at the surface of the medium, that does not propagate but exponentially decays. The energy of this field is concentrated in the vicinity of the surfaces and there is no net flow of energy. Fields propagating in devices of wavelength or sub-wavelength width show distinctive properties in comparison to fields propagating in ordinary optical devices. In particular, the evanescent near-field modes at the surface become much more prominent, which is one of the main reasons for the use of optical nano-fibers [47–51]. In many experimental settings, these evanescent fields can be neglected due to their exponentially decaying amplitude away from the surface. However, the ability to place atoms in the vicinity of these devices allows the atoms to efficiently couple to the evanescent fields, which can lead to interesting induced interactions between the atoms themselves. In the next section, I introduce two optical devices that I have considered in my study.

## Optical nano-fibers

Standard optical fibers are made of two coaxial cylindrical silica materials (see Fig. 1(a)), known as the core and cladding, with refractive indices of  $n_1$  and  $n_2$  respectively, where  $n_1 > n_2$  to satisfy the propagation condition for light passing through the fiber. The fiber diameter and the refractive index difference between the core and cladding determine the optical properties of a fiber. Some examples of standard optical fibers, such as single-mode and multi-mode fibers, are shown in Fig. 1(b). Optical fibers with step index profiles for the core and the cladding are widely used in telecommunications and have many other applications, such as in optical fiber sensors [52, 53]. Conventional optical fibers are built such that the light is confined to the core, which maximizes transmission. Optical nano-fibers, on the other hand, possess a transition region that is designed to guide the light to the sub-wavelength region. There the guided field penetrates into the surrounding medium and appears as an evanescent wave that carries a significant fraction of the power and can have complex polarization patterns [54–56].

When optical nanofibers are fabricated from conventional optical fibers [6, 57], they are tapered to a diameter comparable to or smaller than the wavelength of light [58–62], typically on the order of few hundred nanometers (see Fig. 1(c)). Since optical nanofibers are very sensitive to any contaminant or dirt at their surfaces, their fabrication process and utilization have to be in very clean environments. In addition, light propagation through the optical nano-fibers strongly depends on the shape of the tapered part and the transition profile from the uniform area of the fiber to the tapered



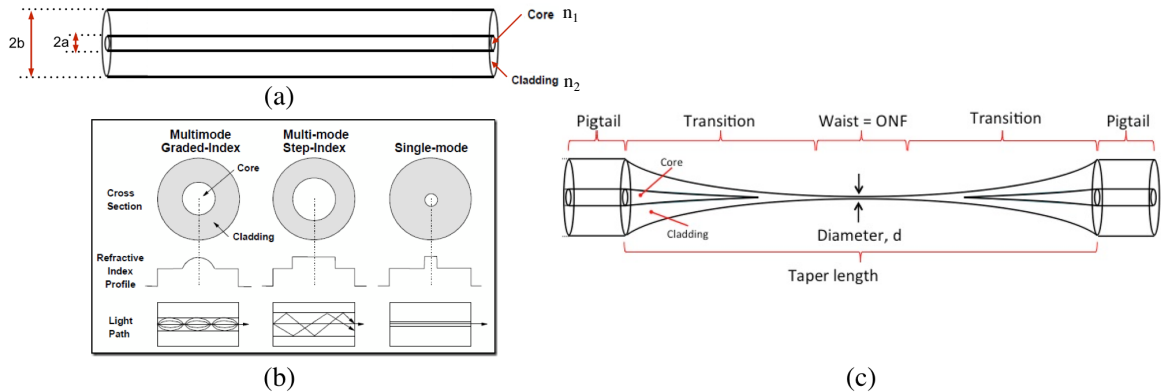


**Figure 1:** Schematic illustration of (a) a standard optical fiber with the core and cladding; (b) examples of multi-mode and single-mode fibers with their refractive index profiles and a sketch of the light path through them, reprinted from [5]; (c) schematic of a tapered optical nano-fiber where the core has vanished at the waist due to tapering, reprinted from [6].

area. Therefore, tapering has to be a well-controlled process to ensure the adiabatic evolution of the guided beam [63].

Optical nano-fibers are used as optical devices to enhance the interaction between atoms and light, and have many applications in various areas of physics as mentioned earlier. Optical nano-fibers are tapered from commercial fibers by using various techniques [64–71] to a diameter that is comparable to or smaller than the wavelength of light [65, 72]. Since the diameters are in the range of a few hundred nanometers, that is why they are called optical nano-fibers.

One of the well established techniques for fabricating tapered optical nano-fibers is melting the fiber locally by a fixed or moving a heat source while two translation stages pull at both ends of the fiber [64–67, 73]. Due to the stretching in the tapered region, the original core almost vanishes and the previous cladding becomes the new guiding medium. The new refractive indices that determine the properties of guided light are therefore those of the original silica cladding and the surrounding vacuum.

Optical nano-fibers have been used in many labs to trap and manipulate cold atoms or micro/nanometer size particles using fiber modes of different orders [74–77]. In particular they have been used for trapping atoms [76–79], for probing atoms [80–88] or molecules [89] or quantum dots [90] or color centers in nano-diamonds [91, 92], and for the mechanical manipulation of small particles [93–95]. An atomic trapping potential around an optical nano-fiber can be produced from blue detuned laser fields (one-color trap) [96], or a red and a blue detuned beam (gradient trapping or two-color trap) [76, 79, 97, 98], or by interfering with higher order modes [99, 100].

## High refractive index prism

A common place for creating evanescent fields for many uses is the surface of highly refractive index prisms, when a beam is incident with an incidence angle larger than the critical angle. In this situation, even though the light beam is fully reflected back

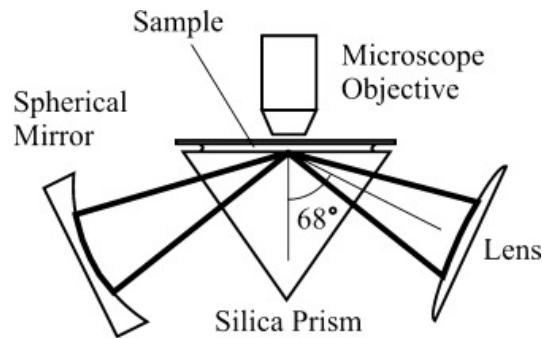


**Figure 2:** Schematic of a prism configuration which is embedded in a typical near-field scanning optical microscopy setup. Around the critical angle, counter propagating beams, which meet at the surface of the prism, create an interference pattern in the evanescent field. By bringing particles close to the surface of the prism, they can be trapped in the evanescent field and can be observed with the Microscope Objective. Reprinted from [7].

within the dielectric medium, an exponentially decaying, evanescent field will appear at the surface of the prism. Due to the simplicity of such a setup, it has found many applications not only in physics, but also in chemistry and biology [101–106]. Notably, this setup allows one to trap, levitate, and accelerating small particles on the prism surface.

Trapping and manipulating micrometer and nanometer size particles with electromagnetic near-fields at the surface of a dielectric medium can be done with a well-known technique in nano-optics that is called near-field scanning optical microscopy [107, 108]. It allows one to obtain high spatial-frequency [109] information about the trapped particles and can be used for sorting particles according to their size [110]. Generally, a near-field scanning optical microscopy setup consists of a prism, on whose surface two incident and counter-propagating beams meet (see Fig. 2). This induces an interference pattern stemming from the transmitted or evanescent field on the surface of the prism [7], depending on the critical angle, in which particles can be trapped [111]. Altering the angle of the incident beam from the partial transmission to total reflection changes the amplitude of the trapping potential, which can be used to sort particles according to their sizes [110]. However, since the optical field is evanescent, the interference pattern decays exponentially from the surface of the substrate.

## Applications

Designing, manufacturing and utilizing hybrid quantum systems which consist of neutral atoms and nano-optical devices is currently a highly active research area [112]. In recent years, new technologies have been developed that can bring neutral atoms close to one another in a controlled way and also close to the surfaces of miniaturized optical devices, which leads to the ability to study controlled interactions between atoms and surface fields. In the vicinity of devices made from dielectric materials, neutral atoms experience changes in their properties, such as frequency shifts of the atomic transitions as well as changes in the spontaneous decay rate [8]. For cases of more than one

atom, the dielectric medium can also modify the coupling between the atoms and it is interesting to determine how this can lead to an enhanced coupling strength that would otherwise only be weak in free space [46]. The presence of a dielectric medium can have profound effects on the spontaneous emission rate of pairs of atoms, and in particular the rotating induced dipoles can lead to an asymmetry in the collective spontaneous emission rate.

Asymmetry in the direction of propagation of light due to the physical properties of the system is known as chirality of light. The chirality of emitted or absorbed light is an interesting feature of optical systems with numerous applications. Recently Chang *et al.* [113] have demonstrated that trapping cold atoms next to a tapered nanofiber enhances the coupling between atoms and photons and allows to create a virtual high finesse cavity. This can be considered as a result of collective effects within the cold atoms near atomic resonance. In a related work, Lodahl *et al.* [114] have proposed to use a photonic waveguide to create directional coupling between emitters, where the flow of information between emitters is unidirectional and dependent on the polarization of the light and the ordering position of the emitters. At the same time experiments have confirmed the possibility of a propagation-direction-dependence or chiral nature of light-matter interactions [47, 114, 115].

This thesis is organised as follows. In Chapter 1, I introduce two mathematical techniques that will later be used to calculate the various properties of few-body atomic systems in free space and in the vicinity of a dielectric media. Chapter 2 then focuses on studying the effect of a dielectric medium on the atomic properties of two neutral atoms with arbitrarily polarized dipoles and I also explain how to calculate the spontaneous emission rate of atoms near a dielectric medium. In chapter 3 I use the same method to study the decay rates of multi-level atom in the vicinity in ultra-thin optical nanofiber and show how the spontaneous emission depends on hyperfine states and on the mode of input laser field. Chapter 4 focuses on how the complex electric dipole moment also leads to chiral force and in Chapter 5, I present my work on how the presence of an inhomogeneous evanescent field induces local rotation in atomic Bose-Einstein condensates. In particular, I will discuss how this leads to symmetry breaking in a multi-component system in the phase-separation regime.



# Chapter 1

## Mathematical methods

In this chapter, I introduce two well-known mathematical methods which are typically used to study the physical properties of atomic systems coupled to optical fields: the mode function and the Green's function method. In the first part of this chapter, I give a brief review of the mode function method and explain the formalism for a flat dielectric plane and for an optical nanofiber. In the second half I introduce the Green's function method and explain the various modes of an optical nanofiber in this formalism.

In the following three chapters, I will use both these methods to calculate the properties of atomic systems, such as decay rates, frequency shifts and the force on and between atoms in the vicinity of the dielectric medium.

### 1.1 Maxwell's equations and electromagnetic fields

The electric part,  $\mathbf{E}(r, t)$ , and the magnetic part,  $\mathbf{H}(r, t)$ , of the electromagnetic field are related to each other via the well-known Maxwell equations as

$$\nabla \times \mathbf{E} = -\mu_0 \frac{\partial \mathbf{H}}{\partial t}, \quad (1.1a)$$

$$\nabla \times \mathbf{H} = \mathbf{J} + \epsilon_0 \frac{\partial \mathbf{E}}{\partial t}, \quad (1.1b)$$

$$\nabla \cdot (\mu_0 \mathbf{H}) = 0, \quad (1.1c)$$

$$\nabla \cdot (\epsilon_0 \mathbf{E}) = \rho. \quad (1.1d)$$

Here  $\epsilon_0$  and  $\mu_0$  are the electric permittivity and magnetic permeability of the vacuum, respectively, and the electric charge density,  $\rho$ , and electric current density,  $\mathbf{J}$ , are related via the continuity equation

$$\nabla \cdot \mathbf{J} = -\frac{\partial \rho}{\partial t}. \quad (1.2)$$

This system of equations exhibits wave-like solutions which can be obtained by solving for the eigenstates of a wave equation. To get this wave equation from Maxwell's equations, one needs to apply the curl operator ( $\nabla \times$ ) on Eqs. (1.1a) and (1.1b), and

then replace  $\mathbf{E}$  and  $\mathbf{H}$  from Eqs. (1.1a) and (1.1b) respectively. This leads to two equations of the form

$$\nabla \times \nabla \times \mathbf{E} = -\mu_0 \frac{\partial \mathbf{J}}{\partial t} - \mu_0 \epsilon_0 \frac{\partial^2 \mathbf{E}}{\partial t^2}, \quad (1.3a)$$

$$\nabla \times \nabla \times \mathbf{H} = \nabla \times \mathbf{J} - \mu_0 \epsilon_0 \frac{\partial^2 \mathbf{H}}{\partial t^2}, \quad (1.3b)$$

which can be transformed into inhomogeneous wave equations. Using an ansatz where the electromagnetic field oscillates with frequency  $\omega$ , such that the time dependent term of the field takes the form  $\exp(\pm i\omega t)$ , one can write  $\mathbf{E} = \mathcal{E} \exp(i\omega t) + \text{c.c.}$  for the electric field and  $\mathbf{H} = \mathcal{H} \exp(i\omega t) + \text{c.c.}$  for the magnetic field. Thus the above equations simplify as

$$\nabla \times \nabla \times \mathcal{E} - \kappa^2 \mathcal{E} = i\omega \mu_0 \mathcal{J}, \quad (1.4a)$$

$$\nabla \times \nabla \times \mathcal{H} - \kappa^2 \mathcal{H} = \nabla \times \mathcal{J}, \quad (1.4b)$$

where  $\kappa = \omega \sqrt{\mu_0 \epsilon_0}$  is known as the free-space wavenumber [116]. Since the right hand side of both equations is not zero, these are inhomogeneous vector wave equations, which can be solved using various mathematical techniques. In the following sections, I discuss two of these techniques and explain how to find the solutions for different boundary conditions.

## 1.2 Mode function method

In this section, I introduce the mathematical tools of the mode function method. I start by briefly introducing the formalism for the electric field in second quantization, followed by a short discussion about the effect of boundaries on the mode functions of any electromagnetic field, which can be generalized to the mode function of the vacuum field.

### 1.2.1 Electromagnetic field in the presence of a dielectric medium

While the classical description of an electromagnetic (EM) field can be used to study a wide range of effects in modern physics, there are a few phenomena that can not be explained by this approach, with the most prominent example being the discrete processes of emission and absorption of light by an atom. The quantum mechanical approach to understanding these phenomena is to quantize the fields as well as the atoms. In this section I will introduce the quantization of the field in the presence of a dielectric medium in a half space.

Since the electric and magnetic components of EM fields are related to each other via the Maxwell equations, it is sufficient to choose only one component to characterize any EM field. In the second quantized formalism the electric field can be expressed as a summation of creation ( $a_\alpha^\dagger$ ) and annihilation ( $a_\alpha$ ) operators of bosons in mode  $\alpha$ , where the bosonic mode multi-index  $\alpha = (\omega \mathbf{K} q j)$  includes the frequency  $\omega = ck$ ; the vector  $\mathbf{K}$ , which is the projection of the wave-vector onto the dielectric surface,

$\mathbf{K} = (0, K_y, K_z)$ ; the mode polarization index  $q = \{s, p\}$ ; and  $j = \{1, 2\}$ , which represents the medium into which the input mode is emitted. Here we have assumed that the dielectric surface is located in the  $y - z$  plane, so that the electric field at time  $t$  and at position  $\mathbf{r} = (x, y, z)$  is given by

$$\mathbf{E}(\mathbf{r}, t) = A \sum_{\alpha} \mathbf{U}_{\alpha}(x) a_{\alpha} e^{-i(\omega t - \mathbf{K} \cdot \mathbf{R})} + h.c., \quad (1.5)$$

where  $\mathbf{U}_{\alpha}(x)$  corresponds to the mode function of the field. The normalization constant,  $A = \frac{ik}{4\pi} \sqrt{\frac{\hbar}{\pi \epsilon_0 \beta_j}}$ , depends on the reduced Plank constant,  $\hbar$ , and the permittivity of free space,  $\epsilon_0$ . The quantity  $\beta_j$  depends on the refractive index of the medium  $j$ ,  $n_j$ , and the vector  $\mathbf{K}$ , and is determined by the equation  $\beta_j = (k^2 n_j^2 - K^2)^{1/2}$ . The projection of the position vector  $\mathbf{r}$  onto the interface between the vacuum and dielectric surface is given by  $\mathbf{R} = (0, y, z)$ .

The mode function,  $\mathbf{U}_{\alpha}(x)$ , carries information about the polarization and propagation direction of the field, which will be explained in more detail in the next section. It is possible to decompose the summation over  $\alpha$  into a summation over  $qj$ , and integration over  $\omega$  and  $K$ , as

$$\sum_{\alpha} = \sum_{qj} \int_0^{\infty} d\omega \int_0^{kn_j} K dK \int_0^{2\pi} d\phi, \quad (1.6)$$

where the angle  $\phi$  encodes the orientation of  $K$  in the  $y - z$  plane and  $\omega$  is the positive frequency part [8].

### 1.2.2 Boundary conditions and Fresnel relation

To understand the effects of boundary conditions on a vacuum field [117, 118], consider an electromagnetic plane wave incident at the interface between the vacuum and a dielectric medium (see Fig. 1.1). It is common to write the expression for the electromagnetic field as a function of its polarization components, such as parallel (s), perpendicular (p), or a superposition of both of them. The vector  $\mathbf{s}$  is defined as the unit polarization vector for an s-polarised mode (or the electric field in the transverse electric (TE) modes), and is given by  $\mathbf{s} = [\mathbf{K} \times \mathbf{x}]$ . Likewise,  $\mathbf{p}_+$  and  $\mathbf{p}_-$  are left and right handed unit polarization vectors for  $p$  modes (or transverse magnetic (TM) modes). In a medium  $j$ , the left- and right-handed unit polarization vectors are formed by  $\mathbf{p}_{j+} = (K\mathbf{x} - \beta_j \mathbf{K})/kn_j$  and  $\mathbf{p}_{j-} = (K\mathbf{x} + \beta_j \mathbf{K})/kn_j$ , respectively.

As an example of the notation, let us consider a mode function  $\mathbf{U}_{\omega \mathbf{K} s 1}(x)$ , which represents a mode for a wave with frequency  $\omega$ , a projected wave vector on the interface between the vacuum and the dielectric medium,  $\mathbf{K}$ , and the polarisation mode  $s$  in the medium 1, which is the dielectric medium here. The explicit expression of the mode function  $\mathbf{U}_{\omega \mathbf{K} s 1}(x)$  has two terms, one for the beam coming from the left side of the interface (see Fig. 1.1(a), red arrow), given by  $e^{i\beta_1 x}$ , and the other term is due to the reflection from the surface and given by  $e^{-i\beta_1 x}$  (see Fig. 1.1(a), blue arrow). The reflection coefficient is given by  $r_{12}^s$  (see eq. (1.7a)). The mode function for the  $s$ -polarised mode which is transmitting from the vacuum into the dielectric medium,

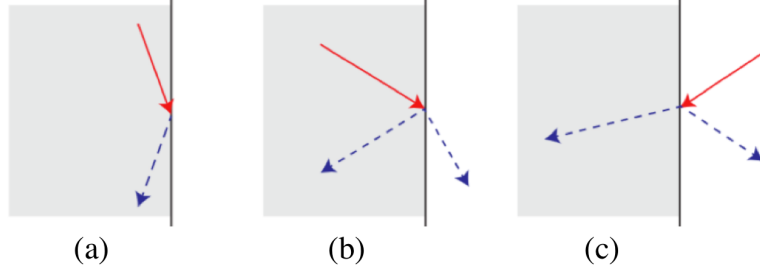


**Figure 1.1:** Schematic of all possible beam propagations at a dielectric surface. (a) The propagated field inside of the dielectric medium (red arrow) gets fully reflected at the interface between the vacuum and dielectric surface (dashed blue arrow). (b) The same as (a), however, since the angle is greater than critical angle for complete reflection, the propagating beam inside the dielectric medium is partially reflected and partially transmitted (dashed blue arrows). (c) The field propagates in free space (red arrow) and is partially reflected and transmitted at the surface of the dielectric medium (blue dashed arrows). Figure reproduced from [8].

$\mathbf{U}_{\omega\mathbf{K}s2}(x)$ , has a term for transmission between the vacuum and the dielectric medium of the form  $e^{-i\beta_1x}$ , but with the transmission coefficient of  $t_{21}^s$  (see eq. (1.7b)).

Similar notation holds for  $p$ -polarised modes, with the additional consideration that this polarization has right- and left-circularly polarized components,  $\mathbf{p}_{1+}$  and  $\mathbf{p}_{1-}$ , which change their direction after reflection from the surface. Inside of the dielectric medium ( $x < 0$ ), the mode functions are therefore given by the expressions

$$\mathbf{U}_{\omega\mathbf{K}s1}(x) = (e^{i\beta_1x} + e^{-i\beta_1x}r_{12}^s)\mathbf{s}, \quad (1.7a)$$

$$\mathbf{U}_{\omega\mathbf{K}s2}(x) = e^{-i\beta_1x}t_{21}^s\mathbf{s}, \quad (1.7b)$$

$$\mathbf{U}_{\omega\mathbf{K}p1}(x) = e^{i\beta_1x}\mathbf{p}_{1+} + e^{-i\beta_1x}r_{12}^p\mathbf{p}_{1-}, \quad (1.7c)$$

$$\mathbf{U}_{\omega\mathbf{K}p2}(x) = e^{-i\beta_1x}t_{12}^p\mathbf{p}_{1-}. \quad (1.7d)$$

In the above equations  $r_{jj'}^s$ ,  $t_{jj'}^s$ ,  $r_{jj'}^p$  and  $t_{jj'}^p$  are the Fresnel coefficients of reflection and transmission for the TE and TM modes [116]. The relations between these coefficients and the components of the vacuum wave vector  $\mathbf{K}$  in Cartesian coordinates,  $(\beta_j, K_y, K_z)$ , are given by

$$r_{jj'}^s = \frac{(\beta_j - \beta_{j'})}{(\beta_j + \beta_{j'})}, \quad (1.8a)$$

$$t_{jj'}^s = \frac{2\beta_j}{(\beta_j + \beta_{j'})}, \quad (1.8b)$$

$$r_{jj'}^p = \frac{(\beta_j n_{j'}^2 - \beta_{j'} n_j^2)}{(\beta_j n_{j'}^2 + \beta_{j'} n_j^2)}, \quad (1.8c)$$

$$t_{jj'}^p = \frac{2n_j n_{j'} \beta_{j'}}{(\beta_j n_{j'}^2 + \beta_{j'} n_j^2)}, \quad (1.8d)$$



where the magnitude of the wave vector in the  $x$  direction, is defined by  $\beta_j = (k^2 n_j^2 - K^2)^{1/2}$ . Here  $n_j$  are the refractive indices of the medium  $j$ .

The mode functions outside of the dielectric medium (in the positive half-space  $x > 0$ ) can equivalently be written as

$$\mathbf{U}_{\omega\mathbf{K}s1}(x) = e^{i\beta_2 x} t_{12}^s \mathbf{s}, \quad (1.9a)$$

$$\mathbf{U}_{\omega\mathbf{K}p1}(x) = e^{i\beta_2 x} t_{12}^p \mathbf{p}_{2+}, \quad (1.9b)$$

$$\mathbf{U}_{\omega\mathbf{K}s2}(x) = (e^{-i\beta_2 x} + e^{i\beta_2 x} r_{21}^s) \mathbf{s}, \quad (1.9c)$$

$$\mathbf{U}_{\omega\mathbf{K}p2}(x) = e^{-i\beta_2 x} \mathbf{p}_{2-} + e^{i\beta_2 x} r_{21}^p \mathbf{p}_{2+}. \quad (1.9d)$$

The mode function method has been used by Le Kien *et al.* [8] to study the spontaneous emission coefficient of a single neutral two-level atom near a flat dielectric surface. In this work, the notable assumption was that the electric dipole moment of the atom,  $\mathbf{d}_{eg}$ , can have complex matrix dipole elements, which can lead to a chiral nature of light in the spontaneous emission process.

### 1.2.3 Interaction between atoms and vacuum fields

For an atom with two internal states, a ground  $|g\rangle$  and an excited  $|e\rangle$  state, the interaction with the vacuum field in the interaction picture is given by [8]

$$\mathcal{H}_{\text{int}} = -i\hbar \sum_{\alpha} G_{\alpha} \sigma^{\dagger} a_{\alpha} e^{-i(\omega - \omega_0)t} + \text{h.c.}, \quad (1.10)$$

where the  $G_{\alpha}$  are the coupling coefficients between the vacuum fields,  $\mathbf{U}_{\omega\mathbf{K}qj}$ , and the atomic dipole moment  $\mathbf{d}_{eg}$ . They are given explicitly by [8]

$$G_{\alpha} = \frac{k}{4\pi\sqrt{\pi\epsilon_0\hbar}\beta_j} e^{i\mathbf{K}\cdot\mathbf{R}} (\mathbf{U}_{\omega\mathbf{K}qj} \cdot \mathbf{d}_{eg}). \quad (1.11)$$

The  $\sigma^{\dagger}$  and  $\sigma$  are raising and lowering operators, which bring the atomic state from  $|g\rangle$  to  $|e\rangle$  and  $|e\rangle$  to  $|g\rangle$ , respectively. The annihilation and creation operators for the electric field in the particular mode  $\alpha$  are given by  $a_{\alpha}$  and  $a_{\alpha}^{\dagger}$ , respectively. Finally,  $\omega_0$  is the atomic transition frequency between the ground and excited states.

In the next chapter, I will explain how to use the mode function method to calculate the various components of the decay rates for two atoms in the vicinity of a dielectric surface. From this the directional force of light on atoms can be calculated as well.

## 1.3 Guided modes of a step-index optical fiber

In this section, I will illustrate how to calculate the mode functions of an optical nanofiber. For this I will assume that the fiber has cylindrical symmetry with radius  $a$  and a refractive index  $n_1$ , and is embedded in a medium with a refractive index of  $n_2$ , where  $n_2 < n_1$ . Due to the cylindrical symmetry of the optical fiber, I will use cylindrical coordinates  $\{r, \varphi, z\}$ , where  $z$  is the coordinate along the fiber axis and  $r$

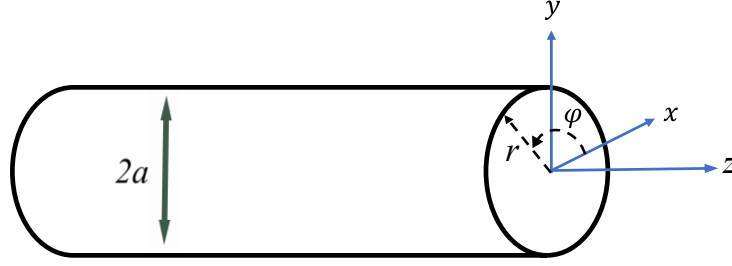


**Figure 1.2:** Schematic of the Cartesian and cylindrical coordinate systems used for an optical nanofiber setup. The radius of the fiber is given by  $a$ .

and  $\varphi$  are the polar coordinates in the transverse  $x - y$  plane. (see Fig. 1.2)

The electric component of the field for an optical fiber can be written in the form of

$$\mathbf{E}(r, \varphi, z) = \frac{1}{2} \mathcal{E} e^{-i\omega t} + \text{c.c.}, \quad (1.12)$$

where  $\mathcal{E}$  is the envelope and  $\omega$  is the frequency (free-space wavelength  $\lambda = 2\pi c/\omega$  and free-space wave number  $k = \omega/c$ ). Propagation of light in an optical fiber is described by the Helmholtz equations for the electric and magnetic fields. I assume that the electric field,  $\mathcal{E}$ , can be decomposed into its components  $E_r(r)$ ,  $E_\varphi(\varphi)$  and  $E_z(z)$  and similarly for the magnetic field,  $B_r(r)$ ,  $B_\varphi(\varphi)$  and  $B_z(z)$ . This allows us to solve these equations by separation of variables and since both equations have the same form, I will use the general notation  $\psi(r, \varphi, z) = A_r(r)B_\varphi(\varphi)C_z(z)$  for both fields. This leads to a wave equation in cylindrical coordinates of the form<sup>1</sup>

$$\frac{1}{A_r} \frac{1}{r} \frac{\partial}{\partial r} \left( r \frac{\partial A_r}{\partial r} \right) + \frac{1}{B_\varphi} \frac{1}{r^2} \frac{\partial^2 B_\varphi}{\partial \varphi^2} + \frac{1}{C_z} \frac{\partial^2 C_z}{\partial z^2} = -\kappa^2, \quad (1.13)$$

which can be separated into three independent equations given by

$$\frac{1}{C_z} \partial_z^2 C_z = -\beta^2, \quad (1.14a)$$

$$\frac{1}{B_\varphi} \frac{1}{r^2} \partial_\varphi^2 B_\varphi = -k_\varphi^2, \quad (1.14b)$$

$$\frac{1}{A_r} \frac{1}{r} \partial_r (r \partial_r A_r) = -k_r^2, \quad (1.14c)$$

where  $\beta^2 + k_\varphi^2 + k_r^2 = \kappa^2$ . Each of these equations now has a familiar differential form, that also allows to easily satisfy the boundary condition for each components of the field. Here I will use the Dirichlet boundary condition, since they satisfy the continuity of the field and the potential at the surface [116]. At the interface of the optical fiber

<sup>1</sup>The Laplacian operator in cylindrical coordinate is  $\nabla^2 = \frac{1}{r} \frac{\partial}{\partial r} \left( r \frac{\partial}{\partial r} \right) + \frac{1}{r^2} \frac{\partial^2}{\partial \varphi^2} + \frac{\partial^2}{\partial z^2}$ .

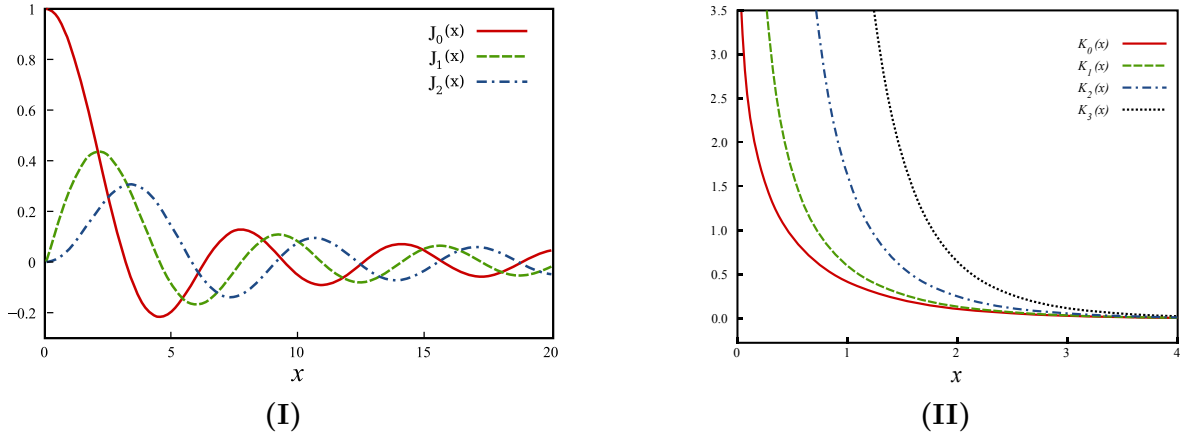


**Figure 1.3:** (a) Bessel functions of first kind,  $J_l(x)$  and (b) modified Bessel functions of second kind,  $K_l(x)$ .

and the vacuum,  $r = a$ , the solutions of Eqs. (1.14a) and (1.14b) can be written as

$$C_z = e^{(\pm i\beta z)} \quad \text{for } \beta \in (-\infty, +\infty), \quad (1.15)$$

$$B_\varphi = e^{(\pm i r k_\varphi \varphi)} \quad \text{for } k_\varphi r \in \mathbb{Z}, \quad (1.16)$$

where the angular term,  $B_\varphi(\varphi)$  satisfies periodic boundary condition,  $B_\varphi(\varphi + 2\pi) = B_\varphi(\varphi)$  and  $k_\varphi r$  has discrete values which I label by  $l$ , such that the azimuthal solution is  $e^{\pm i l \varphi}$ . Depending on boundary conditions,  $l$  and  $\beta$  can be real or imaginary, thus these solutions can be sinusoidal or exponential. By substituting  $k_r^2$  with  $\kappa^2 - \beta^2 - k_\varphi^2$  in Eq. (1.14c), one finds

$$\frac{\partial^2 A_r}{\partial r^2} + \frac{1}{r} \frac{\partial A_r}{\partial r} + \left( k^2 - \beta^2 - \frac{l^2}{r^2} \right) A_r = 0, \quad (1.17)$$

and letting  $\mu^2 = \kappa^2 - \beta^2$ , the above equation becomes

$$\frac{\partial^2 A_r}{\partial r^2} + \frac{1}{r} \frac{\partial A_r}{\partial r} + \left( \mu^2 - \frac{l^2}{r^2} \right) A_r = 0. \quad (1.18)$$

This equation is known as the cylindrical Bessel equation. For an optical nano-fiber, the solutions are the Bessel functions of first kind,  $J_l$ , and modified Bessel functions of the second kind,  $K_l$ . The radial component of electric field is therefore given as a superposition of the Bessel functions,  $\mathbf{E}_r(r) = A J_l(r) + B K_l(r)$  (see Fig. 1.3 for the functional forms of various Bessel functions). The differential equations for the regions inside and outside of the fiber are solved separately, and the boundary conditions between the two regions are matched by adjusting the coefficients: the tangential components of electric ( $E_z$ ,  $E_\varphi$ ), and magnetic ( $H_z$ ,  $H_\varphi$ ) field have to be continuous at the interface between the core and the cladding.

For a guided mode with a propagation constant  $\beta$  and an azimuthal mode order  $l$ ,

the envelope is defined as

$$\mathcal{E}(r, \varphi, z) = e^{i(\beta z + l\varphi)} \mathbf{e}, \quad (1.19)$$

where the mode profile function in cylindrical coordinates for the nanofiber is  $\mathbf{e} = (e_r, e_\phi, e_z)$ . To construct a complete set of guided modes, the  $\beta$  and  $l$  in Eq. (1.19) can have positive and negative values.

For a radiation mode, the propagation constant  $\beta$  has the range  $-kn_2 < \beta < kn_2$  and a mode order of  $l = 0, 1, 2, \dots$ . The characteristic parameters for the field in the inside and outside of the fiber are  $h = \sqrt{k^2 n_1^2 - \beta^2}$  and  $q = \sqrt{k^2 n_2^2 - \beta^2}$ , respectively, which, as already mentioned above, could be real or imaginary depending on the refractive indices and  $\beta$ .

The expressions for the mode functions of the quasicircularly polarized light can be decomposed into polarized hybrid TE and TM modes. For a guided light field, the propagation constant  $\beta$  is determined by the boundary conditions, and can be calculated by using the Bessel function solutions in the fiber eigenvalue equation as [119–121]

$$\beta^2 l^2 = k^2 \left( \frac{1}{h^2 a^2} + \frac{1}{q^2 a^2} \right)^{-2} \left[ \frac{J'_l(ha)}{ha J_l(ha)} + \frac{K'_l(qa)}{qa K_l(qa)} \right] \left[ \frac{n_1^2 J'_l(ha)}{ha J_l(ha)} + \frac{n_2^2 K'_l(qa)}{qa K_l(qa)} \right]. \quad (1.20)$$

The integer index  $l = 0, 1, 2, \dots$  determines the helical phase front and the associated phase gradient in the fiber's transverse plane. The fiber eigenvalue equation (1.20) remains the same when we replace  $\beta$  by  $-\beta$  or  $l$  by  $-l$ . The azimuthal mode for  $l = 0$  is called the TE<sub>0m</sub> mode and it satisfies the equation

$$\frac{J_1(ha)}{ha J_0(ha)} = -\frac{K_1(qa)}{qa K_0(qa)}. \quad (1.21)$$

For the magnetic part the TM<sub>0m</sub> mode follows from

$$\frac{J_1(ha)}{ha J_0(ha)} = -\frac{n_2^2}{n_1^2} \frac{K_1(qa)}{qa K_0(qa)}. \quad (1.22)$$

The index  $m = 1, 2, \dots$  defines the radial mode order. For  $l \geq 1$ , the solutions are given by hybrid HE and EH modes, where the HE<sub>lm</sub> modes are determined by [119–121]

$$\frac{J_{l-1}(ha)}{ha J_l(ha)} = -\frac{n_1^2 + n_2^2}{2n_1^2} \frac{K'_l(qa)}{qa K_l(qa)} + \frac{l}{h^2 a^2} - \mathcal{R}, \quad (1.23)$$

and the EH<sub>lm</sub> modes by

$$\frac{J_{l-1}(ha)}{ha J_l(ha)} = -\frac{n_1^2 + n_2^2}{2n_1^2} \frac{K'_l(qa)}{qa K_l(qa)} + \frac{l}{h^2 a^2} + \mathcal{R}. \quad (1.24)$$

One can see that both equations have the same form, except for a different sign in front

of the last term, which is given by

$$\mathcal{R} = \left[ \left( \frac{n_1^2 - n_2^2}{2n_1^2} \right)^2 \left( \frac{K'_l(qa)}{qaK_l(qa)} \right)^2 + \left( \frac{l\beta}{n_1k} \right)^2 \left( \frac{1}{q^2a^2} + \frac{1}{h^2a^2} \right)^2 \right]^{1/2}. \quad (1.25)$$

It is helpful to define a fiber size parameter  $V = ka\sqrt{n_1^2 - n_2^2}$ , which characterises any fiber as a function of the refractive indices, the radius and  $k$ . The cutoff values  $V_c$  for  $\text{HE}_{1m}$  modes are determined as solutions to the equation  $J_1(V_c) = 0$ , which stems from the need to satisfy the boundary condition at the surface. For the  $\text{HE}_{lm}$  modes with  $l = 2, 3, \dots$ , the cutoff values are obtained as nonzero solutions to the equation  $(n_1^2/n_2^2 + 1)(l - 1)J_{l-1}(V_c) = V_c J_l(V_c)$ . The cutoff values  $V_c$  for  $\text{EH}_{lm}$  modes, where  $l = 1, 2, \dots$ , are determined as nonzero solutions to the equation  $J_l(V_c) = 0$ . For  $\text{TE}_{0m}$  and  $\text{TM}_{0m}$  modes, the cutoff values  $V_c$  are obtained as solutions to the equation  $J_0(V_c) = 0$ .

### 1.3.1 TE modes

The transverse electric modes,  $\text{TE}_{0m}$ , are defined separately for the areas inside and outside of the optical fiber (see Fig. 1.4). For  $r < a$

$$e_r = 0, \quad (1.26a)$$

$$e_\varphi = i \frac{\omega\mu_0}{h} A J_1(hr), \quad (1.26b)$$

$$e_z = 0, \quad (1.26c)$$

and for  $r > a$ ,

$$e_r = 0, \quad (1.27a)$$

$$e_\varphi = -i \frac{\omega\mu_0}{q} \frac{J_0(ha)}{K_0(qa)} A K_1(qr), \quad (1.27b)$$

$$e_z = 0. \quad (1.27c)$$

Without loss of generality, the normalisation constant  $A$  can be considered as a real number (since  $e_\varphi^* e_\varphi$  is real valued) and the overall mode profile function of the electric component of a  $\text{TE}_{0m}$  mode with a propagation direction  $f = \pm$  (where  $+$  is forward and  $-$  is backward) can be written as

$$\mathbf{e}^{(\omega\text{TE}_{0m}f)} = \hat{\varphi} e_\varphi, \quad (1.28)$$

where the nonzero cylindrical component  $e_\varphi$  is given in Eqs. (1.26) and (1.27) for inside and outside of the fiber respectively. The index  $(\omega\text{TE}_{0m}f)$  identifies the  $\text{TE}_{0m}$  mode of the field with frequency of  $\omega$  and propagating in the  $f$  direction.

The mode function depends implicitly on the radial mode order  $m$ . The full mode function of the TE mode is  $\mathcal{E}^{(\omega\text{TE}_{0m}f)} = \mathbf{e}^{(\omega\text{TE}_{0m}f)} e^{if\beta z}$ , where  $\beta > 0$ . When the  $E_z$  component is larger than the  $H_z$  component, the mode is called an EH mode, and when it is the other way around, the mode is called an HE mode. The symmetry

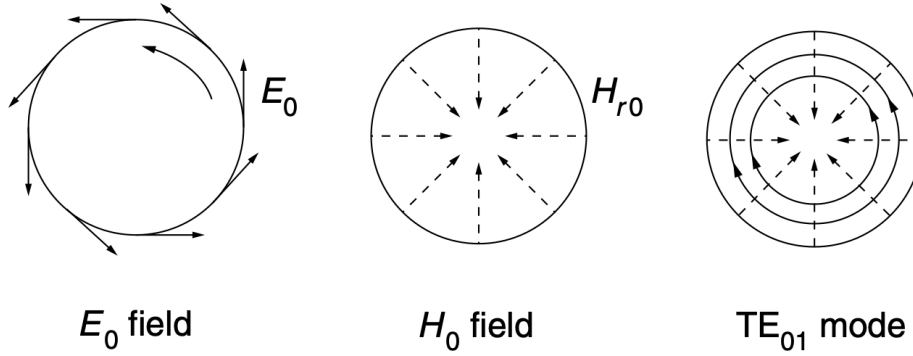


**Figure 1.4:** Schematic plot of the mode pattern for the  $TE_{01}$  mode in the azimuthal plane. The first plot on the left represents the electric field (full lines), the middle plot represents the magnetic field (dashed lines), and the one on the right represents the  $TE_{01}$  mode. Figure taken from [9].

relations of the field will be employed frequently in the future, thus as each mode is introduced, their symmetry relations will be discussed as well. The symmetry relations of the field for the  $TE_{0m}$  are as follow:  $e_\varphi^{(\omega TE_{0m}f)} = e_\varphi^{(\omega TE_{0m}\bar{f})} = -e_\varphi^{(\omega TE_{0m}f)*}$ , which yield  $\mathbf{e}^{(\omega TE_{0m}f)} = -\mathbf{e}^{(\omega TE_{0m}f)*}$ . This means that if the propagation direction,  $f$ , changes, the mode profile changes.

### 1.3.2 TM modes

Similar to the TE modes, the transverse magnetic modes,  $TM_{0m}$  (see Fig. 1.5) can also be defined separately inside and outside of the fiber. The modes inside of the fiber,  $r < a$ , are given by

$$e_r = -i\frac{\beta}{h}AJ_1(hr), \quad (1.29a)$$

$$e_\varphi = 0, \quad (1.29b)$$

$$e_z = AJ_0(hr), \quad (1.29c)$$

and for outside,  $r > a$ , are

$$e_r = i\frac{\beta}{q}\frac{J_0(ha)}{K_0(qa)}AK_1(qr), \quad (1.30a)$$

$$e_\varphi = 0, \quad (1.30b)$$

$$e_z = \frac{J_0(ha)}{K_0(qa)}AK_0(qr). \quad (1.30c)$$

The mode profile function of the electric component of a TM mode with a propagation direction  $f = \pm$  can therefore be written as

$$\mathbf{e}^{(\omega TM_{0m}f)} = \hat{\mathbf{r}}e_r + f\hat{\mathbf{z}}e_z, \quad (1.31)$$

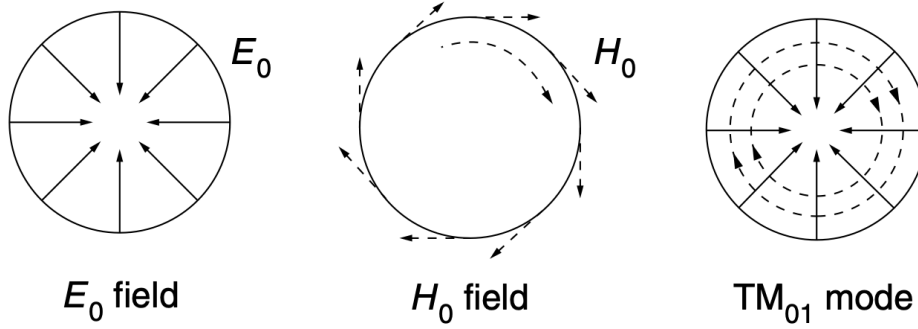


**Figure 1.5:** Schematic plot of the mode pattern for  $TM_{01}$  mode in the azimuthal plane. The first plot on the left represents the electric field (full lines), the middle plot represents the magnetic field (dashed lines), and the one on the right represents the  $TE_{01}$  mode. Graph taken from [9].

as no contribution in the  $\varphi$  direction exists for  $\beta > 0$ . Again, the mode function depends implicitly on the radial mode order  $m$ . The longitudinal component  $e_z$  of a TM mode is nonvanishing and in quadrature ( $\pi/2$  out of phase) with the radial component  $e_r$ . The full mode function of the TM mode is  $\mathcal{E}^{(\omega TM_{0m}f)} = \mathbf{e}^{(\omega TM_{0m}f)} e^{if\beta z}$ , where  $\beta > 0$ .

The symmetry relations the  $TM_{0m}$  mode are  $e_r^{(\omega TM_{0m}f)} = e_r^{(\omega TM_{0m}\bar{f})} = -e_r^{(\omega TM_{0m}f)*}$  and  $e_z^{(\omega TM_{0m}f)} = -e_z^{(\omega TM_{0m}\bar{f})} = e_z^{(\omega TM_{0m}f)*}$ , which yields  $\mathbf{e}^{(\omega TM_{0m}f)} = -\mathbf{e}^{(\omega TM_{0m}\bar{f})}$ .

### 1.3.3 Hybrid modes

Hybrid modes are modes which have  $E_z \neq 0$  and  $H_z \neq 0$ . They are labeled as  $HE_{lm}$  or  $EH_{lm}$ , depending on whether the  $E_z$  or the  $H_z$  component is dominant (see Fig. 1.6). The mode profile functions for quasi-circular polarization are given for  $r < a$  as

$$e_r = iA \frac{\beta}{2h} [(1-s)J_{l-1}(hr) - (1+s)J_{l+1}(hr)], \quad (1.32a)$$

$$e_\varphi = -A \frac{\beta}{2h} [(1-s)J_{l-1}(hr) + (1+s)J_{l+1}(hr)], \quad (1.32b)$$

$$e_z = AJ_l(hr), \quad (1.32c)$$

and for  $r > a$

$$e_r = iA \frac{\beta}{2q} \frac{J_l(ha)}{K_l(qa)} [(1-s)K_{l-1}(qr) + (1+s)K_{l+1}(qr)], \quad (1.33a)$$

$$e_\varphi = -A \frac{\beta}{2q} \frac{J_l(ha)}{K_l(qa)} [(1-s)K_{l-1}(qr) - (1+s)K_{l+1}(qr)], \quad (1.33b)$$

$$e_z = A \frac{J_l(ha)}{K_l(qa)} K_l(qr), \quad (1.33c)$$

where the parameter  $s$  is given by

$$s = l \left( \frac{1}{h^2 a^2} + \frac{1}{q^2 a^2} \right) \left[ \frac{J'_l(ha)}{ha J_l(ha)} + \frac{K'_l(qa)}{qa K_l(qa)} \right]^{-1}, \quad (1.34)$$

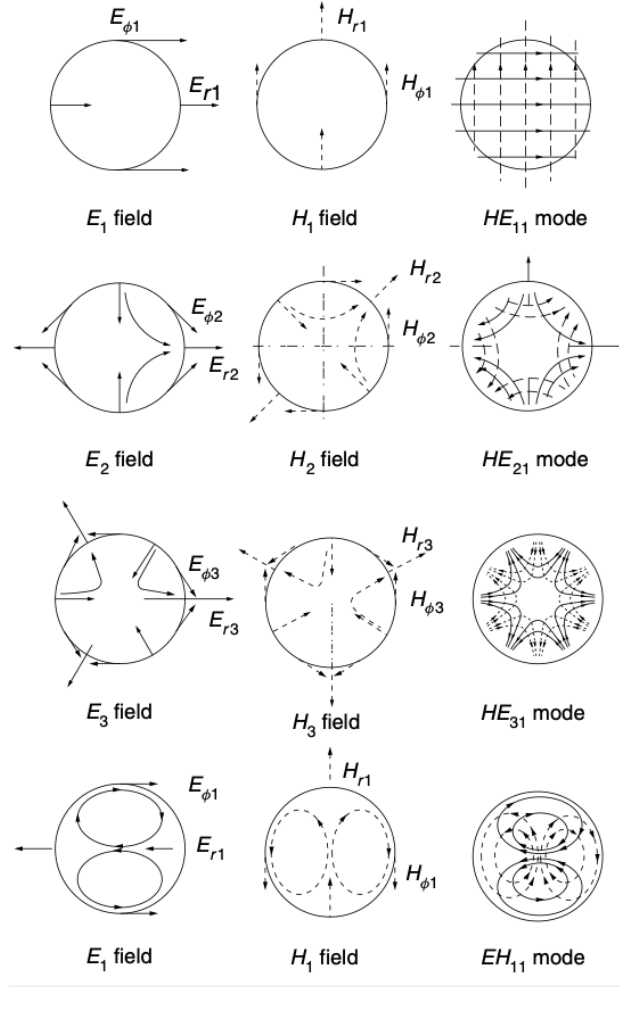


**Figure 1.6:** Examples of hybrid modes: the plots in the left column represent the electric field (solid lines), the ones in the middle column represent the magnetic field (dotted lines) and the column on the right shows the full hybrid modes. Figure taken from [9].

and the parameter  $A$  is the normalisation constant that can be determined from the propagating power of the field. Again, without loss of generality, we take  $A$  to be a real number.

The mode profile function of the electric component of a quasi-circularly polarized hybrid mode  $N$  with a propagation direction  $f = \pm$  and a phase circulation direction  $p = \pm$  is then given by

$$\mathbf{e}^{(\omega N f p)} = \hat{\mathbf{r}}e_r + p\hat{\boldsymbol{\phi}}e_\phi + f\hat{\mathbf{z}}e_z, \quad (1.35)$$

The components depend explicitly on the azimuthal mode order  $l$  and implicitly on the radial mode order  $m$ . An important property of the mode functions of hybrid modes is that the longitudinal component  $e_z$  is non-vanishing and in quadrature ( $\pi/2$  out of phase) with the radial component  $e_r$ . In addition, the azimuthal component  $e_\phi$  is also non-vanishing and in quadrature with the radial component  $e_r$ . We note that the full



mode function of the quasicircularly polarized hybrid mode is

$$\mathcal{E}^{(\omega N f p)} = \mathbf{e}^{(\omega N f p)} e^{i f \beta z + i p l \varphi} \quad (1.36)$$

where  $\beta > 0$  and  $l > 0$ .

Finally, the symmetry relations for these modes are given by [1]:  $e_r^{(\omega N f p)} = e_r^{(\omega N \bar{f} \bar{p})} = e_r^{(\omega N f \bar{p})}$ ,  $e_\varphi^{(\omega N f p)} = e_\varphi^{(\omega N \bar{f} \bar{p})} = -e_\varphi^{(\omega N f \bar{p})}$  and  $e_z^{(\omega N f p)} = -e_z^{(\omega N \bar{f} \bar{p})} = e_z^{(\omega N f \bar{p})}$ , with  $e_r^{(\mu)*} = -e_r^{(\mu)}$ ,  $e_\varphi^{(\mu)*} = e_\varphi^{(\mu)}$  and  $e_z^{(\mu)*} = e_z^{(\mu)}$ , where  $\bar{f} = -f$  and  $\bar{p} = -p$ . From these one can obtain the formulas  $e_r^{(\omega N f p)} = -e_r^{(\omega N \bar{f} \bar{p})*}$ ,  $e_\varphi^{(\omega N f p)} = -e_\varphi^{(\omega N \bar{f} \bar{p})*}$  and  $e_z^{(\omega N f p)} = -e_z^{(\omega N \bar{f} \bar{p})*}$  which yield  $\mathbf{e}^{(\omega N f p)} = -\mathbf{e}^{(\omega N \bar{f} \bar{p})*}$ . This equation is a consequence of the time reversal symmetry of the field.

### 1.3.4 Radiation modes of an optical fiber

Finally, let me describe the mode functions of the electric parts of the radiation modes. Since these depend on the frequency, we introduce the new multi-index  $\nu = (\omega \beta l p)$ , so that for  $r < a$  the modes can be written as [119–121]

$$e_r^{(\nu)} = \frac{i}{h^2} \left[ \beta h A J_l'(hr) + i l \frac{\omega \mu_0}{r} B J_l(hr) \right], \quad (1.37a)$$

$$e_\varphi^{(\nu)} = \frac{i}{h^2} \left[ i l \frac{\beta}{r} A J_l(hr) - h \omega \mu_0 B J_l'(hr) \right], \quad (1.37b)$$

$$e_z^{(\nu)} = A J_l(hr), \quad (1.37c)$$

and for  $r > a$  as

$$e_r^{(\nu)} = \frac{i}{q^2} \sum_{j=1,2} \left[ \beta q C_j H_l^{(j)'}(qr) + i l \frac{\omega \mu_0}{r} D_j H_l^{(j)}(qr) \right], \quad (1.38a)$$

$$e_\varphi^{(\nu)} = \frac{i}{q^2} \sum_{j=1,2} \left[ i l \frac{\beta}{r} C_j H_l^{(j)}(qr) - q \omega \mu_0 D_j H_l^{(j)'}(qr) \right], \quad (1.38b)$$

$$e_z^{(\nu)} = \sum_{j=1,2} C_j H_l^{(j)}(qr). \quad (1.38c)$$

Here, the coefficients  $A$  and  $B$  are related to the coefficients  $C_j$  and  $D_j$  ( $j = 1, 2$ ) via [122]

$$C_j = (-1)^j \frac{i \pi q^2 a}{4 n_2^2} (A L_j + i \mu_0 c B V_j), \quad (1.39a)$$

$$D_j = (-1)^{j-1} \frac{i \pi q^2 a}{4} (i \epsilon_0 c A V_j - B M_j), \quad (1.39b)$$

where

$$V_j = \frac{lk\beta}{ah^2q^2}(n_2^2 - n_1^2)J_l(ha)H_l^{(j)*}(qa), \quad (1.40a)$$

$$M_j = \frac{1}{h}J_l'(ha)H_l^{(j)*}(qa) - \frac{1}{q}J_l(ha)H_l^{(j)*'}(qa), \quad (1.40b)$$

$$L_j = \frac{n_1^2}{h}J_l'(ha)H_l^{(j)*}(qa) - \frac{n_2^2}{q}J_l(ha)H_l^{(j)*'}(qa). \quad (1.40c)$$

Two polarizations can be specified by choosing  $B = \pm i\eta A$  for  $p = \pm$  and  $A$  can be assumed to be real valued.

The symmetry relations for Hybrid modes are as follow [1];  $e_r^{(\omega\beta lp)} = -e_r^{(\omega\bar{\beta}l\bar{p})}$ ,  $e_\varphi^{(\omega\beta lp)} = -e_\varphi^{(\omega\bar{\beta}l\bar{p})}$ ,  $e_z^{(\omega\beta lp)} = e_z^{(\omega\bar{\beta}l\bar{p})}$ ,  $e_r^{(\omega\beta lp)} = (-1)^l e_r^{(\omega\bar{\beta}l\bar{p})}$ ,  $e_\varphi^{(\omega\beta lp)} = (-1)^{l+1} e_\varphi^{(\omega\bar{\beta}l\bar{p})}$ ,  $e_z^{(\omega\beta lp)} = (-1)^l e_z^{(\omega\bar{\beta}l\bar{p})}$ , and also  $e_r^{(\nu)*} = -e_r^{(\nu)}$ ,  $e_\varphi^{(\nu)*} = e_\varphi^{(\nu)}$ ,  $e_z^{(\nu)*} = e_z^{(\nu)}$ , which yield  $\mathbf{e}^{(\omega\beta lp)} = (-1)^l \mathbf{e}^{(\omega\bar{\beta}l\bar{p})*}$ , where the notations are  $\bar{\beta} = -\beta$ ,  $\bar{l} = -l$ , and  $\bar{p} = -p$ .

For the spherical tensor components  $e_q^{(\omega,\beta,l,p)}$ , with the index  $q = 0, \pm 1$ , of the radiation mode functions, the symmetry relations are  $e_q^{(\omega\beta lp)} = (-1)^q e_q^{(\omega\bar{\beta}l\bar{p})}$ ,  $e_q^{(\omega\beta lp)} = (-1)^{l+q} e^{2iq\varphi} e_{-q}^{(\omega\bar{\beta}l\bar{p})}$ , and  $e_q^{(\omega\beta lp)} = (-1)^q e^{2iq\varphi} e_q^{(\omega\beta lp)}$ .

The orthogonality of the modes requires

$$\int_0^{2\pi} d\varphi \int_0^\infty n_{\text{ref}}^2 \left[ \mathbf{e}^{(\nu)} \mathbf{e}^{(\nu')*} \right]_{\beta=\beta', l=l'} r dr = N_\nu \delta_{pp'} \delta(\omega - \omega'), \quad (1.41)$$

where  $n_{\text{ref}}(r) = n_1$  for  $r < a$  and  $n_2$  for  $r > a$  [1], which leads to

$$\eta = \epsilon_0 c \sqrt{\frac{n_2^2 |V_j|^2 + |L_j|^2}{|V_j|^2 + n_2^2 |M_j|^2}}, \quad (1.42)$$

where the constant  $N_\nu$  is given by

$$N_\nu = \frac{8\pi\omega}{q^2} \left( n_2^2 |C_j|^2 + \frac{\mu_0}{\epsilon_0} |D_j|^2 \right). \quad (1.43)$$

In this section, the mode functions for a flat dielectric surface and an optical fiber were reviewed and next I will introduce the Green's function method. These tools will be used to calculate the spontaneous emission of atoms in the vicinity of a flat dielectric surface or an optical nanofiber in Chapter 2, and the chiral force on an atom in Chapter 3.

## 1.4 Green's function method

The Green's function method is a very powerful mathematical tool to find the solution to a large variety of inhomogeneous differential equations. It makes it possible to directly transform the electromagnetic source into an electromagnetic field by a simple integration. The Green's function method has two main steps: the first is to determine the Green's function of the homogeneous problem (assuming a point source instead of

the actual source), and the second is to use the obtained Green's function to express the solution of the full problem. In this thesis, this method will be used to calculate the total force of light on an atom in the vicinity of an optical nanofiber, starting from the Hamiltonian of the dipole-dipole interaction. The results corresponding to this are shown in Chapter 3.

While the wave equations (1.4) can be used to define the electric and magnetic fields, they can also be written using the more fundamental quantities of a vector field  $\mathbf{A}(\mathbf{r}, t)$  and a scalar potential  $\Psi(\mathbf{r}, t)$ , where these satisfy the conditions  $\nabla \times \nabla \Psi(\mathbf{r}, t) = 0$  and  $\nabla \cdot \nabla \times \mathbf{A}(\mathbf{r}, t) = 0$ . This leads to

$$\mathbf{H}(\mathbf{r}, t) = \frac{1}{\mu} \nabla \times \mathbf{A}(\mathbf{r}, t), \quad (1.44)$$

$$\mathbf{E}(\mathbf{r}, t) = i\omega \mathbf{A}(\mathbf{r}, t) - \nabla \Psi(\mathbf{r}, t). \quad (1.45)$$

Placing these expressions into Eqs. (1.1b) and (1.1a), the wave equations for the vector and scalar potentials are

$$\nabla^2 \psi(\mathbf{r}, t) + \kappa^2 \psi(\mathbf{r}, t) = -\frac{\rho(\mathbf{r}, t)}{\epsilon_0}, \quad (1.46)$$

$$\nabla^2 \mathbf{A}(\mathbf{r}, t) + \kappa^2 \mathbf{A}(\mathbf{r}, t) = -\mu_0 \mathbf{J}(\mathbf{r}, t). \quad (1.47)$$

The solution to an inhomogeneous wave-equation can be given in terms of a Green's function. For the scalar problem, the Green's function is a scalar function,  $g(\mathbf{r}, \mathbf{r}')$ , which in general fulfills the following differential equation

$$\nabla^2 g(\mathbf{r}, \mathbf{r}') + \kappa^2 g(\mathbf{r}, \mathbf{r}') = -\delta(\mathbf{r}, \mathbf{r}'), \quad (1.48)$$

where  $\mathbf{r}'$  denotes the position of a source and  $\mathbf{r}$  is the position of the field or observation point. The constant  $\kappa$  is known as the propagation constant and  $\delta(\mathbf{r}, \mathbf{r}')$  is the delta Dirac function. There are different methods to solve the above equation, using for example an inhomogeneous differential equation such as Ohm-Rayleigh introduced by Sommerfeld or an eigenfunction expansion [123]. Two boundary conditions are needed to determine the solution to this equation and, depending on their form, different solutions can be found. From Eq. (1.48), the scalar Green's function can be calculated as

$$g(\mathbf{r}, \mathbf{r}') = \frac{e^{i\kappa|\mathbf{r}-\mathbf{r}'|}}{4\pi|\mathbf{r}-\mathbf{r}'|}. \quad (1.49)$$

Therefore outside of a dielectric medium and in Cartesian coordinates where  $|\mathbf{r}-\mathbf{r}'| = [(x-x')^2 + (y-y')^2 + (z-z')^2]^{\frac{1}{2}}$ , for the case that  $\mathbf{r} \gg \mathbf{r}'$  and  $\kappa r \gg 1$  or  $r \gg 2\pi/\kappa$  it is approximately given by

$$g(\mathbf{r}, \mathbf{r}') \approx \frac{e^{i\kappa(\mathbf{r}-\mathbf{r}' \cdot \hat{\mathbf{r}})}}{4\pi\mathbf{r}}, \quad (1.50)$$

where now  $\hat{\mathbf{r}} = \frac{\mathbf{r}}{|\mathbf{r}|}$  is the unit vector in the  $\mathbf{r}$  direction. In the radiation limit, where the outgoing wave goes to infinity, the scalar function in one dimension can be written

as

$$g(x, x') = \begin{cases} Ae^{i\kappa x} & \text{if } x > x' \\ Be^{-i\kappa x} & \text{if } x < x' \end{cases} \quad (1.51)$$

where the boundary condition at infinity determines the sign of the exponential. Two other boundary conditions are given by the requirement of continuity of  $g(x, x')$  and of the derivative at  $x = x'$ . This leads to

$$\left[ g(x, x') \right]_{x'-0}^{x'+0} = 0 \quad \text{continuity in } g \quad (1.52)$$

$$\left[ \frac{dg(x, x')}{dx} \right]_{x'-0}^{x'+0} = -1 \quad \text{discontinuity in } g \quad (1.53)$$

From this the coefficients  $A$  and  $B$  can be determined as  $A = B = \frac{i}{2\kappa}e^{-i\kappa x'}$ , and equation (1.51) acquires the familiar form of

$$g(x, x') = \frac{i}{2\kappa}e^{ik|x-x'|}. \quad (1.54)$$

Similarly, for the vector problem the dyadic Green's function can be calculated from Eq. (1.47) as

$$\mathbf{G}(\mathbf{r}, \mathbf{r}') = \mathbf{I} \frac{e^{i\kappa|\mathbf{r}-\mathbf{r}'|}}{4\pi|\mathbf{r}-\mathbf{r}'|}, \quad (1.55)$$

where  $\mathbf{I}$  denotes a  $3 \times 3$  unitary matrix.

### 1.4.1 Green's tensor of an optical fiber

In this section I consider an optical fiber with a circular cross section of radius  $a$  and the axis of the cylinder is along the  $z$  direction (see Fig. 1.2). By using the Maxwell equations and implementing the relevant boundary conditions for a point source outside of the fiber at distance  $r' > a$ , the Green's function of the fiber is defined by [123]

$$\mathbf{G}(\mathbf{r}, \mathbf{r}', \omega) = \begin{cases} \mathbf{G}^{(0)}(\mathbf{r}, \mathbf{r}', \omega) + \mathbf{G}^{(R)}(\mathbf{r}, \mathbf{r}', \omega) & \text{if } r > a \\ \mathbf{G}^{(T)}(\mathbf{r}, \mathbf{r}', \omega) & \text{if } r < a. \end{cases} \quad (1.56)$$

Here the indices  $R$  and  $T$  stand for the reflected and transmitted parts.

If these functions satisfy the Dirichlet boundary condition at  $r = a$ , then the above expression can be expanded into various cylindrical harmonic vectors,  $\mathbf{M}_{e_{n\eta}}$ ,  $\mathbf{N}_{e_{n\eta}}$ ,  $\mathbf{M}_{e_{n\eta}}^{(1)}$  and  $\mathbf{N}_{e_{n\eta}}^{(1)}$  [123] which define the electromagnetic field inside the optical fiber. In particular the vacuum Green's tensor is given by

$$\begin{aligned} \mathbf{G}^{(0)}(\mathbf{r}, \mathbf{r}', \omega) &= -\frac{\hat{\mathbf{r}}\hat{\mathbf{r}}\delta(\mathbf{r}-\mathbf{r}')}{k^2} \\ &+ \frac{i}{8\pi} \int_{-\infty}^{\infty} d\beta \sum_{n=0}^{\infty} \frac{2-\delta_{n,0}}{\eta^2} \begin{cases} \mathbf{M}_{e_{n\eta}}^{(1)}(\beta, \mathbf{r})\mathbf{M}_{e_{n\eta}}(-\beta, \mathbf{r}') + \mathbf{N}_{e_{n\eta}}^{(1)}(\beta, \mathbf{r})\mathbf{N}_{e_{n\eta}}(-\beta, \mathbf{r}'), & r > r' \\ \mathbf{M}_{e_{n\eta}}(\beta, \mathbf{r})\mathbf{M}_{e_{n\eta}}^{(1)}(-\beta, \mathbf{r}') + \mathbf{N}_{e_{n\eta}}(\beta, \mathbf{r})\mathbf{N}_{e_{n\eta}}^{(1)}(-\beta, \mathbf{r}'), & r < r', \end{cases} \end{aligned} \quad (1.57)$$

and the reflected and transmitted parts of Green's tensor are respectively as follow

$$\begin{aligned} \mathbf{G}^{(R)}(\mathbf{r}, \mathbf{r}', \omega) &= \frac{i}{8\pi} \int_{-\infty}^{\infty} d\beta \sum_{n=0}^{\infty} \frac{2 - \delta_{n,0}}{\eta^2} \left\{ \left[ A_R \mathbf{M}_{\varepsilon n \eta}^{(1)}(\beta, \mathbf{r}) + B_R \mathbf{N}_{\varepsilon n \eta}^{(1)}(\beta, \mathbf{r}) \right] \mathbf{M}_{\varepsilon n \eta}^{(1)}(-\beta, \mathbf{r}') \right. \\ &\quad \left. + \left[ C_R \mathbf{N}_{\varepsilon n \eta}^{(1)}(\beta, \mathbf{r}) + D_R \mathbf{M}_{\varepsilon n \eta}^{(1)}(\beta, \mathbf{r}) \right] \mathbf{N}_{\varepsilon n \eta}^{(1)}(-\beta, \mathbf{r}') \right\}, \end{aligned} \quad (1.58)$$

$$\begin{aligned} \mathbf{G}^{(T)}(\mathbf{r}, \mathbf{r}', \omega) &= \frac{i}{8\pi} \int_{-\infty}^{\infty} d\beta \sum_{n=0}^{\infty} \frac{2 - \delta_{n,0}}{\eta^2} \left\{ \left[ A_T \mathbf{M}_{\varepsilon n \eta_1}(\beta, \mathbf{r}) + B_T \mathbf{N}_{\varepsilon n \eta_1}(\beta, \mathbf{r}) \right] \mathbf{M}_{\varepsilon n \eta}^{(1)}(-\beta, \mathbf{r}') \right. \\ &\quad \left. + \left[ C_T \mathbf{N}_{\varepsilon n \eta_1}(\beta, \mathbf{r}) + D_T \mathbf{M}_{\varepsilon n \eta_1}(\beta, \mathbf{r}) \right] \mathbf{N}_{\varepsilon n \eta}^{(1)}(-\beta, \mathbf{r}') \right\}, \end{aligned} \quad (1.59)$$

with  $\eta = \sqrt{\varepsilon_1 k^2 - \beta^2}$ , where  $\beta$  and  $\eta$  are the longitudinal and transverse wave numbers, respectively. The cylindrical harmonic vectors are

$$\mathbf{M}_{\varepsilon n \eta}(\beta, \mathbf{r}) = \nabla \times \left[ J_n(\eta r) \frac{\cos(n\phi)}{\sin(n\phi)} e^{i\beta z} \hat{\mathbf{z}} \right], \quad (1.60a)$$

$$\mathbf{N}_{\varepsilon n \eta}(\beta, \mathbf{r}) = \frac{1}{\sqrt{\eta^2 + \beta^2}} \nabla \times \mathbf{M}_{\varepsilon n \eta}(\beta, \mathbf{r}), \quad (1.60b)$$

$$\mathbf{M}_{\varepsilon n \eta}^{(1)}(\beta, \mathbf{r}) = \nabla \times \left[ H_n^{(1)}(\eta r) \frac{\cos n\phi}{\sin n\phi} e^{i\beta z} \hat{\mathbf{z}} \right], \quad (1.60c)$$

$$\mathbf{N}_{\varepsilon n \eta}^{(1)}(\beta, \mathbf{r}) = \frac{1}{\sqrt{\eta^2 + \beta^2}} \nabla \times \mathbf{M}_{\varepsilon n \eta}^{(1)}(\beta, \mathbf{r})' \quad (1.60d)$$

By imposing Dirichlet boundary at  $r = a$  on Eqs. (1.56) and (1.60) the Fresnel coefficient can be obtained [123] and the expanded forms of the above equations are

$$\mathbf{M}_{\varepsilon n \eta}(\beta, \mathbf{r}) = \left[ \mp \frac{n J_n(\eta r)}{r} \frac{\sin(n\phi)}{\cos(n\phi)} \hat{\mathbf{r}} - \eta J_n'(\eta r) \frac{\cos(n\phi)}{\sin(n\phi)} \hat{\boldsymbol{\phi}} \right] e^{i\beta z},$$

$$\mathbf{N}_{\varepsilon n \eta}(\beta, \mathbf{r}) = \frac{e^{i\beta z}}{\sqrt{\eta^2 + \beta^2}} \left[ i\beta \eta J_n'(\eta r) \frac{\cos(n\phi)}{\sin(n\phi)} \hat{\mathbf{r}} \mp i\beta \frac{n J_n(\eta r)}{r} \frac{\sin(n\phi)}{\cos(n\phi)} \hat{\boldsymbol{\phi}} + \eta^2 J_n(\eta r) \frac{\cos(n\phi)}{\sin(n\phi)} \hat{\mathbf{z}} \right],$$

$$\mathbf{M}_{\varepsilon n \eta}^{(1)}(\beta, \mathbf{r}) = \left[ \mp \frac{n H_n^{(1)}(\eta r)}{r} \frac{\sin(n\phi)}{\cos(n\phi)} \hat{\mathbf{r}} - \eta H_n^{(1)'}(\eta r) \frac{\cos(n\phi)}{\sin(n\phi)} \hat{\boldsymbol{\phi}} \right] e^{i\beta z},$$

$$\mathbf{N}_{\varepsilon n \eta}^{(1)}(\beta, \mathbf{r}) = \frac{e^{i\beta z}}{\sqrt{\eta^2 + \beta^2}} \left[ i\beta \eta H_n^{(1)'}(\eta r) \frac{\cos(n\phi)}{\sin(n\phi)} \hat{\mathbf{r}} \mp i\beta \frac{n H_n^{(1)}(\eta r)}{r} \frac{\sin(n\phi)}{\cos(n\phi)} \hat{\boldsymbol{\phi}} + \eta^2 H_n^{(1)}(\eta r) \frac{\cos(n\phi)}{\sin(n\phi)} \hat{\mathbf{z}} \right].$$

At this point, all the essential and necessary mathematical tools and expressions are provided to study various quantities of a system which consists of atoms in free space or in the presence of a dielectric medium with flat or cylindrical geometry.

Since this thesis is based on publications, in the next chapter, I will give an example with extensive details of how to use one of the above methods to study a quantum hybrid system. I introduce a system which consists of two neutral atoms in the vicin-

ity of a flat dielectric medium and explain how to use the mode function method to calculate the spontaneous decay rate. Then, in chapters 2, 3 and 4, I will employ the mode function and the Green's function methods to study different feature of atoms in the presence of an ultra-thin optical nanofiber, such as the decay rate and the optical force stemming from a chiral recoil.

## Chapter 2

# Cooperative behavior of two atoms

In this chapter, I will introduce a hybrid atomic system that consists of two two-level atoms which are located in the vicinity of a dielectric medium and explain how to calculate their decay rate by using the mode function method. The decay rate into free space is modified due to the presence of the dielectric medium and the medium can also be used for channeling between the atoms. In fact, by carefully choosing the parameters, the presence of a surface can enhance the coupling between the atoms and an oscillatory behavior as a function of the distance between the atoms can be found, which also depends on the orientation of the electric dipole moments.

At first, I will use the mode expansion method to find the angular density and hence the spontaneous emission coefficients into the evanescent and radiation modes analytically and derive their dependence on the orientation of the electric dipole moments, position of the two atoms and the distance between them. Then, I will show that the relative position of the atoms as well as the orientations of the electric dipole moments with respect to the dielectric surface have a strong effect on the cooperative spontaneous emission coefficient into the evanescent and radiation modes. For the spontaneous emission coefficient into the radiation mode oscillatory behavior can be found, which reduces in amplitude as the distance between the atoms and the surface is increased. This is a reliable indicator that the presence of the dielectric medium acts like a communication channel, and modifies the coupling between the two atoms. I will also determine the conditions for maximum coupling between the atoms as a function of the orientation of the electric dipole moments, the distance between the atoms and the atom-interface distance.

The internal structure of the atoms is assumed to be a two-level system and, in contrast to previous studies [46], the atom is considered to have rotating induced dipoles, which implies complex dipole matrix elements [8, 44]. In this case the presence of a dielectric medium can have the profound effect of leading to an asymmetry in the collective spontaneous emission with respect to propagation of the emitted or absorbed light. Asymmetry in the direction of propagation of light due to the physical properties of the system is known as chirality of light. The chirality of emitted or absorbed light via the dielectric medium is an interesting feature of optical systems with numerous applications.

Recently Chang *et al.* [113] have demonstrated that trapped cold atoms next to a tapered nanofiber enhance the coupling between atoms and photons creating a virtual

high finesse cavity. This can possibly be considered as a result of collective effects within the cold atoms near atomic resonance. Lodahl *et al.* [47] have proposed using a photonic waveguide to create directional coupling between emitters, where the flow of information between emitters is unidirectional and dependent on the polarization of the light and the ordering position of the emitters. At the same time experiments have confirmed the possibility of a propagation-direction-dependent or chiral nature of light-matter interactions [47, 115].

In Section 2.1, I will describe the relevant modes of the field and introduce the Hamiltonian for the atom-field interaction. Section 2.2 presents the calculations for the angular density of the spontaneous emission rate and the coefficients of the spontaneous emission rate of atoms into the evanescent and radiation modes. In section 2.3, I will present the results for cooperative angular density of the evanescent and radiation mode for a few cases of different parameters. Section 2.4 is devoted to studying the asymmetry of collective spontaneous emission of the evanescent and radiation modes with respect to the propagation direction and the summary, conclusions and outlook of this work are presented in Section 2.5.

## 2.1 Quantization of the EM field near a dielectric surface

I consider the situation where the dielectric surface lies in the  $y - z$  plane and its interface with the vacuum is at  $x = 0$  (see Fig. 2.1). The second quantized formalism that I will use has been described in Section 1.2.1.

When two neutral atoms with electric dipole moments are close to the half-infinite dielectric medium, the interaction between the atoms can be expected to be enhanced by the evanescent modes of the dielectric medium. However, to be able to observe effects stemming from the presence of the dielectric medium, the distance between the atoms and the surface must be of the order of hundreds of nanometers. Let us define the position of the two atoms in Cartesian coordinates by  $\mathbf{r}_l \equiv \{x_l, y_l, z_l\}$ , where the index  $l = \{A, B\}$  labels atom  $A$  and atom  $B$ . The total Hamiltonian of the system then consists of the contributions from the electromagnetic field,  $\mathcal{H}_{\text{Field}}$ , from each individual atom,  $\mathcal{H}_{\text{Atom}_l}$ , and from the interaction between the atoms and the field,  $\mathcal{H}_{\text{Atom}_l-\text{Field}}$ , as

$$\mathcal{H} = \mathcal{H}_{\text{Field}} + \sum_{l=A,B} \mathcal{H}_{\text{Atom}_l} + \sum_{l=A,B} \mathcal{H}_{\text{Atom}_l-\text{Field}}. \quad (2.1)$$

This Hamiltonian can be used to calculate the spontaneous emission rates into the radiation and evanescent modes. To exclude the effect of the magnetic dipole moment on the interaction between the dielectric medium and the two atoms, the dielectric medium is assumed to be made from a non-magnetic material. To study the effect of dipole-dipole interaction between two atoms, it is preferable to have neutral atoms possessing strong electric dipole moments, such as the alkali atoms Rubidium or Cesium. While previously atoms were considered as point-like polarizable particles [124, 125], here I assume that they have internal structure and an electric dipole moment whose orientation undergoes changes due to the field polarization.



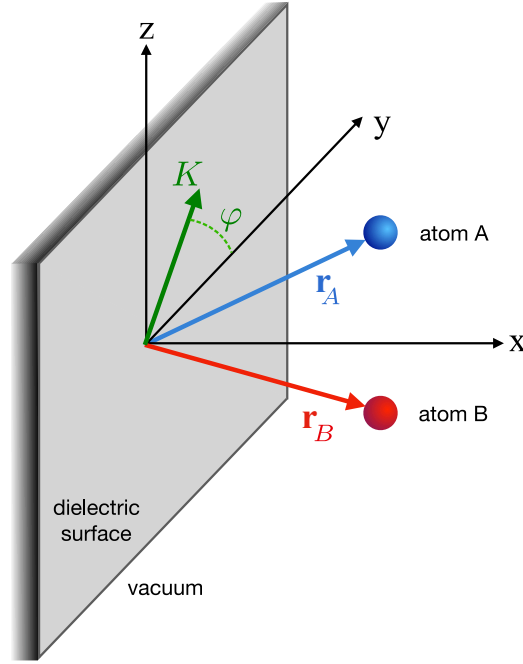


**Figure 2.1:** Schematic of two neutral atoms in the vicinity of a flat dielectric surface. The atoms are located in the positive half-space,  $x > 0$  at  $\mathbf{r}_A$  and  $\mathbf{r}_B$ . The projection of the vacuum field vector  $\mathbf{K}$  onto the interface is characterized by the angle  $\varphi$ .

Within the dipole approximation, the Hamiltonian for the atom-field interaction for a single atom is given by  $\mathcal{H}_{\text{Atom-Field}} = -\mathbf{D} \cdot \mathbf{E}$  for two atomic states  $|g\rangle$  and  $|e\rangle$  with the electric dipole moment  $\mathbf{D}$ . The latter can be written in terms of dipole matrix elements as

$$\mathbf{D} = \mathbf{d}_{gg}|g\rangle\langle g| + \mathbf{d}_{ge}|g\rangle\langle e| + \mathbf{d}_{eg}|e\rangle\langle g| + \mathbf{d}_{ee}|e\rangle\langle e|, \quad (2.2)$$

where  $\mathbf{d} \equiv \mathbf{d}_{eg} = \langle e|\mathbf{D}|g\rangle$ . Since  $|e\rangle$  and  $|g\rangle$  can be complex and either odd or even eigen-functions of the system, their overlap with the electric dipole element is zero, implying the same for the dipole matrix elements. It is immediately clear that  $\mathbf{d}_{gg} = \mathbf{d}_{ee} = 0$  and hence the electric dipole moment can be written as

$$\mathbf{D} = \mathbf{d}\sigma^\dagger + \mathbf{d}^*\sigma, \quad (2.3)$$

where the operators  $\sigma^\dagger = |e\rangle\langle g|$  and  $\sigma = |g\rangle\langle e|$  are raising and lowering operators. It is important to point out that the total electric dipole moment  $\mathbf{D}$  of a neutral atom is always a real quantity, however, in the interaction picture it can have complex components, implying that the atomic electric dipole rotates with a frequency of  $\omega_l$ . This means that in the interaction picture it can be written as

$$\mathbf{D}_{\text{int}} = \mathbf{d}\sigma^\dagger e^{i\omega_l t} + \mathbf{d}^*\sigma e^{-i\omega_l t}. \quad (2.4)$$

The complex nature of the electric dipole moment can be understood by realizing that the atom does not have a permanent dipole moment, and that the electric dipole is in fact rotating with a frequency of  $\omega_l$ . To see the consequences this has for the interaction

between two atoms placed in front of dielectric surface, I use the expressions for the electric dipole moment operator  $\mathbf{D}_{\text{int}}$  and for the electric field from Eq. (1.5), and apply the mode function method [8, 126] to write the atom-field interaction Hamiltonian in the interaction picture as

$$\mathcal{H}_{\text{int}} = - \sum_{l,\alpha} A \left( \mathbf{d}_l^* \cdot \mathbf{U}_\alpha^*(x) \sigma_l a_\alpha e^{-i(\omega+\omega_l)t} e^{-i\mathbf{K}\cdot\mathbf{R}_l} + \mathbf{d}_l \cdot \mathbf{U}_\alpha(x) \sigma_l^\dagger a_\alpha^\dagger e^{-i(\omega-\omega_l)t} e^{i\mathbf{K}\cdot\mathbf{R}_l} + \text{h.c.} \right), \quad (2.5)$$

where  $\mathbf{R}_l = (0, y, z)$  is the projection of the position of the atoms onto the surface of the dielectric medium. Employing the rotation wave approximation (RWA), which assumes that fast rotating terms of the form  $(\omega + \omega_l)$  average out over long integration periods, the atom-field interaction Hamiltonian can be written as

$$\mathcal{H}_{\text{int}} = - \sum_{l,\alpha} A \left( \mathbf{d}_l \cdot \mathbf{U}_\alpha(x) \sigma_l^\dagger a_\alpha e^{i(\omega_l-\omega)t} e^{i\mathbf{K}\cdot\mathbf{R}_l} + \mathbf{d}_l^* \cdot \mathbf{U}_\alpha^*(x) \sigma_l a_\alpha^\dagger e^{-i(\omega_l-\omega)t} e^{-i\mathbf{K}\cdot\mathbf{R}_l} \right). \quad (2.6)$$

This can be made more compact by writing

$$\mathcal{H}_{\text{int}} = -i\hbar \sum_{l,\alpha} \left( G_{\alpha,l} \sigma_l^\dagger a_\alpha e^{i(\omega_l-\omega)t} + G_{\alpha,l}^* \sigma_l a_\alpha^\dagger e^{-i(\omega_l-\omega)t} \right), \quad (2.7)$$

where the  $G_{\alpha,l}$  are coupling coefficients defined as

$$G_{\alpha,l} = \frac{k}{4\pi\sqrt{\pi\epsilon_0\hbar}\beta_j} e^{i\mathbf{K}\cdot\mathbf{R}_l} (\mathbf{d}_l \cdot \mathbf{U}_\alpha(x)). \quad (2.8)$$

In the next section I show how to calculate the coefficient of the spontaneous emission rates into the evanescent and radiation modes within the above model.

## 2.2 Spontaneous emission rate

To derive the microscopic dynamical equations for the spontaneous radiative decay of two atoms I will use the mode function approach and the Weisskopf-Wigner formalism [127]. The coefficients of spontaneous emission into the evanescent and radiation modes are calculated by using the Liouville-von Neumann equation, which determines the time evolution of the reduced density function of the atoms  $\rho$  in the interaction picture [8, 128]. Substitution of  $\mathcal{H}_{\text{int}}$  from Eq. (2.7) into this equation of motion and further simplifying the resulting expression gives

$$\frac{d\rho}{dt} = \sum_{l,l'} \left[ \frac{\gamma^{(l')}}{2} ([\rho, \sigma_l^\dagger \sigma_{l'}] - [\rho, \sigma_l \sigma_{l'}^\dagger]) + i \Omega^{(l')} ([\rho, \sigma_l^\dagger \sigma_{l'}] + [\rho, \sigma_l \sigma_{l'}^\dagger]) \right], \quad (2.9)$$

where  $\gamma^{(l')}$  and  $\Omega^{(l')}$  are the coefficients of the cooperative spontaneous emission rate and the frequency shift, respectively. These coefficients have previously been calculated for a single atom ( $l = l'$ ) near a dielectric surface [128]. For our purpose, the time

evolution of the creation and annihilation operator can be written as [8]

$$a_\alpha^\dagger(t) = a_\alpha^\dagger(t_0) + \sum_l \int_{t_0}^t G_{\alpha,l} \sigma_l^\dagger(t') e^{i(\omega_l - \omega)t'} dt', \quad (2.10)$$

and I assume that the field is initially in the vacuum state. I also assume that the time evolution interval  $(t - t_0)$  and the characteristic atomic life time  $\tau_a$  are greater than both the optical period  $2\pi/\omega_0$  and the light propagation time  $|\mathbf{r}_l - \mathbf{r}_{l'}|/c$  between the two atoms. Using the Markov approximation,  $\sigma_j(t') = \sigma_j(t)$ , and going to the limit  $t - t_0 \rightarrow \infty$ , Eq. (2.10) simplifies to

$$a_\alpha^\dagger(t) = \sum_l G_{\alpha,l} \sigma_l^\dagger(t) e^{i(\omega_l - \omega)t} \left[ \pi \delta(\omega_l - \omega) - i\mathcal{P} \frac{1}{\omega_l - \omega} \right], \quad (2.11)$$

with  $a_\alpha^\dagger(0) = 0$ . From this the coefficient of the cooperative spontaneous emission rate can be calculated as

$$\gamma^{(ll')} = 2\pi \sum_\alpha G_{\alpha,l} G_{\alpha,l'}^*, \quad (2.12)$$

which can then be split into a sum for the rate into the evanescent modes,  $\gamma_{\text{evan}}^{(ll')}$ , and into the radiation modes,  $\gamma_{\text{rad}}^{(ll')}$ , as

$$\gamma^{(ll')} = \gamma_{\text{evan}}^{(ll')} + \gamma_{\text{rad}}^{(ll')}. \quad (2.13)$$

For  $l = l'$  this expression gives the total coefficient of spontaneous emission for a single atom near the dielectric surface [8], however when  $l \neq l'$  it refers to the collective effects of multiple atoms near the dielectric surface. The calculation of the coefficient of spontaneous emission is dependent on the angular density of the collective decay coefficient which is given by

$$F^{(ll')} = F_{\text{evan}}^{(ll')} + F_{\text{rad}}^{(ll')}. \quad (2.14)$$

This will be discussed in more detail in the next subsection.

### 2.2.1 Spontaneous emission into the evanescent mode

The coefficient for the cooperative spontaneous emission of the atoms into the evanescent mode can be determined as

$$\begin{aligned} \gamma_{\text{evan}}^{(ll')} &= 2\pi \sum_{\substack{\alpha \\ k_0 < K < k_0 n_1}} G_{\alpha,l} G_{\alpha,l'}^* \\ &= 2\pi \sum_{q=s,p} \int_{k_0}^{k_0 n_1} K dK \int_0^{2\pi} G_{\omega_0 \mathbf{K} q 1, l} G_{\omega_0 \mathbf{K} q 1, l'}^* d\phi, \end{aligned} \quad (2.15)$$

where the different polarization modes of the vacuum fields are embedded in the expression for the coupling coefficient  $G_{\alpha,l}$  and labelled as  $q = s, p$  for  $s$  and  $p$  polarization.

The subscript label 1 indicates that the mode function in the dielectric medium 1 is responsible for the evanescent modes. It is important to note that for the evanescent mode, the vacuum wave vector  $\mathbf{K}$  lies in the range  $k_0 < K < k_0 n_1$  with  $k_0 = \omega_0/c$ , which guarantees total internal reflection. Next, the total coefficient is split into contributions from the two different polarisation modes,  $\gamma_{\text{evan}}^{(ll')} = \gamma_{\text{evan},s}^{(ll')} + \gamma_{\text{evan},p}^{(ll')}$ , where  $\gamma_{\text{evan},s}^{(ll')}$  and  $\gamma_{\text{evan},p}^{(ll')}$  are the coefficients of spontaneous emission into the evanescent mode for  $s$  and  $p$  polarization respectively. For simplicity, let us rewrite Eq. (2.15) in terms of the cooperative angular density of the spontaneous emission rate into the evanescent mode  $F_{\text{evan}}^{(ll')}(\xi, \phi)$  using the new variables  $\kappa = K/k_0$  and  $\xi = \sqrt{|1 - \kappa^2|}$  [8]

$$\gamma_{\text{evan},q}^{(ll')} = \frac{d_l d_{l'} k_0^3}{3\pi\epsilon_0 \hbar} \int_0^{\sqrt{n_1^2-1}} \xi d\xi \int_0^{2\pi} F_{\text{evan},q}^{(ll')}(\xi, \phi) d\phi. \quad (2.16)$$

Here, I have used the decomposition of  $F_{\text{evan}}^{(ll')}(\xi, \phi)$  into its polarisation components  $s$  and  $p$  as  $F_{\text{evan}}^{(ll')} = F_{\text{evan},s}^{(ll')} + F_{\text{evan},p}^{(ll')}$ , where each term is given as

$$F_{\text{evan},s}^{(ll')}(\xi, \phi) = \frac{3}{4\pi\xi} T_s e^{i\sqrt{1+\xi^2}\mathbf{k}_0 \cdot (\mathbf{R}_l - \mathbf{R}_{l'})} e^{-k_0\xi(x_l+x_{l'})} \left[ u_{yl}u_{y'l'}^* \sin^2 \phi + u_{zl}u_{z'l'}^* \cos^2 \phi - [u_{yl}^*u_{z'l'} + u_{zl}^*u_{y'l'}] \sin \phi \cos \phi \right], \quad (2.17)$$

$$F_{\text{evan},p}^{(ll')}(\xi, \phi) = \frac{3}{4\pi\xi} T_p e^{i\sqrt{1+\xi^2}\mathbf{k}_0 \cdot (\mathbf{R}_l - \mathbf{R}_{l'})} e^{-k_0\xi(x_l+x_{l'})} \left[ (1 + \xi^2)u_{xl}u_{x'l'}^* + \xi^2 u_{yl}u_{y'l'}^* \cos^2 \phi + \xi^2 u_{zl}u_{z'l'}^* \sin^2 \phi + \xi^2 (u_{yl}u_{z'l'}^* + u_{zl}u_{y'l'}^*) \sin \phi \cos \phi + i\xi \sqrt{1 + \xi^2} \left( (u_{xl}u_{y'l'}^* - u_{yl}u_{x'l'}^*) \cos \phi + (u_{xl}u_{z'l'}^* - u_{zl}u_{x'l'}^*) \sin \phi \right) \right]. \quad (2.18)$$

It is worth remembering that the dipole moments of the atoms are written with respect to their orientations in cartesian coordinates as  $\mathbf{d}_l = |d|\mathbf{u}_l$ , where  $\mathbf{u}_l = (u_{xl}, u_{yl}, u_{zl})$  can be a complex vector and  $\phi = \arctan(\frac{K_z}{K_y})$  is the angle between its components in the  $y$  and  $z$  directions. The coefficients  $T_s = \frac{\xi |t_{12}^s|^2}{2\eta}$  and  $T_p = \frac{\xi |t_{12}^p|^2}{2\eta}$  are the transmission coefficients for the  $s$  and  $p$  polarization, respectively, with the coefficients  $t_{12}^s$  and  $t_{12}^p$  as defined previously in (1.8) (see section 1.2.2) [8]. If the electric dipole matrix elements have complex values, terms of the form  $(u_{xl}u_{y'l'}^* - u_{yl}u_{x'l'}^*)$  and  $(u_{xl}u_{z'l'}^* - u_{zl}u_{x'l'}^*)$  are in general non-zero and hence the complex nature of dipole matrix elements has an effect on the spontaneous emission properties of the atoms. By using Eq. (2.16), the total coefficient of cooperative spontaneous emission into the evanescent mode can be simplified as

$$\gamma_{\text{evan}}^{(ll')} = \frac{3}{4} \gamma_0^{(ll')} \int_0^{\sqrt{n_1^2-1}} d\xi e^{i\sqrt{1+\xi^2}\mathbf{k}_0 \cdot (\mathbf{R}_l - \mathbf{R}_{l'})} e^{-k_0\xi(x_l+x_{l'})} \left[ 2(1 + \xi^2)T_p u_{xl}u_{x'l'}^* + (T_s + \xi^2 T_p)u_{yl}u_{y'l'}^* + (T_s + \xi^2 T_p)u_{zl}u_{z'l'}^* \right], \quad (2.19)$$

where the coefficient  $\gamma_0^{(l'l')} = \frac{d_l d_{l'} k_0^3}{3\pi\epsilon_0\hbar}$  is the coefficient of spontaneous emission for two atoms in free space. It can be seen from the above equation that the cooperative spontaneous emission coefficient for the evanescent mode,  $\gamma_{evan}^{(l'l')}$ , depends on the respective orientations  $\mathbf{u}_l$  and  $\mathbf{u}_{l'}$  of the electric dipole moments and on the relative position of the two atoms near the dielectric surface.

## 2.2.2 Spontaneous emission into the radiation mode

For the spontaneous emission into the available radiation modes both polarisations in both media need to be considered,  $qi = \{s1, s2, p1, p2\}$ , where the indices 1 and 2 refers to the source of the vacuum modes. For example, for  $qi = s1$  the mode function  $\mathbf{U}_{\omega\mathbf{K}s1}(x)$  contains all vacuum mode in  $x > 0$  and their reflection from the vacuum-dielectric interface [8]. Let us calculate the coefficient of cooperative spontaneous emission into the radiation modes which is given by

$$\gamma_{\text{rad}}^{(l'l')} = 2\pi \sum_{q=s,p} \sum_{i=1,2} \int_0^{k_0} K dK \int_0^{2\pi} G_{\omega_0\mathbf{K}qi,l} G_{\omega_0\mathbf{K}qi,l'}^* d\phi, \quad (2.20)$$

where the wave vector  $K$  in this case lies in the range  $0 \leq K \leq k_0$ . Similar to the discussion for the evanescent modes above, it is useful to write Eq. (2.20) in terms of the cooperative angular density of the spontaneous emission rate into the radiation mode  $F_{\text{rad},qj}^{(l'l')}(\xi, \phi)$  as

$$\gamma_{\text{rad},qj}^{(l'l')} = \gamma_0^{(l'l')} \int_0^1 \xi d\xi \int_0^{2\pi} F_{\text{rad},qj}^{(l'l')}(\xi, \phi) d\phi, \quad (2.21)$$

with

$$\gamma_{\text{rad}}^{(l'l')} = \sum_{q=s,p} \sum_{j=1,2} \gamma_{\text{rad},qj}^{(l'l')}. \quad (2.22)$$

Again,  $F_{\text{rad},qj}^{(l'l')}(\xi, \phi)$  can be split into its polarisation components  $F_{\text{rad}}^{(l'l')} = F_{\text{rad},s}^{(l'l')} + F_{\text{rad},p}^{(l'l')}$ , where  $F_{\text{rad},s}^{(l'l')} = F_{\text{rad},s1}^{(l'l')} + F_{\text{rad},s2}^{(l'l')}$  and  $F_{\text{rad},p}^{(l'l')} = F_{\text{rad},p1}^{(l'l')} + F_{\text{rad},p2}^{(l'l')}$ . This is because the angular density of the collective decay coefficient of radiation mode for  $s$  polarization,  $\gamma_{\text{rad},s}^{(l'l')}$ , has contributions from two sources: the first one originating from the  $s$  polarization of the field in the space  $x > 0$  and its reflection from the dielectric surface, and the second one from the transmitted  $s$  polarized field which travels from  $x < 0$  towards the positive  $x$  space. Similarly, for the case of  $p$  polarization we split  $F_{\text{rad},p}^{(l'l')}$  into  $F_{\text{rad},p1}^{(l'l')}$  and  $F_{\text{rad},p2}^{(l'l')}$ . The expression  $F_{\text{rad}}^{(l'l')}$ , after rigorous simplification, can be written for  $s$  polarization as

$$F_{\text{rad},s}^{(l'l')} = \frac{3}{4\pi\xi} e^{i\sqrt{1-\xi^2}\mathbf{k}_0 \cdot (\mathbf{R}_l - \mathbf{R}_{l'})} \left[ \cos(k_0\xi(x_l - x_{l'})) + r_s \cos(k_0\xi(x_l + x_{l'})) \right] \times \left[ u_{yl}u_{y'l'}^* \sin^2 \phi - (u_{yl}u_{z'l'}^* + u_{zl}u_{y'l'}^*) \sin \phi \cos \phi + u_{zl}u_{z'l'}^* \cos^2 \phi \right], \quad (2.23)$$

and for  $p$  polarization

$$\begin{aligned}
F_{\text{rad},p}^{(ll')} &= \frac{3}{4\pi\xi} e^{i\sqrt{1-\xi^2}\mathbf{k}_0\cdot(\mathbf{R}_l-\mathbf{R}_{l'})} \left[ \cos(k_0\xi(x_l-x_{l'})) \{ u_{xl}u_{xl'}^*(1-\xi^2) + u_{yl}u_{yl'}^*\xi^2 \cos^2\phi \right. \\
&\quad \left. + u_{zl}u_{zl'}^*\xi^2 \sin^2\phi + \xi^2(u_{yl}^*u_{zl'} + u_{zl}^*u_{yl'}) \sin\phi \cos\phi \right] \\
&\quad + i\xi\sqrt{1-\xi^2} \sin(k_0\xi(x_l-x_{l'})) \{ (u_{xl}u_{yl'}^* - u_{yl}u_{xl'}^*) \cos\phi + (u_{xl}u_{zl'}^* - u_{zl}u_{xl'}^*) \sin\phi \} \\
&\quad + \frac{3}{4\pi\xi} e^{i\sqrt{1-\xi^2}\mathbf{k}_0\cdot(\mathbf{R}_l-\mathbf{R}_{l'})} r_p \left[ \cos(k_0\xi(x_l+x_{l'})) \{ u_{xl}u_{xl'}^*(1-\xi^2) - u_{yl}u_{yl'}^*\xi^2 \cos^2\phi \right. \\
&\quad \left. - u_{zl}u_{zl'}^*\xi^2 \sin^2\phi - \xi^2(u_{yl}^*u_{zl'} + u_{zl}^*u_{yl'}) \sin\phi \cos\phi \right] \\
&\quad \left. + i\xi\sqrt{1-\xi^2} \sin(k_0\xi(x_l+x_{l'})) \{ (u_{xl}u_{yl'}^* - u_{yl}u_{xl'}^*) \cos\phi + (u_{xl}u_{zl'}^* - u_{zl}u_{xl'}^*) \sin\phi \} \right], \tag{2.24}
\end{aligned}$$

where  $\frac{\xi|t_{12}^s|^2}{\eta} = 1 - r_s^2$  and  $\frac{\xi|t_{12}^p|^2}{\eta} = 1 - r_p^2$  are the transmission coefficients of the  $s$  and  $p$  polarization for the radiation mode. The final expression for the coefficient of cooperative spontaneous emission into the radiation modes is then given by

$$\begin{aligned}
\gamma_{\text{rad}}^{(ll')} &= \frac{3}{4}\gamma_0^{(ll')} \int_0^1 d\xi e^{i\sqrt{1-\xi^2}\mathbf{k}_0\cdot(\mathbf{R}_l-\mathbf{R}_{l'})} \left[ \cos(k_0\xi(x_l-x_{l'})) \{ 2u_{xl}u_{xl'}^*(1-\xi^2) + (u_{yl}u_{yl'}^* \right. \\
&\quad \left. + u_{zl}u_{zl'}^*)(1+\xi^2) \} + \cos(k_0\xi(x_l+x_{l'})) \{ 2r_p u_{xl}u_{xl'}^*(1-\xi^2) + u_{yl}u_{yl'}^*(r_s - r_p\xi^2) \right. \\
&\quad \left. + u_{zl}u_{zl'}^*(r_s - r_p\xi^2) \} \right], \tag{2.25}
\end{aligned}$$

and it can be clearly seen that this quantity depends on the respective orientation  $\mathbf{u}_l$  and  $\mathbf{u}_{l'}$  of the electric dipole moments and the relative position of the two atoms.

## 2.3 Cooperative angular density

The absolute value of the cooperative angular density  $|F_{\text{evan/rad}}^{(AB)}(\xi, \phi)|$  of the spontaneous emission into the evanescent and radiation modes is plotted in Fig. 2.2, with respect to the normalized in plane components of the vacuum field  $\kappa_y$  and  $\kappa_z$  for various orientations of the electric dipole moment of the atoms,  $\mathbf{u}_A$  and  $\mathbf{u}_B$ . In fact, we choose to plot the absolute values because the cooperative angular densities can have a finite imaginary part due to the exponential  $e^{i\sqrt{1\pm\xi^2}\mathbf{k}_0\cdot(\mathbf{R}_A-\mathbf{R}_B)}$  term, which means that the essential features of the complex nature of the dipole matrix elements can already be clearly seen from the absolute values. The variable  $\kappa = K/k_0$  is the normalized in-plane component of the vacuum field, with  $\kappa_y$  and  $\kappa_z$  being the projections of  $\kappa$  onto the  $y$  and  $z$  axes, respectively. For our calculations we choose two identical Cesium atoms where the  $D_2$  line has a transition wavelength of  $\lambda_0 = 852$  nm and assume that they have a fixed distance  $|z_A - z_B| = 200$  nm between them and a distance from the dielectric surface of  $x_A = x_B = 200$  nm.

The rows (I) to (IV) in Fig. 2.2 show results for the cases where the orientation of dipole polarization vectors  $\mathbf{u}_A$  and  $\mathbf{u}_B$  are  $\mathbf{u}_A = \mathbf{u}_B = \hat{x}$ ,  $\mathbf{u}_A = \mathbf{u}_B = \hat{z}$ ,  $\mathbf{u}_A = \mathbf{u}_B =$

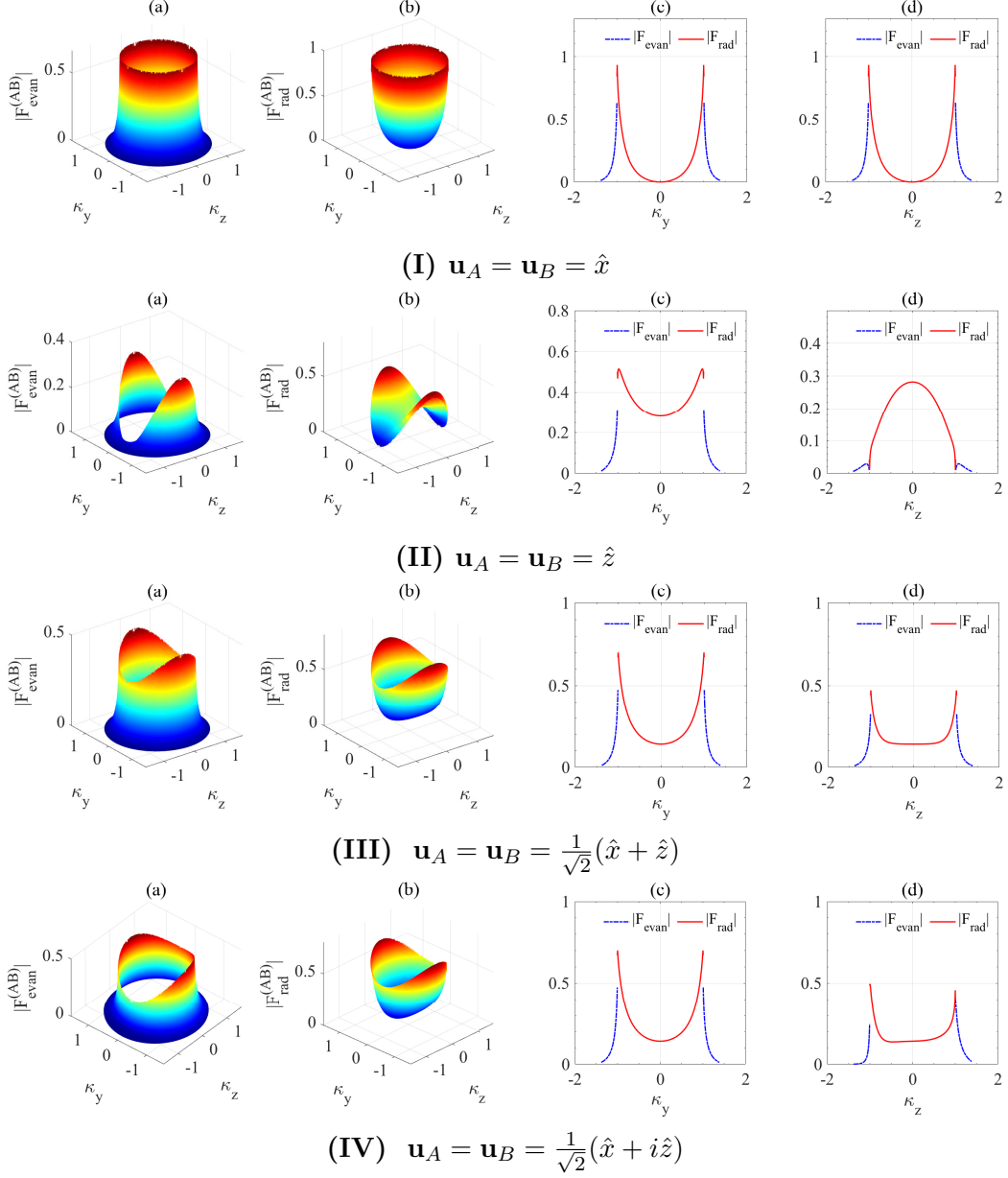


**Figure 2.2:** Absolute values of the cooperative angular densities  $|F_{\text{evan}}^{(AB)}|$  and  $|F_{\text{rad}}^{(AB)}|$  of the spontaneous emission into the evanescent and radiation modes for atoms with the electric dipole moments  $\mathbf{u}_A$  and  $\mathbf{u}_B$ . The atoms are separated by 200 nm from each other, and the atom-interface distance is  $x_A = x_B = 200$  nm. (I)  $\mathbf{u}_A = \mathbf{u}_B = \hat{x}$ , (II)  $\mathbf{u}_A = \mathbf{u}_B = \hat{z}$ , (III)  $\mathbf{u}_A = \mathbf{u}_B = \frac{1}{\sqrt{2}}(\hat{x} + \hat{z})$ , and (IV)  $\mathbf{u}_A = \mathbf{u}_B = \frac{1}{\sqrt{2}}(\hat{x} + i\hat{z})$ . (a) Absolute values of the angular density of the collective decay coefficient into the evanescent modes, (b) into the radiation modes, (c) the projection of the angular densities into the  $\kappa_y$ , and (d)  $\kappa_z$  direction.

$\frac{1}{\sqrt{2}}(\hat{x} + \hat{z})$  and  $\mathbf{u}_A = \mathbf{u}_B = \frac{1}{\sqrt{2}}(\hat{x} + i\hat{z})$ , respectively. One can immediately see that changing the orientation of the electric dipole moments with respect to the dielectric surface strongly impacts the profile of the cooperative angular density for evanescent

and radiation modes. If the dipole moments are aligned along the  $x$ -axis (see Fig. 2.2 (I)), both angular densities are cylindrically symmetric functions of  $\kappa$ . For the cases where  $\mathbf{u}$  is aligned along the  $z$ -axis (Fig. 2.2 (II)) and where  $u$  is aligned at a nonzero angle with respect to the  $x$ -axis in the  $x - z$  plane (Fig. 2.2 (III)), the cooperative angular densities are no longer cylindrically symmetric. However, as it is evident from panels (c) and (d) in Figs. 2.2 (II) and (III),  $|F_{\text{evan}}^{(AB)}|$  and  $|F_{\text{rad}}^{(AB)}|$  stay symmetric under the transformation  $\kappa_y \rightarrow -\kappa_y$  and  $\kappa_z \rightarrow -\kappa_z$ , which implies their symmetry under the transformation  $\kappa \rightarrow -\kappa$ .

If  $\mathbf{u}_A$  and  $\mathbf{u}_B$  are a complex vectors (see Fig. 2.2 (IV)), the cooperative angular densities have noticeably distinct angular density profiles compared to the case when the dipole moments are real. Panels (c) and (d) show that  $|F_{\text{evan}}^{(AB)}|$  and  $|F_{\text{rad}}^{(AB)}|$  are symmetric under the transformation  $\kappa_y \rightarrow -\kappa_y$  but not symmetric under the transformation  $\kappa_z \rightarrow -\kappa_z$ . This implies that they are asymmetric under the transformation  $\kappa \rightarrow -\kappa$ . This asymmetry is the result of the complex nature of the atomic dipole matrix elements and one of the main results of this chapter.

The asymmetry is also visible in the coefficients of cooperative spontaneous emission into the evanescent and radiation modes, which can be determined using Eqs. (2.19) and (2.25). These coefficients and the total cooperative spontaneous emission coefficient,  $\gamma^{(AB)} = \gamma_{\text{evan}}^{(AB)} + \gamma_{\text{rad}}^{(AB)}$  are plotted in Fig. 2.3 as a function of the distance of the two atoms from the dielectric surface for different values of inter-atomic separation  $|z_A - z_B|$ . Note that these coefficients are normalised to the respective free space value  $\gamma_0^{(AB)} = \frac{d_A d_B k_0^3}{3\pi\epsilon_0\hbar}$ .

In Fig. 2.3 the results for different dipole orientations are shown, when the inter-atomic separation  $|z_A - z_B|$  has four possible values and both atoms are simultaneously moved away from the dielectric surface medium from  $x_A = x_B = 0 - 800$  nm. In all of these cases, the orientations of the electric dipole moment of the atoms is varied as (I)  $\mathbf{u}_A = \mathbf{u}_B = \hat{x}$ , (II)  $\mathbf{u}_A = \mathbf{u}_B = \hat{z}$ , (III)  $\mathbf{u}_A = \mathbf{u}_B = \frac{1}{\sqrt{2}}(\hat{x} + \hat{z})$  and (IV)  $\mathbf{u}_A = \mathbf{u}_B = \frac{1}{\sqrt{2}}(\hat{x} + i\hat{z})$ . The results of the cases  $\mathbf{u}_A = \mathbf{u}_B = \frac{1}{\sqrt{2}}(\hat{x} + \hat{z})$  and  $\mathbf{u}_A = \mathbf{u}_B = \frac{1}{\sqrt{2}}(\hat{x} + i\hat{z})$  are the same and shown in Fig. 2.3 (III). As can be seen from Fig. 2.3, the cooperative coefficients of spontaneous emission into the evanescent mode, the radiation mode and the total cooperative spontaneous emission coefficient for the two atoms acquire finite values due to the presence of the dielectric surface. This indicates that the presence of the dielectric surface is responsible for the coupling between the two atoms placed closed to it.

For all cases of dipole moment orientation, the cooperative coefficient of spontaneous emission into the evanescent mode decays rapidly to zero when the atom-interface distance is increased, and the cooperative coefficient of spontaneous emission into the radiation mode shows oscillatory behavior with increasing atom-interface distance. For a fixed value of interatomic separation  $|z_A - z_B|$ , the dashed black lines in Fig. 2.3 for the normalized total cooperative spontaneous rate  $\gamma^{(AB)}/\gamma_0$  show both an increase  $\gamma^{(AB)}/\gamma_0 > 1$ , and a decrease  $\gamma^{(AB)}/\gamma_0 < 1$  in magnitude, depending on the distance between the atom and the dielectric interface. When both of the atoms are placed at the same position (corresponding to the limiting case of one atom near a dielectric surface discussed in [8]), the enhancement is maximal and as the distance between the two atoms is increased, it falls off. The reason for the enhancement of the rate can be



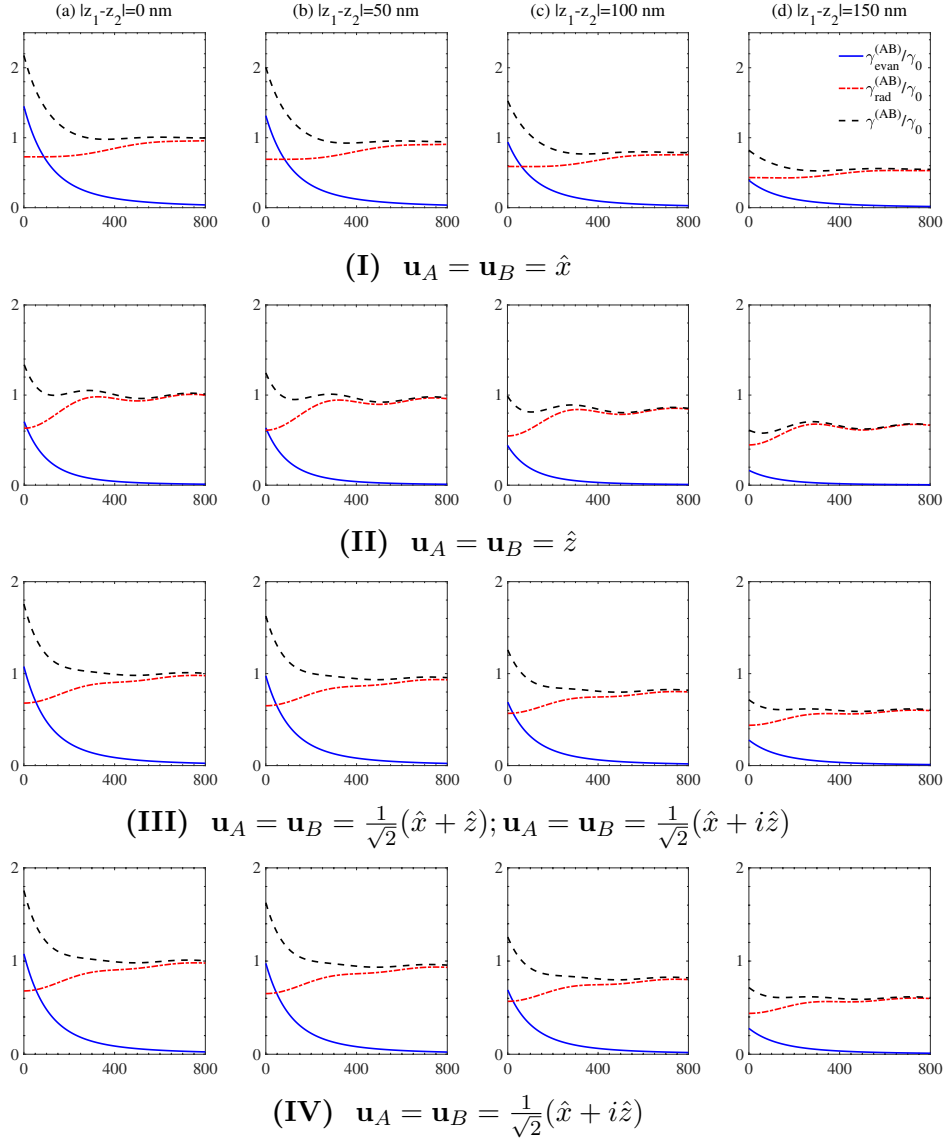


**Figure 2.3:** Coefficients of spontaneous emission into the evanescent modes  $\gamma_{\text{evan}}^{(AB)}/\gamma_0$  (blue solid line), the radiation modes  $\gamma_{\text{rad}}^{(AB)}/\gamma_0$  (red dashed-dotted line) and their sum  $\gamma^{(AB)}/\gamma_0$  (black dashed line) as a function of atom-interface distance for varying inter-atomic separation (a)  $|z_1 - z_2| = 0$  nm, (b)  $|z_1 - z_2| = 50$  nm, (c)  $|z_1 - z_2| = 100$  nm and (d)  $|z_1 - z_2| = 150$  nm and varying orientation of dipole moments (I)  $\mathbf{u}_A = \mathbf{u}_B = \hat{x}$ , (II)  $\mathbf{u}_A = \mathbf{u}_B = \hat{z}$ , (III)  $\mathbf{u}_A = \mathbf{u}_B = \frac{1}{\sqrt{2}}(\hat{x} + \hat{z})$ , and (IV)  $\mathbf{u}_A = \mathbf{u}_B = \frac{1}{\sqrt{2}}(\hat{x} + i\hat{z})$ .

seen to be mainly due to the presence of the evanescent modes. The tight confinement of the evanescent modes in the  $+x$  direction is responsible for the rapid decay of  $\gamma_{\text{evan}}^{(AB)}$ . On the other hand, the oscillatory behaviour of  $\gamma_{\text{rad}}^{(AB)}$  and consequently of  $\gamma^{(AB)}$  is mainly due to interference between the emitted and reflected fields.

The dashed dotted red lines in Fig. 2.3 show oscillatory behaviour when atoms are located close to the dielectric surface while  $\gamma_{\text{rad}}^{(AB)}/\gamma_0$  reaches to its asymptotic value as the distance between atoms and dielectric surface increases. The exact magnitude also depends on the distance between the two atoms. For the case of large distance from the

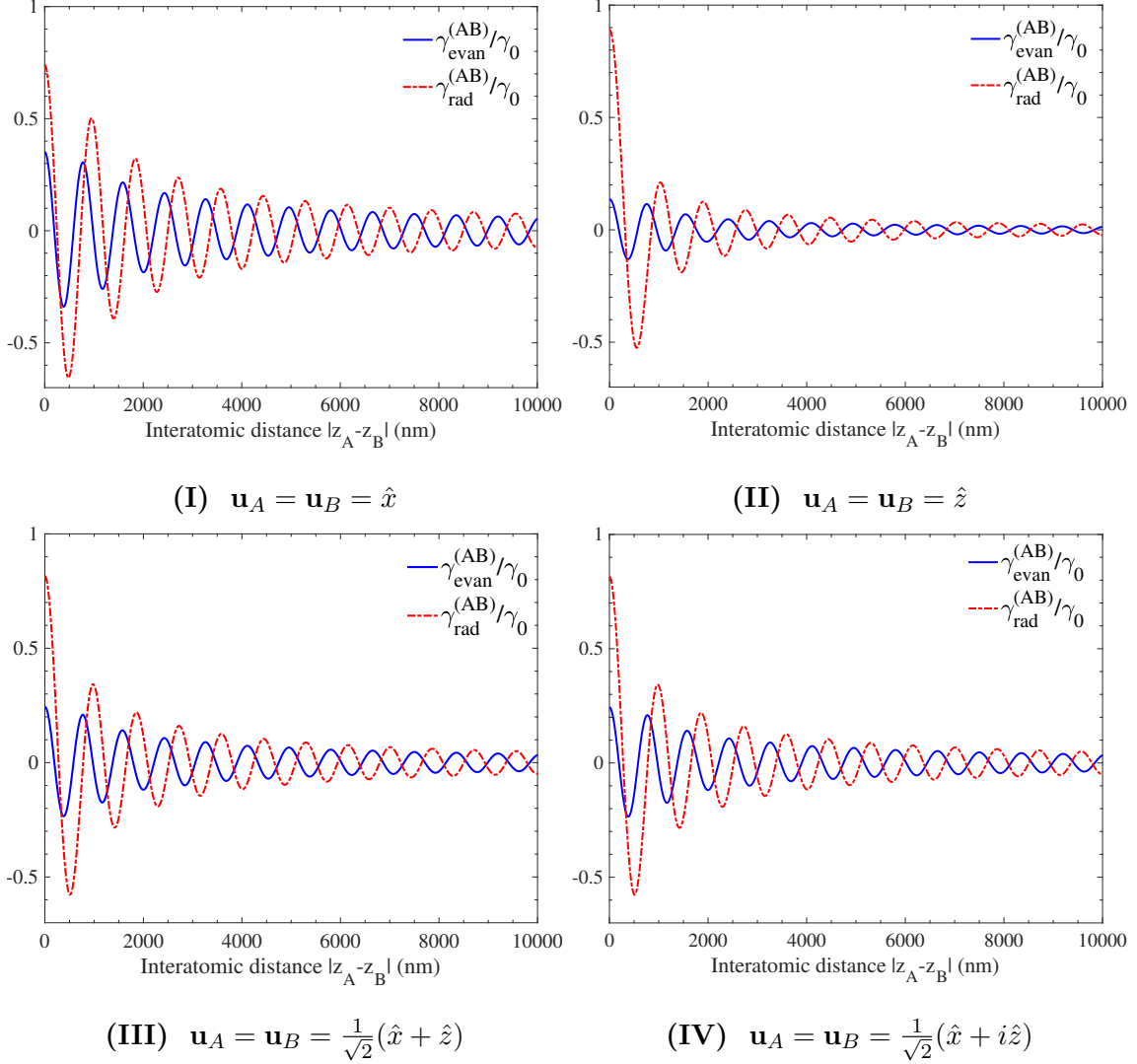


**Figure 2.4:** Coefficients of spontaneous emission into the evanescent (blue solid lines) and radiation (red dashed-dotted lines) modes for  $x_A = x_B = 200$  nm as a function of the inter-atomic separation  $|z_A - z_B|$  (I)  $\mathbf{u}_A = \mathbf{u}_B = \hat{x}$ , (II)  $\mathbf{u}_A = \mathbf{u}_B = \hat{z}$ , (III)  $\mathbf{u}_A = \mathbf{u}_B = \frac{1}{\sqrt{2}}(\hat{x} + \hat{z})$  and (IV)  $\mathbf{u}_A = \mathbf{u}_B = \frac{1}{\sqrt{2}}(\hat{x} + i\hat{z})$ .

dielectric surface, there is only contribution from the radiation mode  $\gamma^{(AB)} = \gamma_{\text{rad}}^{(AB)}$ , and the evanescent mode  $\gamma_{\text{evan}}^{(AB)}$  vanishes completely.

Fig. 2.4 shows how the coefficient of spontaneous emission into the evanescent and radiation modes changes as a function of the interatomic distance for a fixed distance from the dielectric surface  $x_A = x_B = 200$  nm and fixed orientation of the dipole moments. The most noticeable feature is that the coupling between the two atoms due to the dielectric surface is oscillatory in nature and that it can be controlled by changing the inter atomic separation and the relative dipole moment orientation of the two atoms. This indicates that the cooperative behavior of the two atoms is strongly influenced by the presence of the dielectric surface and can lead to both, strong and weak couplings. This is also clear from Eqs. (2.19) and (2.25).

It is worth noting that the total spontaneous emission coefficient into the evanescent and radiation mode is defined as  $\gamma = \gamma^{(AA)} + \gamma^{(BB)} \pm \gamma^{(AB)}$ . The plots in Figs. 2.3 and 2.4 show the cooperative spontaneous emission coefficients of two atoms into the evanescent or radiation mode,  $\gamma_{\text{evan}}^{(AB)}$  or  $\gamma_{\text{rad}}^{(AB)}$  and these values can henceforth be used to calculate the total spontaneous emission coefficient  $\gamma$ .

## 2.4 Asymmetry of collective spontaneous emission

In this section I present the results from studying the asymmetry of the collective spontaneous emission into the evanescent and radiation modes with respect to the change of the propagation direction at the interface between the dielectric surface and vacuum. The projection of the vacuum wave-vector onto the interface between vacuum and dielectric medium  $\mathbf{K} = (0, K_y, K_z)$  determines the propagation direction of the emitted or absorbed light mode. The mirror transformation of  $\mathbf{K}$  in the  $y - z$  plane,  $\mathbf{K} \rightarrow -\mathbf{K}$ , changes the angle between the wave vector  $\mathbf{K}$  and the  $y$  axis as  $\phi \rightarrow \phi + \pi$  and can be used to determine the chirality of the propagating light.

### 2.4.1 Asymmetry of spontaneous emission into evanescent modes

To quantify the degree of asymmetry of the cooperative angular density  $F_{\text{evan}}$ , I define the factor  $\zeta_{F_{\text{evan}}}^{(ll')}$  as the ratio of the difference and sum of the angular densities with opposite in-plane wave vectors  $\mathbf{K}$  and  $-\mathbf{K}$  as

$$\zeta_{F_{\text{evan}}}^{(ll')} = \frac{\Delta F_{\text{evan}}^{(ll')}}{F_{\text{evan}}^{\text{sum}(ll')}} \quad (2.26)$$

where  $\Delta F_{\text{evan}}^{(ll')} = F_{\text{evan}}^{(ll')}(\xi, \phi) - F_{\text{evan}}^{(ll')}(\xi, \phi + \pi)$  and  $F_{\text{evan}}^{\text{sum}(ll')} \equiv F_{\text{evan}}^{(ll')}(\xi, \phi) + F_{\text{evan}}^{(ll')}(\xi, \phi + \pi)$ . These expressions can be explicitly written as

$$\begin{aligned} \Delta F_{\text{evan}}^{(ll')} &= \frac{3}{2\pi} e^{i\sqrt{1+\xi^2} \mathbf{k}_0 \cdot (\mathbf{R}_l - \mathbf{R}_{l'})} e^{-k_0 \xi (x_l + x_{l'})} T_p \left[ i\sqrt{1+\xi^2} \left( (u_{xl} u_{y l'}^* - u_{yl} u_{x l'}^*) \cos \phi \right. \right. \\ &\quad \left. \left. + (u_{xl} u_{z l'}^* - u_{zl} u_{x l'}^*) \sin \phi \right) \right] \end{aligned} \quad (2.27)$$

$$\begin{aligned} F_{\text{evan}}^{\text{sum}(ll')} &= \frac{3}{2\pi \xi} e^{i\sqrt{1+\xi^2} \mathbf{k}_0 \cdot (\mathbf{R}_l - \mathbf{R}_{l'})} e^{-k_0 \xi (x_l + x_{l'})} \left[ u_{xl} u_{x l'}^* T_p (1 + \xi^2) + u_{yl} u_{y l'}^* (T_s \sin^2 \phi \right. \\ &\quad \left. + T_p \xi^2 \cos^2 \phi) + u_{zl} u_{z l'}^* (T_s \cos^2 \phi + T_p \xi^2 \sin^2 \phi) \right. \\ &\quad \left. + (u_{yl} u_{z l'}^* + u_{zl} u_{y l'}^*) (T_p \xi^2 - T_s) \sin \phi \cos \phi \right], \end{aligned} \quad (2.28)$$

and one can immediately see that the asymmetry degree for the angular density  $\zeta_{F_{\text{evan}}}^{(ll')}$  into the evanescent modes does not depend either on the distance of the atoms from the dielectric surface nor the distance between them.

Another point worth noting is that the asymmetry in the angular density into the evanescent mode is solely due to the angular density of the  $p$  polarization. This can be

seen from Eq. (2.17) where  $F_{\text{evan},s}^{(l')}$  contains terms with the coefficients  $\sin^2 \phi$ ,  $\cos^2 \phi$ , and  $\sin 2\phi$  and the transformation  $\phi \rightarrow \phi + \pi$  has no effect on the overall expression. Hence the angular density for the  $s$  polarized evanescent modes remains the same irrespective of the sign of the in-plane wave vectors  $\mathbf{K}$  or  $-\mathbf{K}$ . On the other hand, one can see from Eq. (2.17) that the expression of  $F_{\text{evan},p}^{(l')}$  contains terms with coefficients of the form  $\sin \phi$  and  $\cos \phi$ , which change their signs under  $\phi \rightarrow \phi + \pi$ . This suggests that the angular density for the  $p$ -polarized evanescent modes takes different values for opposite in-plane wave vectors. The reason behind this asymmetry in the spontaneous emission lies in the non zero values of either the  $(u_{x_l} u_{y_{l'}}^* - u_{y_l} u_{x_{l'}}^*)$  or the  $(u_{x_l} u_{z_{l'}}^* - u_{z_l} u_{x_{l'}}^*)$  terms. These terms are non zero only if the atomic dipole vector  $\mathbf{u}$  is complex with a nonzero projection onto the  $x$  axis, which is the case we are considering. For the case when the atomic dipole vector  $\mathbf{u}$  is a real quantity, the cooperative angular density for the evanescent modes  $F_{\text{evan}}$  and subsequently the cooperative spontaneous emission into the evanescent mode is symmetric with respect to central inversion in the interface plane.

In the following, I give the expressions for the coefficients of cooperative spontaneous emission into the evanescent mode. Keeping in mind that the atoms are located in the  $x - y$  plane and these expressions are obtained for positive and negative direction in the  $x$  axis. The coefficient of cooperative spontaneous emission into the evanescent modes propagating into the  $+z$  and  $-z$  half-planes are then given by

$$\gamma_{\text{evan}}^{(l',+)} = \gamma_0^{(l')} \int_0^{\sqrt{n_1^2-1}} \xi d\xi \int_0^\pi F_{\text{evan}}^{(l')}(\xi, \phi) d\phi, \quad (2.29)$$

$$\gamma_{\text{evan}}^{(l',-)} = \gamma_0^{(l')} \int_0^{\sqrt{n_1^2-1}} \xi d\xi \int_\pi^{2\pi} F_{\text{evan}}^{(l')}(\xi, \phi) d\phi. \quad (2.30)$$

From this we can define  $\gamma_{\text{evan}}^{(l')} = \gamma_{\text{evan}}^{(l',+)} + \gamma_{\text{evan}}^{(l',-)}$  and  $\Delta_{\text{evan}}^{(l')} = \gamma_{\text{evan}}^{(l',+)} - \gamma_{\text{evan}}^{(l',-)}$  as the sum and difference between the coefficient of spontaneous emission for the opposite sides. Explicitly  $\gamma_{\text{evan}}^{(l')}$  is given by Eq. (2.19) and  $\Delta_{\text{evan}}^{(l')}$  can be calculated as

$$\begin{aligned} \Delta_{\text{evan}}^{(l')} &= \frac{3}{\pi} \gamma_0^{(l')} \int_0^{\sqrt{n_1^2-1}} e^{i\sqrt{1+\xi^2} \mathbf{k}_0 \cdot (\mathbf{R}_l - \mathbf{R}_{l'})} e^{-k_0 \xi (x_l + x_{l'})} \\ &\quad \times T_p \xi \sqrt{1 + \xi^2} \text{Im}(u_{x_{l'}}^* u_{z_l} - u_{x_l} u_{z_{l'}}^*) d\xi. \end{aligned} \quad (2.31)$$

Again one can see that the rate difference  $\Delta_{\text{evan}}^{(l')}$  is dependent on the term  $(u_{x_{l'}}^* u_{z_l} - u_{x_l} u_{z_{l'}}^*)$ , which is only non-zero for the complex atomic dipole vectors. The sign of the rate difference also depends only on the sign of the term  $(u_{x_{l'}}^* u_{z_l} - u_{x_l} u_{z_{l'}}^*)$  and not on the distance between the two atoms nor on their respective distance from the dielectric surface. We can characterize the asymmetry between these coefficients by defining  $\zeta_{\text{evan}}^{(l')} = \Delta_{\text{evan}}^{(l')} / \gamma_{\text{evan}}^{(l')}$  and, using Eqs. (2.19) and (2.31), one can immediately see that in contrast to the asymmetry factor  $\zeta_{F_{\text{evan}}}^{(l')}$  for the angular density, the asymmetry  $\zeta_{\text{evan}}^{(l')}$  for the cooperative spontaneous emission depends explicitly on the respective distance of the two atoms  $x_l$  and  $x_{l'}$  from the dielectric surface and the distance  $(\mathbf{R}_l - \mathbf{R}_{l'})$  between them.

### 2.4.2 Asymmetry of spontaneous emission into radiation modes

Similar to the definitions for the case of the evanescent mode, the sum and difference between the cooperative angular densities of radiation modes with opposite in-plane wave vectors  $\mathbf{K}$  and  $-\mathbf{K}$  is given by  $\Delta F_{\text{rad}}^{(l'l')} \equiv F_{\text{rad}}^{(l'l')}(\xi, \phi) + F_{\text{rad}}^{(l'l')}(\xi, \phi + \pi)$  and  $\Delta F_{\text{rad}}^{(l'l')} \equiv F_{\text{rad}}^{(l'l')}(\xi, \phi) - F_{\text{rad}}^{(l'l')}(\xi, \phi + \pi)$ . The degree of asymmetry of the cooperative angular densities of the radiation modes  $\zeta_{F_{\text{rad}}}^{(l'l')}$  is defined as

$$\zeta_{F_{\text{rad}}}^{(l'l')} = \frac{\Delta F_{\text{rad}}^{(l'l')}}{F_{\text{rad}}^{\text{sum}(l'l')}} \quad (2.32)$$

using the explicit expressions

$$\begin{aligned} \Delta F_{\text{rad}}^{(l'l')} &= \frac{3}{2\pi} \sqrt{1 - \xi^2} e^{i\sqrt{1 - \xi^2} \mathbf{k}_0 \cdot (\mathbf{R}_l - \mathbf{R}_{l'})} \left[ 2u_{x'l'}^* (u_{yl} \cos \phi + u_{zl} \sin \phi) \sin(k_0 \xi (x_l - x_{l'})) \right. \\ &\quad + \left( (u_{xl} u_{y'l'}^* - u_{yl} u_{x'l'}^*) \cos \phi + (u_{xl} u_{z'l'}^* - u_{zl} u_{x'l'}^*) \sin \phi \right) \left( \sin(k_0 \xi (x_l - x_{l'})) \right. \\ &\quad \left. \left. - r_p \sin(k_0 \xi (x_l + x_{l'})) \right) \right], \quad (2.33) \end{aligned}$$

$$\begin{aligned} F_{\text{rad}}^{\text{sum}(l'l')} &= \frac{3}{2\pi \xi} e^{i\sqrt{1 - \xi^2} \mathbf{k}_0 \cdot (\mathbf{R}_l - \mathbf{R}_{l'})} \left[ \left( u_{xl} u_{x'l'}^* (1 - \xi^2) + u_{yl} u_{y'l'}^* (\sin^2 \phi + \xi^2 \cos^2 \phi) \right. \right. \\ &\quad \left. \left. + u_{zl} u_{z'l'}^* (\cos^2 \phi + \xi^2 \sin^2 \phi) - (u_{yl} u_{z'l'}^* + u_{zl} u_{y'l'}^*) \sin \phi \cos \phi (1 - \xi^2) \right) \right. \\ &\quad \times \cos(k_0 \xi (x_l - x_{l'})) + \left( r_p u_{xl} u_{x'l'}^* (1 - \xi^2) + u_{yl} u_{y'l'}^* (r_s \sin^2 \phi - r_p \xi^2 \cos^2 \phi) \right. \\ &\quad \left. \left. + u_{zl} u_{z'l'}^* (r_s \cos^2 \phi + r_p \xi^2 \sin^2 \phi) - (u_{yl} u_{z'l'}^* + u_{zl} u_{y'l'}^*) (r_s + r_p \xi^2) \sin \phi \cos \phi \right) \right. \\ &\quad \left. \times \cos(k_0 \xi (x_l + x_{l'})) \right]. \quad (2.34) \end{aligned}$$

It can be seen that for the radiation modes the asymmetry of the cooperative angular density depends not only on  $\xi$  and  $\phi$ , but also on the position of the atoms with respect to the surface and to each other.

Similar to the case of the evanescent modes, the asymmetry in the cooperative angular density into the radiation mode is also mainly due to the cooperative angular density of the radiation mode for the  $p$  polarization. This is because  $F_{\text{rad},s}^{(l'l')}$  (see Eq. (2.24)) is symmetric with respect to a change of the in-plane component of the wave vector from  $\mathbf{K}$  to  $-\mathbf{K}$  as it again contains only terms with the coefficients  $\sin^2 \phi$ ,  $\cos^2 \phi$ , and  $\sin 2\phi$ . However, using Eq. (2.24), it can be seen that there are terms with coefficients  $\sin \phi$  and  $\cos \phi$  in the expression of  $F_{\text{rad},p}^{(l'l')}$  that change their sign with the transformation  $\phi \rightarrow \phi + \pi$ . This suggests that the angular density for the  $p$  polarized radiation modes takes distinct values for opposite in-plane wave vectors, which leads to the asymmetry. However, when the atomic dipole vector  $u$  is a real quantity, the cooperative angular density for the radiation modes  $F_{\text{rad}}^{(l'l')}$  and subsequently the cooperative spontaneous emission into the radiation mode remain symmetric with respect to central inversion in the interface plane.

The sign of the asymmetry factor  $\zeta_{F_{\text{rad}}}^{(l')}$  depends on a number of terms and variables, which in particular include the position  $x_l$  and  $x_{l'}$  of the two atoms, the cross product of the unit atomic dipole moment vectors ( $u_{il}u_{jl}^*$  with  $i, j = \{x, y, z\}$ ), the out-of-plane component of the wave vector  $\xi$ , the angle  $\phi$  and the reflection coefficients of the  $s$  and  $p$  polarization modes,  $r_s$  and  $r_p$ .

The calculation of the asymmetry in the cooperative angular density now leads to the asymmetry in the coefficient of cooperative spontaneous emission into the radiation modes travelling in the  $+z$  and  $-z$  sides, with the individual coefficients given by

$$\gamma_{\text{rad}}^{(l',+)} = \gamma_0^{(l')} \int_0^1 \xi d\xi \int_0^\pi F_{\text{rad}}^{(l')}(\xi, \phi) d\phi, \quad (2.35)$$

$$\gamma_{\text{rad}}^{(l',-)} = \gamma_0^{(l')} \int_0^1 \xi d\xi \int_\pi^{2\pi} F_{\text{rad}}^{(l')}(\xi, \phi) d\phi. \quad (2.36)$$

Their summation and difference are defined as  $\gamma_{\text{rad}}^{(l')} = \gamma_{\text{rad}}^{(l',+)} + \gamma_{\text{rad}}^{(l',-)}$  and  $\Delta_{\text{rad}}^{(l')} = \gamma_{\text{rad}}^{(l',+)} - \gamma_{\text{rad}}^{(l',-)}$ , with  $\gamma_{\text{rad}}^{(l')}$  given by Eq. (2.25) and  $\Delta_{\text{rad}}^{(l')}$  by

$$\begin{aligned} \Delta_{\text{rad}}^{(l')} = & \frac{3}{\pi} \gamma_0^{(l')} \int_0^1 d\xi \xi \sqrt{1 - \xi^2} e^{i\sqrt{1 - \xi^2} \mathbf{k}_0 \cdot (\mathbf{R}_l - \mathbf{R}_{l'})} \left[ (u_{x'l'}^* u_{zl} + u_{xl} u_{z'l'}^*) \sin(k_0 \xi (x_l - x_{l'})) \right. \\ & \left. + r_p (u_{x'l'}^* u_{zl} - u_{xl} u_{z'l'}^*) \sin(k_0 \xi (x_l + x_{l'})) \right]. \end{aligned} \quad (2.37)$$

Again, it can be seen that  $\Delta_{\text{rad}}^{(l')}$  depends on  $(u_{x'l'}^* u_{zl} + u_{xl} u_{z'l'}^*)$  and  $(u_{x'l'}^* u_{zl} - u_{xl} u_{z'l'}^*)$ , similar to the case of the rate difference  $\Delta_{\text{evan}}^{(l')}$ .  $\Delta_{\text{rad}}^{(l')}$  is non zero for the complex atomic dipole vector and zero for real valued electric dipole moments. However unlike the case of evanescent modes, the sign of the rate difference now depends not only on the sign of the term  $(u_{x'l'}^* u_{zl} - u_{xl} u_{z'l'}^*)$  but also on the respective distance of the two atoms from the dielectric surface. This dependence carries through to the asymmetry parameter  $\zeta_{\text{rad}}^{(l')} = \Delta_{\text{rad}}^{(l')}/\gamma_{\text{rad}}^{(l')}$ .

As the explicit expression is derived for the asymmetry between the rates  $\gamma^{(l',+)}$  and  $\gamma^{(l',-)}$  of the chiral spontaneous emission into both, the evanescent and radiation modes, the total asymmetry can be defined as  $\zeta = \Delta/\gamma$ . From all the above it is obvious that one gets  $\zeta = 0$  for the case of a real dipole polarization vector, as it is found that  $\Delta = 0$  in all expressions in this case.

To quantitatively understand the asymmetry of spontaneous emission, the respective quantities  $\zeta_{\text{evan}}$ ,  $\zeta_{\text{rad}}$  and  $\zeta$  are plotted as a function of the distance of the atoms from the dielectric interface for different values of the inter-atomic distance  $|z_A - z_B|$  in Fig. 2.5. The first case shown in panel (a) corresponds to the situation where both atoms are on top of each other and reproduces the result for single atom case [8]. Panels (b)-(d) shows the asymmetry parameters for increasing inter-atomic distances and for all four cases one can see that the asymmetry parameter  $\zeta_{\text{evan}}$  for emission into evanescent modes is positive and decreases with increasing atom-interface distance. It can be seen that the asymmetry parameters  $\zeta_{\text{rad}}$  and  $\zeta$  start becoming oscillatory at shorter atom-interface distance for increasing distance between the atoms as compared to the single atom case, Fig. 2.5(a).

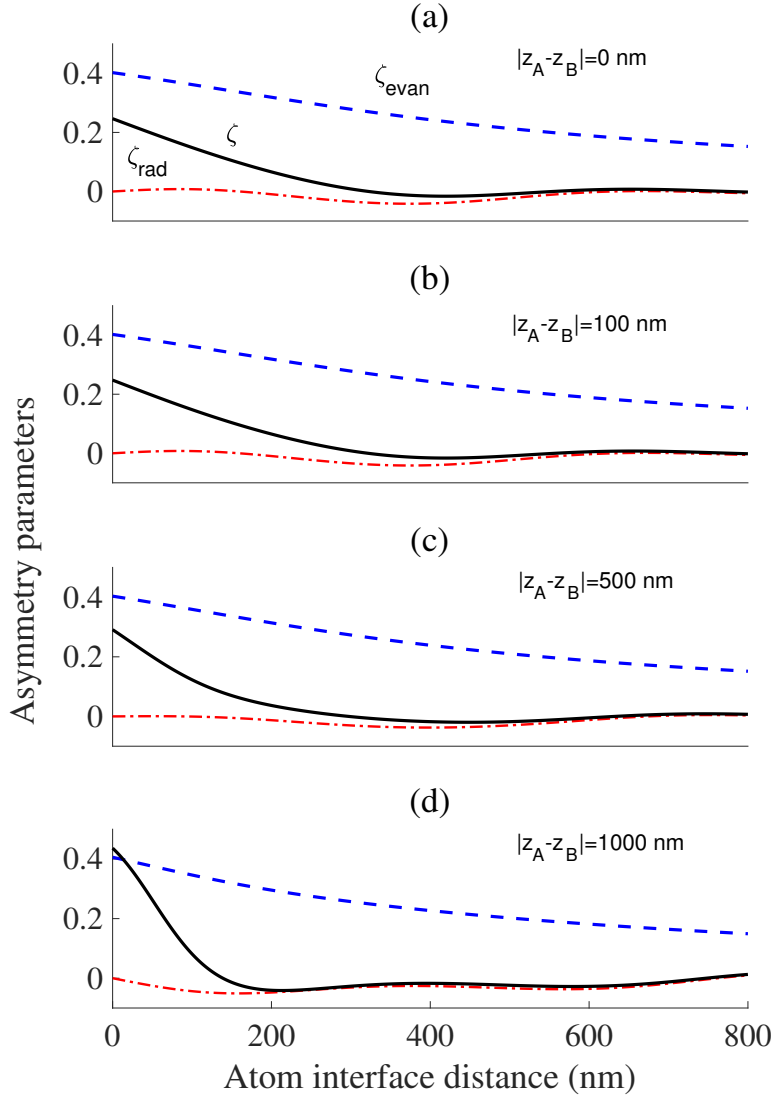


**Figure 2.5:** Asymmetry parameters for cooperative spontaneous emission into the evanescent modes  $\zeta_{\text{evan}}$  (blue dashed line), radiation modes  $\zeta_{\text{rad}}$  (red dash-dotted line), and both type of modes  $\zeta$  (black solid line) as a function of atom-interface distance  $x_A = x_B = 0 - 800$  nm for different values of inter-atomic distance (a)  $|z_A - z_B| = 0$  nm, (b)  $|z_A - z_B| = 100$  nm, (c)  $|z_A - z_B| = 500$  nm, and (d)  $|z_A - z_B| = 1000$  nm. The atomic dipole moment matrix elements for both atoms are taken as complex quantities  $\mathbf{u}_A = \mathbf{u}_B = \frac{1}{\sqrt{2}}(\hat{x} + i\hat{z})$ .

## 2.5 Conclusions

In this section, the mode function method was used to calculate the cooperative spontaneous emission of two atoms with arbitrarily polarized electric dipole moments placed in front of a flat dielectric surface. I have considered the general case where the atomic dipoles can rotate in time and space or, in other words, when the atomic dipole matrix

elements are complex vectors. I have used the mode expansion technique to calculate the angular density and hence the spontaneous emission coefficients into the evanescent and radiation modes analytically and derived their dependence on the orientation direction of the electric dipole moments, position of the two atoms and the distance between the two atoms.

This work has shown that the relative position of the atoms and the orientations of the electric dipole moments with respect to the dielectric surface have a strong effect on the cooperative spontaneous emission coefficient into the evanescent and radiation modes. For the spontaneous emission coefficient into the radiation mode oscillatory behavior was found, which reduces in amplitude as the atom-interface distance is increased. This is a reliable indicator that the presence of the dielectric medium acts like a communication channel, and modifies the coupling between the two atoms. I have therefore shown that it is possible to determine the conditions for maximum coupling between the atoms as a function of the orientation of the electric dipole moments, the distance between the atoms and the atom interface distance.

Finally, to quantify the chirality, I have calculated the asymmetry degree for the angular density and the spontaneous emission into the evanescent modes, the radiation modes and the sum of them. Here the mirror symmetry of the in-plane projection of the wave-vector at the interface was used to mathematically quantify the symmetry of the propagated beam in the dielectric.

Even though the results are very interesting and insightful to give a clear understanding of how two atoms communicate through a dielectric channel, the mode function approach does not offer an easy way to calculate changes of decay related due to the frequency shift of atoms. To incorporate this effect, the Green's function method needs to be employed, which is a future task to be carried out for this project.



# Chapter 3

## "Channeling of spontaneous emission from a multi-level atom into a nanofiber" originally published as [1]

### 3.1 introduction

Similar to the presence of a flat dielectric surface, which was discussed in the previous chapter, the presence of an optical nanofiber can effect the spontaneous emission rates of an atom and act as a communication channel. This leads to a different behaviour for the atomic decay when compared to free space. In this Chapter, I present my work on the channeling of spontaneous emission into a nanofiber which can support higher-order modes in addition to the fundamental one and, as an introduction, I briefly review how to use the mode function method for the case of a multi-level atom that can couple to the fundamental and higher-order modes. The results of this work were published as *Phys. Rev. A* **96**, 043859 (2017).

As seen in Chapter 2, the spontaneous emission rate of two-level atoms in the vicinity of a flat dielectric surface is affected by the presence of the medium, as it modifies the modes the atoms can decay into. This suggests that different geometries of the dielectric substrate will have a direct effect on these results. Here, I consider an ultra-thin optical nanofiber with a cylindrical symmetry as my medium, which is an interesting system to study and which has in the recent decade been used in hybrid systems together with atoms [6, 44, 45, 78, 82, 87, 88, 129]. To make the situation more realistic, I will assume that the atom that couples to the fiber is a Rubidium atom with a multi-level structure. By using the mode function method, I can then calculate the spontaneous emission rate of the atom into the fundamental and higher-order modes of the optical fiber. This rate depends on various quantities, such as the magnetic sub-level occupied, the type of optical modes present, the orientation of the quantization axis, the position of the atom relative to the fiber, and the fiber radius.

Furthermore, in the vicinity of dielectric substances neutral atoms experience changes in their properties, such as frequency shifts of the atomic transitions and changes in the spontaneous decay rate [8]. As seen in the previous chapter, for more than one atom, the dielectric medium can also modify the coupling between the atoms, and it

is interesting to determine how this can lead to an enhanced coupling strength if the medium is an optical nanofiber.

As discussed in chapter 1, the optical modes of a fiber depend on various quantities such as the shape of propagating beam and the diameter of the nanofiber. Different modes can have different shapes and symmetries, which in turn can effect different quantities of the hybrid systems. Due to the small radius of the optical nanofiber, single modes of light can be transmitted through the fiber in limited frequencies. For example, due to the symmetry inherent in the TE modes with respect to the axis of fiber, the spontaneous emission rate into the TE modes will always have to be symmetric with respect to the propagation directions. However, directional asymmetry of spontaneous emission may appear into other modes when the quantization axis does not lie in the meridional plane containing the position of the atom.

## 3.2 Mathematical model of a multi-level atom in the vicinity of an optical nanofiber

In free space, the direction of spontaneous emission of an atom is distributed isotropically, however the presence of a dielectric substrate modifies this properly by favouring (or preventing) emission into the modes of the substrate (or free space). An example of this phenomena is the channeling of spontaneous emission of an atom into the optical modes of an ultra-thin optical nanofiber. For atoms that require to consider their multi-level structure, such as the experimentally popular rubidium or cesium atoms often do, the coupling to the different modes also depends on the magnetic sub-levels and the orientation of the electric dipole moment of the atom. To study this system, I consider a  $^{87}\text{Rb}$  (multi-level alkali-metal) atom that is trapped in the vicinity of an optical nanofiber, which has a radius  $a$  and a refractive index of  $n_1 = 1.4537$  and which supports the fundamental and several higher-order modes (see Fig. 3.1(a)).

For atoms with a hyperfine-structure, the states can be labeled with their total electronic angular momenta  $J$  and  $J'$ ; their total atomic angular momenta  $F$  and  $F'$ ; and their magnetic quantum numbers  $M$  and  $M'$ . Thus, each state can be defined by  $|g\rangle = |JFM\rangle$  for a ground state and  $|e\rangle = |J'F'M'\rangle$  for an excited state. The hyperfine-structure (hfs) for the  $5S_{1/2}$  (ground) and  $5P_{3/2}$  (excited) states in  $^{87}\text{Rb}$  and the possible transitions are shown in Fig. 3.1(b). The electric dipole matrix element for such an atom can then be written as [130]

$$d_{qQ} = (-1)^{I+J'-M'} \langle J' \| D \| J \rangle \sqrt{(2F+1)(2F'+1)} \times \begin{Bmatrix} J' & F' & I \\ F & J & 1 \end{Bmatrix} \begin{pmatrix} F & 1 & F' \\ M & q & -M' \end{pmatrix}. \quad (3.1)$$

The evanescent field that the atom interacts with can be written as a combination of positive and negative-frequency components,  $\mathbf{E} = \mathbf{E}^{(+)} + \mathbf{E}^{(-)}$ , where both parts consist of guided and radiation modes,  $\mathbf{E}^{(\pm)} = \mathbf{E}_g^{(\pm)} + \mathbf{E}_r^{(\pm)}$ . The guided and radiation modes of an optical nanofiber in cylindrical coordinates were introduced in Chapter 1 and for

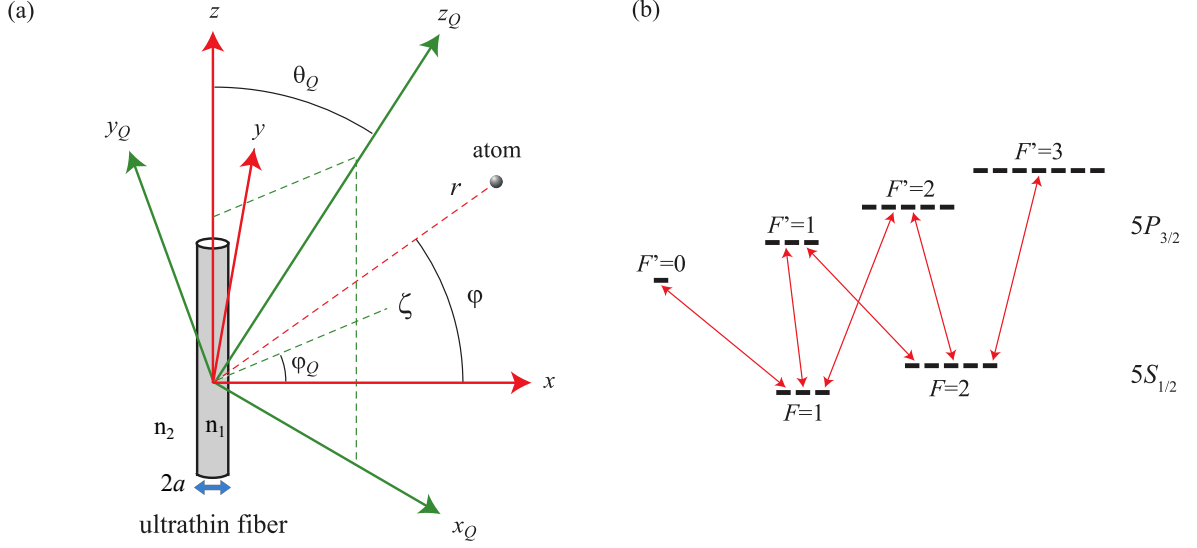


**Figure 3.1:** (a) Schematic plot of the atom in the vicinity of an optical nanofiber. The atom interacts with the guided and radiation modes via its electric dipole moment. The fiber-based Cartesian coordinate system  $\{x, y, z\}$  and also the corresponding cylindrical coordinate system  $\{r, \varphi, z\}$ , where  $r$  and  $\varphi$  are the polar coordinates in the transverse  $x - y$  plane of the fiber, are indicated. The energy levels of the atom are specified in a Cartesian coordinate system  $\{x_Q, y_Q, z_Q\}$ , where  $z_Q$  is the direction of the quantization axis. (b) Schematic of the hyperfine-structure of the atomic levels of the  $5P_{3/2}$  and  $5S_{1/2}$  states of the  $^{87}\text{Rb}$  atom and the allowed transitions. These levels are specified with respect to the quantization axis  $z_Q$  [1]. The fiber has radius of  $a$  and refractive index of  $n_1$ .

the positive part can be written as

$$\mathbf{E}_g^{(+)} = i \sum_{\mu} \sqrt{\frac{\hbar\omega\beta'}{4\pi\epsilon_0}} a_{\mu} \mathbf{e}^{(\mu)} e^{-i(\omega t - f\beta z - pl\varphi)}, \quad (3.2)$$

$$\mathbf{E}_r^{(+)} = i \sum_{\nu} \sqrt{\frac{\hbar\omega}{4\pi\epsilon_0}} a_{\nu} \mathbf{e}^{(\nu)} e^{-i(\omega t - \beta z - l\varphi)}. \quad (3.3)$$

where  $\mathbf{e}^{\mu(\nu)} = \mathbf{e}^{\mu(\nu)}(r, \phi)$  are the profile functions of the guided (radiation) modes,  $a_{\mu}$  annihilates a  $\mu$  mode and  $\beta$  is the the longitudinal propagation constant. The frequency is  $\omega$ , the propagation direction is  $f$  and the polarization is  $p$ .

To calculate the spontaneous emission rate, one has to start from the Hamiltonian of the system where the atom-light interaction is described by  $H = -\mathbf{d} \cdot \mathbf{E}$ , where  $\mathbf{d}$  is electric dipole moment of atom and  $\mathbf{E}$  is the electric field of the light. In the interaction picture, the light-matter interaction part of the Hamiltonian is

$$H_{\text{int}} = -i\hbar \sum_{\alpha eg} G_{\alpha eg} \sigma_{ge}^{\dagger} a_{\alpha} e^{-i(\omega - \omega_{eg})t} + \text{H.c.}, \quad (3.4)$$

where the coefficients are defined by [1]

$$G_{\mu eg} = \sqrt{\frac{\omega\beta'}{4\pi\epsilon_0\hbar}} (\mathbf{d}_{eg} \cdot \mathbf{e}^{(\mu)}) e^{i(f\beta z + pl\varphi)}, \quad (3.5)$$

$$G_{\nu eg} = \sqrt{\frac{\omega}{4\pi\epsilon_0\hbar}} (\mathbf{d}_{eg} \cdot \mathbf{e}^{(\nu)}) e^{i(\beta z + l\varphi)}. \quad (3.6)$$

By using the Hamiltonian in Eq. (3.4), one can calculate the time evolution of the reduced density operator,  $\rho$ , using the Liouville-von Neumann equation, which leads to [45]

$$\dot{\rho}_{ee'} = -\frac{1}{2} \sum_{e''} (\gamma_{ee''} \rho_{e''e'} + \gamma_{e''e'} \rho_{ee''}), \quad (3.7)$$

$$\dot{\rho}_{gg'} = \sum_{ee'} \gamma_{e'eg'g} \rho_{ee'}, \quad (3.8)$$

$$\dot{\rho}_{eg} = -\frac{1}{2} \sum_{e'} \gamma_{ee'} \rho_{e'g}, \quad (3.9)$$

where coefficients  $\gamma_{ee'gg'}^{(g)}$ ,  $\gamma_{ee'}^{(g)}$  and  $\gamma_{ee'gg'}^{(r)}$ ,  $\gamma_{ee'}^{(r)}$  describe spontaneous emission into guided modes, and into radiation modes [1].

The coefficients for the spontaneous emission rate of the atom can then be obtained from those equations, with all input fully defined by the coefficients in Eqs. (3.5) and (3.6).

### 3.3 Spontaneous emission of the atom

The spontaneous emission rates of a multilevel atom into the different modes can be calculated from the time evolution of the reduced density operator of the atom [45]. The elements of this operator can be written as [1]

$$\begin{aligned} \gamma_{ee'gg'} &= \gamma_{ee'gg'}^{(g)} + \gamma_{ee'gg'}^{(r)}, \\ \gamma_{ee'} &= \sum_g \gamma_{ee'gg} = \gamma_{ee'}^{(g)} + \gamma_{ee'}^{(r)}, \end{aligned} \quad (3.10)$$

where  $\gamma_{ee'gg'}^{(g)}$  and  $\gamma_{ee'}^{(g)}$  describe spontaneous emission into guided modes, and the set of coefficients  $\gamma_{ee'gg'}^{(r)}$  and  $\gamma_{ee'}^{(r)}$  describes spontaneous emission into radiation modes [1]. The rates of spontaneous emission for different magnetic sub-levels into different modes as a function of the various quantities of the system are presented in the publication *Phys. Rev. A* **96**, 043859 (2017) included below [1]. The formalism we use allows the atom to be inside or outside of the fiber. It also allows the atom to have, in principle, an arbitrary level structure. The results, when reduced to the case of a two-level atom inside or outside a fiber, are in perfect agreement with other studies [122, 131]. In particular, the agreement with the results of Ref. [122] has been confirmed analytically and numerically, while the agreement with the results of Ref. [131] has been checked

numerically. For a multilevel atom in free space, the results are also in agreement with previous results [132].

### 3.4 Publication

F. Le Kien, S. Sahar S. Hejazi, Th. Busch, V. G. Truong, and S. Nic Chormaic. Channeling of spontaneous emission from a multi-level atom into a nano-fiber, *Phys. Rev. A* **96**, 043859 (2017).

### 3.5 Summary and conclusions

In this work, I have focused on how to characterise the spontaneous emission of a multi-level atom into the fundamental and higher-order modes of an ultra-thin optical fiber. In this situation the spontaneous emission rate depends on various elements of the system such as the position of the atom, the magnetic sublevel structure, the orientation of the quantization axis, the type of modes available and the fiber radius.

I found that the rate of spontaneous emission into the TE modes is always symmetric with respect to the propagation directions. Furthermore, when the quantization axis lies in the meridional plane containing the position of the atom, the rates of spontaneous emission into other guided modes do also not depend on the propagation direction. However, asymmetric spontaneous emission with respect to the propagation directions may appear when the output modes are not TE modes and the quantization axis does not lie in the meridional plane containing the position of the atom.

It is interesting to note that the rate of spontaneous emission into guided modes propagating in a given direction does not change when both, the propagation direction and the magnetic quantum number are reversed. This means that asymmetry of spontaneous emission with respect to the propagation directions leads to asymmetry with respect to the magnetic quantum numbers and vice versa. As shown in the publication, when the quantization axis coincides with the fiber axis and the radial distance is not too large, the rates of spontaneous emission from the outermost magnetic sublevels into guided modes are larger than those from the other sublevels.

In summary, the spontaneous emission rate from an atom into the fiber surface mode depends on the form of the optical mode, the magnetic sublevels and the radius of nanofiber, as shown in more detail in the paper. In particular, the spontaneous emission into the HE<sub>21</sub> modes is stronger than into the HE<sub>11</sub>, TE<sub>01</sub>, and TM<sub>01</sub> modes for a fiber radius in the range of 330 to 450 nm. As shown in Fig. (11) in the publication, the total fractional rates  $\eta_e = \gamma_e^{(g)}/\gamma_e$  of emission into guided modes is most substantial when the fiber radius is around 180 nm (see sub-figure (a)), where the fiber supports only the fundamental HE<sub>11</sub> modes, or around 340 nm, where the fiber supports not only the HE<sub>11</sub> modes but also the TE<sub>01</sub>, TM<sub>01</sub>, and HE<sub>21</sub> modes (see sub-figure (d)). At the cutoff for higher-order modes, the rates of spontaneous emission into guided and radiation modes undergo steep variations, which are caused by the changes of the mode structure. Due to the mutual compensation of these changes, the variations of the total rate of spontaneous emission into both types of modes are smooth.

Also, the spontaneous emission from the upper level of the cyclic transition into the TM modes is unidirectional when the quantization axis lies at an appropriate azimuthal angle in the fiber transverse plane. The fractional rates depend on the atomic transition wavelength and the quantum numbers of the atomic states. While these results depend on the type of the atom considered, the differences for other species are not dramatic. For example, the average fractional rates do not depend on any specific characteristics of the atomic states except for the atomic transition frequency.

This work has provided a starting point to explore and study more complicated and realistic quantum hybrid systems. For instance, employing this groundwork to expand it to quadrupole interactions between the atoms and the evanescent field is interesting, especially since alkali atoms can have substantial electric quadrupole moments in addition to their dipole ones. This is considered in Ref. [133], where the authors carefully studied a light-matter hybrid system based on quadrupole coupling to the modes of an ultra-thin optical fiber. Our study can also be extended to aid the understanding of the principles that can control light emission and guide designing quantum systems which act as chiral quantum optical emitters [134]. As discussed in more detail in the paper, our system is very sensitive to the symmetry of the input beam and the structure of the hyperfine states of the atom. It can therefore also be used to study anisotropic coupling of quantum emitters via the modes of optical fibers [135] and the induced torques and forces on multi-level atoms from the guided light [2, 3].

# Chapter 4

## "Chiral force of guided light on an atom" originally published as [2, 3]

### 4.1 Introduction

The purpose of this chapter is to motivate the study of chiral forces of light on an individual atom in the vicinity of an ultra-thin optical nanofiber and to briefly summarise the employed mathematical treatments. Previously, it was shown how the presence of a dielectric medium effects various features of an atomic systems, such as the spontaneous decay rate, as the orientation of the electric dipole moment of the atom and also the type of the optical modes of fiber have substantial influence on the value and the direction of the spontaneous emission. Since in some situations the spontaneous emission has a directional dependence (i.e. becomes chiral), a natural question to ask is about the chiral nature of the the recoil force. These investigations into the details of optical chiral forces on atoms have been summarised in two peer-reviewed publications that are included below: Phys. Rev. A **97**, 063849 (2018) and New J. Phys. **20**, 093031 (2018).

In Ref. [Phys. Rev. A **97**, 063849 (2018)] the mode function method was used to express the various modes of the fiber, which allowed us to calculate the force in the direction of the fiber axis and showed the possibility of chiral forces. However, to have a full picture one needs to calculate the total force, which has contributions from the driving-field force, the spontaneous-emission recoil force, and the fiber-induced van der Waals potential force. For the latter, a number of studies on van der Waals interactions between atoms (considered to be point-like polarizable particles) and dielectric cylinders exist [136–143]. The best way to calculate the total force is through the Green's function method, which was done in the second publication [New J. Phys. **20**, 093031 (2018)]. Both works demonstrate that the directional dependencies of the Rabi frequency and the spontaneous emission rate lead to a significant chirality of the optical force on an atom. Over the last few decades, electromagnetic fields have been widely employed for controlling and manipulating microscopic quantum systems and, in particular, optical setups have been used to cool and trap atoms [144–147]. The interaction between light and matter leads to different optical forces that are felt by the atoms and using these for cooling to temperature close to absolute zero is common-

place in many laboratories worldwide. When interacting with laser light the atoms can absorb photons and become excited, before re-emitting the photon through spontaneous emission and returning to the atomic ground state. Since spontaneous emission in free space is a random and isotropic process, the recoil force is randomly oriented and repeated absorption and emission processes impart on average zero recoil onto the atom. This is a crucial part of standard laser cooling techniques. Thence, in free space the optical forces on atoms are determined by the absorption and emission of single photons and by the light shifts of the ground and excited states. However this changes in the presence of modes stemming from a dielectric medium and in particular leads to forces that are no longer isotropic.

As explained earlier in this thesis, the presence of a dielectric medium can break the isotropic symmetry of free space for certain quantities and, in particular, lead to chirality for the spontaneous emission processes [148]. The appearance of an asymmetric emission pattern for an atom next to media of different geometry has been investigated, for example for a flat surface [8, 51, 149], an optical nanofiber [47–51, 150], or a photonic topological material [151, 152]. When the spontaneous emission rate becomes asymmetric with respect to the propagation directions [47–49], the atom also experiences a directional recoil force and, for instance, for an atom with a rotating dipole located near a nanofiber a resonant lateral Casimir-Polder force has been predicted [50].

Full control over a chiral force could potentially have significant applications in various areas of physics. For instant, they could provide control over the center-of-mass motion of atoms beyond the recoil limit and therefore help to reach lower temperatures in laser cooling. They could also be used to sort atoms in optical lattices [153, 154] or to construct atomic interferometers. For the latter one can take advantage of the fact that superpositions of different internal states would transfer to superpositions of the atomic center-of-mass.

In the following, I will briefly review how to incorporate the effect of a dielectric medium onto the atom by using the mode function and the Green's function method and show how one can calculate the force of a near-resonant guided light field of an ultra-thin optical fiber on a two-level atom.

## 4.2 Model, Hamiltonian and optical force of light on an atom

Let us again consider a two-level alkali atom with ground state  $|g\rangle$  and excited state  $|e\rangle$  with the energy difference of  $\hbar\omega_0$ , which is located in the vicinity of an ultra-thin optical nanofiber with radius  $a$  and refractive index  $n_1 > 1$  in free space with refractive index  $n_2 = 1$ . The atom possesses an electric dipole moment  $\mathbf{d}$ , which can have complex matrix elements. The interaction between the atom and the field can be expressed with the Hamiltonian of the standard form  $H_{\text{int}} = -\mathbf{d} \cdot \mathbf{E}$ , where  $\mathbf{E}$  is the classical electric field. As explained in previous chapters, the field  $\mathbf{E}$  can be written as a summation of the positive and the negative frequencies of the guided and radiation modes. I will also assume that the fiber supports the fundamental and higher order modes.



Within the semi-classical treatment, the center-of-mass motion of the atom experiences forces arising from changes of the internal state of the atom. These forces can be calculated from the interaction Hamiltonian as [144]

$$\mathbf{F} = -\langle \nabla H_{\text{int}} \rangle, \quad (4.1)$$

where  $H_{\text{int}}$  is the interaction part of Hamiltonian in the interaction picture. As mentioned in Chapter 1, there are two elegant ways to define a field and calculate the Hamiltonian and other important quantities of atom-field interactions. In the work presented in this chapter, both methods are employed and a comparison between the quantities is presented in [New J. Phys. **20**, 093031 (2018)]. As expected, both methods lead to consistent results.

In the mode function method, the electric field of the laser beam is defined based on the modes of the fiber, which carry all the information about the electromagnetic field of the laser, such as frequency  $\omega_L$ , the type of modes and the propagation direction (see Chapter 1 for more details). In the interaction picture the Hamiltonian can then be written as [Phys. Rev. A **97**, 063849 (2018)]

$$H_{\text{int}} = -\frac{\hbar}{2}\Omega\sigma_{eg}e^{-i(\omega_L-\omega_0)t} - i\hbar\sum_{\alpha}G_{\alpha}\sigma_{eg}a_{\alpha}e^{-i(\omega-\omega_0)t} - i\hbar\sum_{\alpha}\tilde{G}_{\alpha}\sigma_{ge}a_{\alpha}e^{-i(\omega+\omega_0)t} + \text{H.c.}, \quad (4.2)$$

where  $\Omega = \mathbf{d}\cdot\mathcal{E}/\hbar$  is the Rabi frequency and the notations  $\alpha = \mu, \nu$  and  $\sum_{\alpha} = \sum_{\mu} + \sum_{\nu}$  stand for the general mode index and the full mode summation, respectively. The coefficients  $G_{\alpha}$  and  $\tilde{G}_{\alpha}$  carry all the information about the electric dipole moment of the atom and the type of optical modes of the fiber, as well as the frequency and propagation direction (see Eqs. (11) and (12) in Ref. [New J. Phys. **20**, 093031 (2018)] for further details).

Within the Born-Markov approximation the force can be split into different components [144]. One part originates from the interaction between the atom and the driving field,  $\mathbf{F}_{\text{drv}}$ , and follows from the recoil of absorption and emission and the shifts of the energy levels. Another force is connected to the spontaneous emission,  $\mathbf{F}_{\text{spon}}$ , and  $\mathbf{F}_{\text{vdW}}^{(e)}$  and  $\mathbf{F}_{\text{vdW}}^{(g)}$  are forces associated with the surface-induced van der Waals potentials for the excited and ground states. This leads to [Phys. Rev. A **97**, 063849 (2018)]

$$\mathbf{F} = \mathbf{F}_{\text{drv}} + \rho_{ee}\mathbf{F}_{\text{spon}} + \rho_{ee}\mathbf{F}_{\text{vdW}}^{(e)} + \rho_{gg}\mathbf{F}_{\text{vdW}}^{(g)}, \quad (4.3)$$

with the explicit expressions of each individual force given by

$$\mathbf{F}_{\text{drv}} = \frac{\hbar}{2}(\rho_{ge} \nabla \Omega + \rho_{eg} \nabla \Omega^*), \quad (4.4)$$

$$\mathbf{F}_{\text{spon}} = i\pi\hbar \sum_{\alpha_0} (G_{\alpha_0}^* \nabla G_{\alpha_0} - G_{\alpha_0} \nabla G_{\alpha_0}^*), \quad (4.5)$$

$$\mathbf{F}_{\text{vdW}}^{(e)} = \hbar \nabla \mathcal{P} \sum_{\alpha} \frac{|G_{\alpha}|^2}{\omega - \omega_0}, \quad (4.6)$$

$$\mathbf{F}_{\text{vdW}}^{(g)} = \hbar \nabla \mathcal{P} \sum_{\alpha} \frac{|\tilde{G}_{\alpha}|^2}{\omega + \omega_0}. \quad (4.7)$$

The notation  $\rho$  stands for the density operator of the internal atomic state in the coordinate frame rotating with the frequency  $\omega_L$ , the notation  $\alpha_0 = \mu_0, \nu_0$  labels resonant guided modes  $\mu_0 = (\omega_0 N f p)$  or resonant radiation modes  $\nu_0 = (\omega_0 \beta l p)$ , the summation  $\sum_{\alpha_0}$  is  $\sum_{\alpha_0} = \sum_{\mu_0} + \sum_{\nu_0}$  with  $\sum_{\mu_0} = \sum_{N f p}$  and  $\sum_{\nu_0} = \sum_{l p} \int_{-k_0 n_2}^{k_0 n_2} d\beta$ , and the notation  $\mathcal{P}$  stands for the principal value of the integral over  $\omega$ . With this the total force can be calculated from [New J. Phys. **20**, 093031 (2018)]

$$\begin{aligned} \mathbf{F} = & \left\{ \frac{\hbar}{2} (\nabla \Omega) \langle \sigma_{eg} \rangle e^{-i(\omega_L - \omega_0)t} + i\hbar \sum_{\alpha} (\nabla G_{\alpha}) \langle \sigma_{eg} a_{\alpha} \rangle e^{-i(\omega - \omega_0)t} \right. \\ & \left. + i\hbar \sum_{\alpha} (\nabla \tilde{G}_{\alpha}) \langle \sigma_{ge} a_{\alpha} \rangle e^{-i(\omega + \omega_0)t} + \text{c.c.} \right\}. \end{aligned} \quad (4.8)$$

For the special case that the driving field is propagating along the fiber axis  $z$ , this expression can be simplified to [Phys. Rev. A **97**, 063849 (2018)]

$$F_z = \hbar \rho_{ee} \left\{ f_L \beta_L \Gamma - \sum_N \beta_0^{(N)} (\gamma_{gN}^{(+)} - \gamma_{gN}^{(-)}) - \int_{-k_0 n_2}^{k_0 n_2} \beta \gamma_r^{(\beta)} d\beta \right\}, \quad (4.9)$$

where

$$\rho_{ee} = \langle \sigma_{ee} \rangle = \frac{|\Omega|^2/4}{\Delta^2 + \Gamma^2/4 + |\Omega|^2/2}. \quad (4.10)$$

Here,  $\Delta = \omega_L - \omega_0$  is the detuning of the driving field and  $\Gamma = \gamma_g + \gamma_r$  is the total rate of spontaneous emission with  $\gamma_g = \sum_N (\gamma_{gN}^{(+)} + \gamma_{gN}^{(-)})$  and  $\gamma_r = \int_{-k_0 n_2}^{k_0 n_2} \gamma_r^{(\beta)} d\beta$  [150].

By plotting the force in the  $z$  direction, Eq. (4.9), with respect to the normalized radial distance  $r/a$  of the atoms from the fibre for various optical modes (see Fig. (2) in Ref. [Phys. Rev. A **97**, 063849 (2018)]), it is immediately evident that for certain modes the forward  $f_L = +$  and the backward force  $f_L = -$  are not equal. This chirality has its origins in Eq. (4.9) when the expression  $\gamma_{gN}^{(+)} - \gamma_{gN}^{(-)}$  is asymmetric.

To calculate the total force in all directions we will use the Green's function method, which provides an elegant way to define any electromagnetic field. For our case the Green's function of the electric field outside of the fiber ( $r > a$ ) can be obtained by substituting the vacuum Green's tensor (Eq. (1.57)), the reflection part of the Green's tensor (Eq. (1.58)) and the transmitted part of the Green's tensor (Eq. (1.59)) into the

definition of the electric field outside of the fiber given in Eq. (1.56). By calculating the various terms of the total force using the Green's function, the total radiation force given in Eq. (4.3) can be written as (see Ref. [New J. Phys. **20**, 093031 (2018)] for further details)

$$\begin{aligned} \mathbf{F} = & \mathbf{F}^{(\text{drv})} + (\rho_{ee} - \rho_{gg}) \frac{\omega_0}{\pi \epsilon_0 c^2} \int_0^\infty du \frac{u^2}{\omega_0^2 + u^2} \nabla \left\{ \mathbf{d} \cdot \text{Re}[\mathbf{G}^{(\text{R})}(\mathbf{R}, \mathbf{R}; iu)] \cdot \mathbf{d}^* \right\} \\ & + \rho_{ee} \frac{\omega_0^2}{\epsilon_0 c^2} \left\{ \nabla [\mathbf{d} \cdot \mathbf{G}^{(\text{R})}(\mathbf{R}, \mathbf{R}'; \omega_0) \cdot \mathbf{d}^*] \Big|_{\mathbf{R}'=\mathbf{R}} + \text{c.c.} \right\}. \end{aligned} \quad (4.11)$$

The first term  $\mathbf{F}^{(\text{drv})}$  is the force originating from the driving field while the second term contains an integral over the components of imaginary frequencies. The second term describes the effects of the off-resonant van der Waals potentials onto the force. The last term corresponds to the resonant excited-state van der Waals potential and the scattered-photon recoil. This expression contains all contributions to the force and can be used to describe it in all spatial directions.

Since the axial component of the guided mode is nonzero, the magnitude of the force of the guided driving field can depend on the propagation direction of the beam  $f_L$ . As shown in Ref. [New J. Phys. **20**, 093031 (2018)] for the case where the atom has a complex electric dipole moment,  $\mathbf{d} = (i\hat{x} - \hat{z})/\sqrt{2}$ , all components of the force (from Eq. (4.3)) show chiral behaviour (forward and backward forces are not equal). Different components of the force, which are plotted with respect to the normalised distance  $r/a$  and the azimuthal component  $\phi$  in Figs. 5 and 6 of the [New J. Phys. **20**, 093031 (2018)], show clearly that the driving force  $F_z^{(\text{drv})}$  has different values for  $f_L = +$  and  $f_L = -$ . In particular, the same conclusion can be obtained for the HE21 mode from Fig. 20 in [New J. Phys. **20**, 093031 (2018)], where it is shown that  $F_z$  and  $F_r$  are different for forward and backward forces.

All further details on how the chirality of the force changes with respect to various orientations of the electric dipole moment of an atom, as well as various optical modes are presented in Phys. Rev. A **97**, 063849 (2018) and New J. Phys. **20**, 093031 (2018), which are included below.

## 4.3 Publication

F. Le Kien, D. F. Kornovan, S. Sahar S. Hejazi, V. G. Truong, M. I. Petrov, S. Chormaic, and Th. Busch. Force of light on a two-level atom near an ultrathin optical fiber. *New J. Phys.* **20**, 093031 (2018), and F. Le Kien, S. Sahar S. Hejazi, V. G. Truong, S. Nic Chormaic, and Th. Busch. Chiral force of guided light on an atom. *Phys. Rev. A* **97**, 063849 (2018).

## 4.4 Summary and conclusions

In summary, in this work I have examined the force generated by a guided light field from an ultra-thin optical fiber on a two-level atom analytically and numerically using

the mode function and the Green's tensor method. Both methods were also shown to be consistent with each other. I have shown that the magnitude of the force of the guided light on an atom with a complex electric dipole moment (i.e. a dipole moment rotating in the meridional plane) depends on the direction of field propagation. Since the Rabi frequency of the guided driving field has a directional dependence, the rate of the spontaneous emission of an atom is chiral as well. This leads to the chirality of the force. The total force on the atom was found to consist of the driving-field force, the spontaneous-emission recoil force, and the fiber-induced van der Waals potential force. The axial component of the driving-field force is a light pressure force, while the radial component is a gradient force.

This chiral force could have many potential applications in quantum science and technologies, for instance to control and manipulate the direction of motion of atoms in a cold atomic gas or an optical lattice near the surface of an ultra-thin fiber by simply varying the electric field propagation direction. This could enable studies of optical binding effects on atoms experiencing chiral forces and lead in turn to new laser cooling schemes and novel designs for atom interferometers.

## 4.5 My contributions

This project was carried out in close collaboration with Dr. Fam LeKien. For the study using the mode function method I carried out the analytical calculations for the force and the comparisons between the forward and backward forces to determine the chirality of the system. Since the mode function method has limitations and does not allow one to calculate the force in all directions, I then switched to using the Green's function method. In this second part of the project I performed the analytical calculations that enabled the construction of the mathematical model as well as the detailed comparisons between the two methods. I was involved in all discussions at all stages of these two project and also in the writing of the manuscripts.

# Chapter 5

## "Symmetry breaking in binary Bose-Einstein condensates" originally published as [4]

### 5.1 Introduction

To expand the horizon of my studies and explore the behaviour of many body atomic systems in the presence of an evanescent field, I now shift gears and investigate the effect of an evanescent field on a collection of ultra-cold atoms in a Bose-Einstein condensate (BEC) state. Cold gases of neutral atoms have proven to be highly controllable systems to study new physics and simulate other quantum systems in recent years [155–157]. Their center of mass state and internal states can be controlled by using laser light, and even the interaction between the individual particles can be tuned by using external fields [158, 159]. In particular, Bose-Einstein condensates are superfluid and therefore outstanding systems to study quantized rotation and topological excitations such as quantum vortices.

Persistent currents and vortices are two of the hallmarks of superfluidity and they have been studied extensively in atomic Bose-Einstein condensates. Vortices are fundamental objects that possess a  $2\pi$  phase winding around a singularity, which is countered at which the density vanishes. The inducing angular momentum into a simply connected BEC by rotating it leads to a homogeneous distribution of vortices over the whole condensate [160, 161]. Therefore the vortex structure is distributed homogeneously over the condensate as well. These vortices with winding number one arrange themselves in an Abrikosov lattice type structure [162]. However, inhomogeneous artificial gauge fields can be used to introduce rotation only locally, which in turn leads to a localised distribution of vortices in the BEC [163–167]. In this work I consider the effect of an inhomogeneous artificial gauge field on a two-component condensate and focus, in particular, on its effect on the phase separation transition. As the rotational energy is inhomogeneously distributed in the condensates, the presence of the gauge field will lead to a symmetry breaking in the separated density distribution.

One of the most interesting features of a BEC is that, under certain circumstances, the interaction between the evanescent field and the condensate atoms creates an ar-

tificial gauge field for the condensate. Several previous investigations into this have shown that the condensate responds to this by picking up some angular momentum and consequently forming vortices, albeit in a non-homogeneous manner [165–167]. In the following, I will extend the existing works by considering the effect of the non-homogeneous artificial gauge fields on interacting two-component condensates, and in particular the phase separation transition in such systems. Artificial gauge fields for neutral atoms can be created in various different ways [163–166, 168], with one of them being the exposure of the atoms to a strong, optical intensity gradient. Evanescent fields are a good candidate for this and in this work I will consider condensates that are close to the surface of a dielectric prism. While condensates are fundamentally many-body systems, which can require complex many-body models for their description, the low-density condensates that I consider can be treated with the well-established mean-field approach of the Gross-Pitaevskii framework [169]. In this, each condensate component is described by a macroscopic wavefunction whose evolution is determined by a non-linear Schrödinger equation and the coupling between different components is accounted for by a density-density term. Since this is a highly non-linear system, I use a numerical approach that is complemented by analytical studies in certain limits. The results of this project have been published as Phys. Rev. A **102**, 053309 (2020) and selected as "Editor's Suggestion".

## 5.2 Mathematical model and artificial gauge fields

I consider an interacting two-component BEC of neutral alkali atoms with wavefunctions  $\phi_1$  and  $\phi_2$  trapped in a harmonic potential  $V(x, z)$  above the surface of a dielectric prism with the refractive index  $n$  (see Fig. 5.1). The atoms of both components have an identical internal two-level structure with atomic energies  $\hbar\omega_1$  and  $\hbar\omega_2$ , and interact with the evanescent field emerging from the surface of the dielectric prism. The light traversing the prism has the frequency  $\omega_L$  and is assumed to be close to the resonance frequency of the atoms.

To reduce the large number of degrees of freedom that the two-component systems possess, I assume that both condensates are trapped in the same harmonic potential ( $\omega_A = \omega_B$ ), and that the trap is symmetric in the  $x - z$  plane, i. e. the trapping frequencies are the same in both directions ( $\omega_x = \omega_z = \omega$ ). In addition, I assume that the number of atoms in each condensate is equal and conserved ( $N_1 = N_2 = N$ ) and both components have the same mass  $M$ , which can be achieved by trapping a single species and condensing the atoms in two different internal states. Since the fundamental nature of vortices already appears in two-dimensions, all calculations are restricted to this lower dimensional space.

Since the interacting, two-component BEC is located in the vicinity of a dielectric prism, the atoms feel the effect of the evanescent field emerging from the prism due to their electric dipole moments,  $\mathbf{d}$ , via the dipole interaction  $\mathbf{d} \cdot \mathbf{E}$ . The presence of the evanescent field at the position of each atom leads to the appearance of dressed states

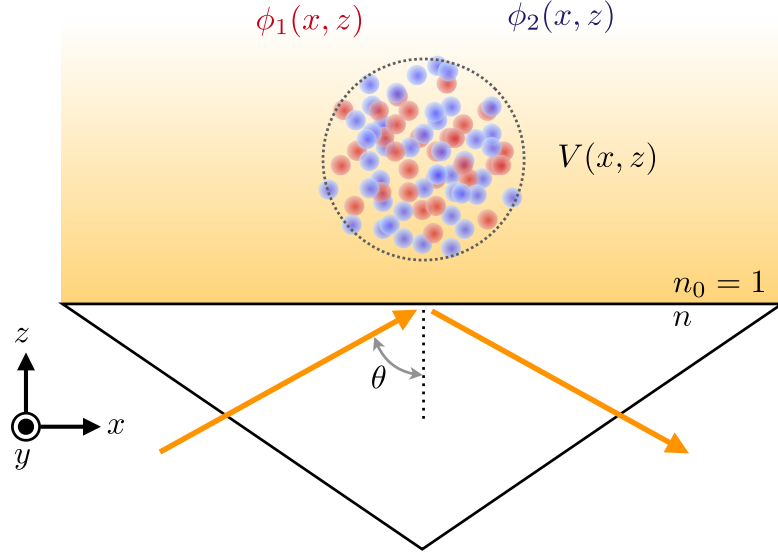


**Figure 5.1:** Schematic representation of a two-component BEC trapped in a potential  $V(x, z)$  (geometry indicated by the dashed circle) just above the surface of a dielectric prism.[4]

and one of the dressed states is given by [165]

$$|\chi(x, z)\rangle = \begin{pmatrix} \cos[\Phi(z)/2] \\ \sin[\Phi(z)/2]e^{-i\phi(x)} \end{pmatrix}, \quad (5.1)$$

where the relative phase  $\phi(x) = xk_0n \sin \theta$  depends on the wave vector  $k_0$  as well as on the incident angle  $\theta$ . Also  $\Phi(z) = \arctan\left(\frac{|\kappa(x, z)|}{\Delta}\right)$  depends on  $\kappa(\mathbf{r}) = \mathbf{d} \cdot \mathbf{E}(\mathbf{r})/\hbar$  and the detuning from the resonance frequency  $\Delta = \omega_L - \omega_A$  [170]. For simplicity, the parameter  $s$  is defined as [165]

$$s = \frac{|\mathbf{d} \cdot \mathbf{E}(\mathbf{r})|}{\hbar|\Delta|}. \quad (5.2)$$

The artificial gauge field can be calculated from the above dressed state as  $\mathbf{A} = i\hbar\langle\chi|\nabla\chi\rangle$  and when the artificial magnetic field  $B = \nabla \times \mathbf{A}$  is nonzero, the vector potential can not be eliminated from the Hamiltonian by a gauge transformation.

To obtain the ground state of this system, one needs to solve two coupled Gross-Pitaevskii equations. In the presence of the gauge field the standard momentum operator  $\mathbf{P}$  needs to be replaced by a generalized momentum  $[\mathbf{P} - \mathbf{A}]$  and therefore the two coupled equations of motion of the system are given by

$$\begin{aligned} i\hbar\frac{\partial\phi_1}{\partial t} &= \frac{1}{2m}\left(\mathbf{P}_1 - \mathbf{A}\right)^2\phi_1 + \frac{1}{2}m\omega^2(x^2 + y^2)\phi_1 + g_{11}|\phi_1|^2\phi_1 + g_{12}|\phi_2|^2\phi_1, \\ i\hbar\frac{\partial\phi_2}{\partial t} &= \frac{1}{2m}\left(\mathbf{P}_2 - \mathbf{A}\right)^2\phi_2 + \frac{1}{2}m\omega^2(x^2 + y^2)\phi_2 + g_{22}|\phi_2|^2\phi_2 + g_{21}|\phi_1|^2\phi_2. \end{aligned} \quad (5.3)$$

In the above equations,  $g_{11}$  and  $g_{22}$  account for the intra-component interaction strengths and  $g_{12} = g_{21}$  is the inter-component interaction strength. In free space the ratio between intra-component interaction and inter-component interaction determines if the two component are in a miscible or phase separated state: if  $g_{12}^2 < g_{11}g_{22}$  the system is miscible, and once this inequality is violated, the system phase separates. However, in a trap and in the presence of rotation, the above criterion needs to be adjusted and the final, phase separated distribution will have to take into account the minimization of the additional energy terms relating to these additional effects. This can lead to phase-separated states that break the symmetries that are otherwise inherent in the Hamiltonian. The presence of an inhomogeneous gauge fields is one example where this appears.

### 5.3 Publication

S. Sahar S. Hejazi, J. Polo, R. Sachdeva, and Th. Busch. Symmetry breaking in binary Bose-Einstein condensates in the presence of an inhomogeneous artificial gauge field. *Phys. Rev. A* **102**, 053309 (2020).

### 5.4 Results and conclusions

The artificial gauge field produced from the atom light interaction in the vicinity of the prism has a position dependence (see Eq. (4) in *Phys. Rev. A* **102**, 053309 (2020)). Due to this inhomogeneity, both condensates carry a localised vortex line in the miscible regime (see Fig. 3(a)), and the position of this line plays a substantial role in determining how the two components separate in the immiscible regime. However, while both condensate show the same behaviour in the miscible phase, in the immiscible regime the condensates spontaneously break symmetry and separate into an asymmetric state (see Fig. 3(b)). To have a clear understanding of this mechanism and obtain a qualitative explanation of the fundamental concepts behind the occurrence of the symmetry breaking, I use a simplified toy model, where the spatial dependence of the artificial gauge field is given by a Heaviside step function  $\mathbf{A}_\Theta(z) = A_0\Theta(-z + z_0)$ . This model allows to separate out the importance of the different contributions to the overall energy of the system as they change when the vortex lines moves through the high density areas of the condensates. The results have been published as *Phys. Rev. A* **102**, 053309 (2020).



# Conclusion

The work presented in this thesis has been focused on examining several aspects of the coupling between evanescent electromagnetic fields and cold atoms. A number of different phenomena that can appear have been discussed, such as creating channeling between atoms through the surface modes of the dielectric, enhancing the spontaneous emission of an atom, allowing directional emission and consequently the appearance of a chiral force, and finally symmetry breaking within a coupled Bose-Einstein condensate.

I first introduced two well-known methods to solve inhomogeneous differential equations, the mode function method and the Green's function method. These techniques can be used to study situations where one or two atoms interact with an electromagnetic field in the presence of a dielectric medium.

In Chapter 3, I presented an example of how to use the mode function method to calculate the decay rate of two two-level atoms close to a dielectric half-plate. Here atomic dipole matrix element of atoms can be complex vectors, this leads to few interesting phenomena such as oscillatory behaviour of decay rate in addition to directional dependence of it. The decay rates into the surface modes were shown to decrease as the atoms were moving away from the dielectric medium, while oscillatory behaviour was found for emission into the radiation modes due to interference of modes. For situations where the dipole moments were complex an asymmetry in the emission rate was observed and this chirality was quantified by calculating the asymmetry factor. This study laid the foundations to study various other systems, starting from the decay rate of multi-level atoms in the vicinity of ultra-thin optical nanofiber which support higher-order modes, to exploring the chirality of the recoil force after a directed spontaneous emission.

The results relating to the first of these last two projects were presented in Chapter 4. Here I expanded the previous work to the different geometry given by a nanofiber and studied the channeling of spontaneous emission from a multi-level atom into the optical modes of this fiber. I was able to show that, in particular, the spontaneous emission rate depends on the hyperfine level of the atom and on the optical modes of nanofiber.

To calculate the force of light on an atom stemming from a chiral emission of a photon, I used two different methods. The mode-function method allowed to determine the force in the direction of the optical propagation axis, while the Green's function methods allowed me to fully describe the force in all three spatial directions.

Finally, I studied the many-body system given by a Bose-Einstein condensate in the vicinity of a dielectric prism. The evanescent field of prism interacts with the BEC to create an artificial gauge field, which has position dependence due to exponential

decay characteristic of the evanescent field. This leads to the appearance of a position dependence of the vortex structure. In this study, I explored how this inhomogeneous distribution of angular momentum energy leads to a symmetry breaking in the phase-separated regime of a two components BEC.

# Bibliography

- [1] F. Le Kien, S. Sahar S. Hejazi, Th. Busch, V. G. Truong, and S. Nic Chormaic. Channeling of spontaneous emission from an atom into the fundamental and higher-order modes of a vacuum-clad ultrathin optical fiber. *Phys. Rev. A*, 96:043859, Oct 2017.
- [2] F. Le Kien, S. Sahar S. Hejazi, V. G. Truong, S. Nic Chormaic, and Th. Busch. Chiral force of guided light on an atom. *Phys. Rev. A*, 97:063849, 2018.
- [3] F. Le Kien, D. F. Kornovan, S. Sahar S. Hejazi, V. G. Truong, M. I. Petrov, S. Chormaic, and Th. Busch. Force of light on a two-level atom near an ultrathin optical fiber. *New J. Phys.*, 20(9):093031, 2018.
- [4] S. Sahar S. Hejazi, J. Polo, R. Sachdeva, and Th. Busch. Symmetry breaking in binary Bose-Einstein condensates in the presence of an inhomogeneous artificial gauge field. *Phys. Rev. A*, 102(5):053309, 2020.
- [5] FOSCO. Fiber dispersion and optical dispersion – an overview. [http://hank.uoregon.edu/wiki/index.php/Fiber\\_Optics](http://hank.uoregon.edu/wiki/index.php/Fiber_Optics). Accessed: 2017-06-26.
- [6] M. J. Morrissey, K. Deasy, M. Frawley, R. Kumar, E. Prel, L. Russell, V. G. Truong, and S. Nic Chormaic. Spectroscopy, manipulation and trapping of neutral atoms, molecules, and other particles using optical nanofibers: A review. *Sensors*, 13:10449 – 10481, 2013.
- [7] C. D. Mellor and C. D. Bain. Array formation in evanescent waves. *Chem. Phys. Chem.*, 7(2):329 – 332, 2006.
- [8] F. Le Kien and A. Rauschenbeutel. Spontaneous emission of a two-level atom with an arbitrarily polarized electric dipole in front of a flat dielectric surface. *Phys. Rev. A*, 93:043828, 2016.
- [9] K. Iizuka. *Elements of Photonics, Volume I: In Free Space and Special Media*, volume 41. John Wiley & Sons, 2002.
- [10] A. Günther, M. Kemmler, S. Kraft, C. J. Vale, C. Zimmermann, and J. Fortágh. Combined chips for atom optics. *Phys. Rev. A*, 71:063619, 2005.
- [11] P. Treutlein, P. Hommelhoff, T. Steinmetz, Th. W. Hänsch, and J. Reichel. Coherence in microchip traps. *Phys. Rev. Lett.*, 92:203005, 2004.

- [12] J. Fortágh and C. Zimmermann. Magnetic microtraps for ultracold atoms. *Rev. Mod. Phys.*, 79:235 – 289, 2007.
- [13] J. Reichel and V. Vuletic. *Atom Chips*. Wiley, 2011.
- [14] D. R. Leibbrandt. *Integrated chips and optical cavities for trapped ion quantum information processing*. PhD thesis, University of Michigan, 2009.
- [15] F. London. On centers of Van der Waals attraction. *The Journal of Physical Chemistry*, 46(2):305 – 316, 1942.
- [16] H. C. Hamaker. The London—van der Waals attraction between spherical particles. *Physica*, 4(10):1058 – 1072, 1937.
- [17] E. M. Lifshitz. The theory of molecular attractive forces between solids. *Sov. Phys. JETP*, 2:73 – 83, 1956.
- [18] J. Bardeen. The image and Van der Waals forces at a metallic surfaces. *Phys. Rev.*, 58(727), 1940.
- [19] J. E. Lennard-Jones. Process adsorption and diffusion on solid surfaces. *Trans. Faraday Soc.*, 28:333–359, 1932.
- [20] H. B. G. Casimir. On the attraction between two perfectly conducting plates. *Indag. Math.*, 10:261 – 263, 1948.
- [21] G. Barton. On the fluctuations of the Casimir forces. II. The stress-correlation function. *Journal of Physics A: Mathematical and General*, 24(23):5533, 1991.
- [22] U. Mohideen and A. Roy. Precision measurement of the Casimir force from 0.1 to 0.9 $\mu\text{m}$ . *Phys. Rev. Lett.*, 81:4549 – 4552, 1998.
- [23] U. Mohideen and A. Roy. Mohideen and roy reply. *Phys. Rev. Lett.*, 83, 1999.
- [24] A. W. Rodriguez, F. Capasso, and S. G. Johnson. The casimir effect in microstructured geometries. *Nature photonics*, 5(4):211–221, 2011.
- [25] H. B. G. Casimir and D. Polder. The influence of retardation on the London-van der Waals forces. *Phys. Rev.*, 73:360 – 372, 1948.
- [26] A. Lambrecht. The Casimir effect: a force from nothing. *Physics World*, 15(9):29, 2002.
- [27] E. V. Teodorovich. On the contribution of macroscopic Van Der Waals interactions to frictional force. *Proceedings of the Royal Society of London A: Mathematical, Physical and Engineering Sciences*, 362(1708):71 – 77, 1978.
- [28] J. B. Pendry. Quantum friction—fact or fiction? *New J. Phys*, 12(3):033028, 2010.
- [29] U. Leonhardt. Comment on "Quantum Friction – Fact or Fiction?". *New J. Phys*, 12(6):068001, 2010.

- 
- [30] B. N. J. Persson, F. Bucher, and B. Chiaia. Elastic contact between randomly rough surfaces: Comparison of theory with numerical results. *Phys. Rev. B*, 65:184106, 2002.
- [31] A. I. Volokitin and B. N. J. Persson. Quantum friction. *Phys. Rev. Lett.*, 106:094502, 2011.
- [32] S. A. Fulling and P. C. W. Davies. Radiation from a moving mirror in two dimensional space-time: Conformal anomaly. *Proceedings of the Royal Society of London A: Mathematical, Physical and Engineering Sciences*, 348(1654):393 – 414, 1976.
- [33] E. M. Purcell, H. C. Torrey, and R. V. Pound. Resonance absorption by nuclear magnetic moments in a solid. *Phys. Rev.*, 69:37 – 38, 1946.
- [34] R. P. Feynman. Nobel lecture: The development of the space-time view of quantum electrodynamics. 114, 1965.
- [35] R. P. Feynman. *QED: The Strange Theory of Light and Matter*. Princeton University Press, 1988.
- [36] W. Dittrich and H. Gies. *Probing the Quantum Vacuum*. Springer, 2000.
- [37] M. Revzen. Quantum fluctuation theory. *Phys. Lett. A*, 29(8):443 – 444, 1969.
- [38] P. A. M. Dirac. The quantum theory of the emission and absorption of radiation. *Proceedings of the Royal Society of London A: Mathematical, Physical and Engineering Sciences*, 114(767):243 – 265, 1927.
- [39] P. W. Milonni. Why spontaneous emission? *American Journal of Physics*, 52(4):340 – 343, 1984.
- [40] S. R. Zhao, C. P. Sun, and W. X. Zhang. Exact analytical approach for spontaneous emission of atoms in the optical potential theory. *Phys. Lett. A*, 207(6):327 – 332, 1995.
- [41] W. E. Lamb and R. C. Retherford. Fine structure of the hydrogen atom by a microwave method. *Phys. Rev.*, 72:241 – 243, 1947.
- [42] T. A. Welton. Some observable effects of the quantum-mechanical fluctuations of the electromagnetic field. *Phys. Rev.*, 74:1157 – 1167, 1948.
- [43] A. Lambrecht. Electromagnetic pulses from a cavity moving in vacuum : possible experiments. *Annales de la Fondation Louis de Broglie.*, 29(1-2), 2004.
- [44] F. Le Kien, S. Dutta Gupta, K. P. Nayak, and K. Hakuta. Nanofiber-mediated radiative transfer between two distant atoms. *Phys. Rev. A*, 72(6):063815, 2005.
- [45] F. Le Kien, S. Dutta Gupta, V. I. Balykin, and K. Hakuta. Spontaneous emission of a cesium atom near a nanofiber: Efficient coupling of light to guided modes. *Phys. Rev. A*, 72:032509, 2005.

- [46] Q. Z. Yuan, C. H. Yuan, and W. Zhang. Near-surface effect on interatomic resonance interaction. *Phys. Rev. A*, 93:032517, 2016.
- [47] J. Petersen, J. Volz, and A. Rauschenbeutel. Chiral nanophotonic waveguide interface based on spin-orbit interaction of light. *Science*, 346(6205):67 – 71, 2014.
- [48] F. Le Kien and A. Rauschenbeutel. Anisotropy in scattering of light from an atom into the guided modes of a nanofiber. *Phys. Rev. A*, 90(2):023805, 2014.
- [49] R. Mitsch, C. Sayrin, B. Albrecht, P. Schneeweiss, and A. Rauschenbeutel. Quantum state-controlled directional spontaneous emission of photons into a nanophotonic waveguide. *Nature communications*, 5(1):1 – 5, 2014.
- [50] S. Scheel, S. Y. Buhmann, C. Clausen, and Ph. Schneeweiss. Directional spontaneous emission and lateral Casimir-Polder force on an atom close to a nanofiber. *Phys. Rev. A*, 92(4):043819, 2015.
- [51] F. Kalhor, Th. Thundat, and Z. Jacob. Universal spin-momentum locked optical forces. *Applied Physics Letters*, 108(6):061102, 2016.
- [52] B. Lee. Review of the present status of optical fiber sensors. *Optical Fiber Technology*, 9(2):57 – 79, 2003.
- [53] S. Yin and P. Ruffin. *Fiber Optic Sensors*. John Wiley and Sons, Inc., 2006.
- [54] J. Bures and R. Ghosh. Power density of the evanescent field in the vicinity of a tapered fiber. *JOSA A*, 16(8):1992 – 1996, 1999.
- [55] L. Tong, J. Lou, and E. Mazur. Single-mode guiding properties of subwavelength-diameter silica and silicon wire waveguides. *Optics Express*, 12(6):1025 – 1035, 2004.
- [56] F. Le Kien, J.Q. Liang, K. Hakuta, and V. I. Balykin. Field intensity distributions and polarization orientations in a vacuum-clad subwavelength-diameter optical fiber. *Optics Communications*, 242(4-6):445 – 455, 2004.
- [57] L. Tong. Brief introduction to optical microfibers and nanofibers. *Frontiers of Optoelectronics in China*, 3(1):54 – 60, 2010.
- [58] L. Tong, R. R. Gattass, J. B. Ashcom, S. He, J. Lou, M. Shen, I. Maxwell, and E. Mazur. Subwavelength-diameter silica wires for low-loss optical wave guiding. *Nature*, 426(6968):816 – 819, 2003.
- [59] T. A. Birks, W. J. Wadsworth, and P. St J. Russell. Supercontinuum generation in tapered fibers. *Optics letters*, 25(19):1415 – 1417, 2000.
- [60] S. G. Leon-Saval, T. A. Birks, W. J. Wadsworth, P. St J. Russell, and M. W. Mason. Conference on lasers and electro-optics (CLEO). 2004.

- 
- [61] J. C. Knight, G. Cheung, F. Jacques, and T. A. Birks. Phase-matched excitation of whispering-gallery-mode resonances by a fiber taper. *Optics letters*, 22(15):1129 – 1131, 1997.
- [62] M. Cai and K. Vahala. Highly efficient hybrid fiber taper coupled microsphere laser. pages 114 – 116, 2001.
- [63] J. D. Love, W. M. Henry, W. J. Stewart, R. J. Black, S. Lacroix, and F. Gonthier. Tapered single-mode fibres and devices. i. adiabaticity criteria. *IEE Proceedings J - Optoelectronics*, 138(5):343 – 354, 1991.
- [64] J. M. Ward, A. Maimaiti, Vu H. Le, and S. Nic Chormaic. Contributed review: Optical micro- and nanofiber pulling rig. *Review of Scientific Instruments*, 85(11):111501, 2014.
- [65] T. A. Birks and Y. W. Li. The shape of fiber tapers. *Journal of Lightwave Technology*, 10(4):432 – 438, 1992.
- [66] R. P. Kenny, T. A. Birks, and K. P. Oakley. Control of optical fibre taper shape. *Electronics Letters*, 27(18):1654 – 1656, 1991.
- [67] F. Orucevic, V. Lefèvre-Seguin, and J. Hare. Transmittance and near-field characterization of sub-wavelength tapered optical fibers. *Opt. Express*, 15(21):13624 – 13629, 2007.
- [68] T. E. Dimmick, G. Kakarantzas, T. A. Birks, and P. St. J. Russell. Carbon dioxide laser fabrication of fused-fiber couplers and tapers. *Appl. Opt.*, 38(33):6845 – 6848, 1999.
- [69] A. J. C. Grellier, N. K. Zayer, and C. N. Pannell. Heat transfer modelling in co2 laser processing of optical fibres. *Optics Communications*, 152(4):324 – 328, 1998.
- [70] G. Brambilla, Y. Jung, and F. Renna. Optical fiber microwires and nanowires manufactured by modified flame brushing technique: properties and applications. *Frontiers of Optoelectronics in China*, 3(1):61–66, 2010.
- [71] F. Bilodeau, K. O. Hill, S. Faucher, and D. C. Johnson. Low-loss highly over-coupled fused couplers: fabrication and sensitivity to external pressure. *Journal of Lightwave Technology*, 6(10):1476–1482, 1988.
- [72] R. R. Tong, J. B. Gattass, and S. He Ashcom. J. lou, m. shen, i. maxwell, and e. mazur. *Nature*, 426:816, 2003.
- [73] J. D. Love and W. M. Henry. Quantifying loss minimisation in single-mode fibre tapers. *Electronics Letters*, 22(17):912–914, 1986.
- [74] F. W. Sheu and Y. S. Huang. Trapping and propelling microparticles at long range by using an entirely stripped and slightly tapered no-core optical fiber. *Sensors*, 13(3):2884–2894, 2013.

- [75] C. Xu, H. Lei, Y. Zhang, and B. Li. Backward transport of nanoparticles in fluidic flow. *Opt. Express*, 20(3):1930–1938, 2012.
- [76] A. Goban, K. S. Choi, D. J. Alton, D. Ding, C. Lacroûte, M. Pototschnig, T. Thiele, N. P. Stern, and H. J. Kimble. Demonstration of a state-insensitive, compensated nanofiber trap. *Phys. Rev. Lett.*, 109(3):033603, 2012.
- [77] E. Vetsch, D. Reitz, G. Sagué, R. Schmidt, S. T. Dawkins, and A. Rauschenbeutel. Optical interface created by laser-cooled atoms trapped in the evanescent field surrounding an optical nanofiber. *Phys. Rev. Lett.*, 104(20):203603, 2010.
- [78] V. I. Balykin, K. Hakuta, F. Le Kien, J. Q. Liang, and M. Morinaga. Atom trapping and guiding with a subwavelength-diameter optical fiber. *Phys. Rev. A*, 70(1):011401, 2004.
- [79] F. Le Kien, V. I. Balykin, and K. Hakuta. Atom trap and waveguide using a two-color evanescent light field around a subwavelength-diameter optical fiber. *Phys. Rev. A*, 70(6):063403, 2004.
- [80] P. Domokos, P. Horak, and H. Ritsch. Quantum description of light-pulse scattering on a single atom in waveguides. *Phys. Rev. A*, 65(3):033832, 2002.
- [81] F. Le Kien, V. I. Balykin, and K. Hakuta. Scattering of an evanescent light field by a single cesium atom near a nanofiber. *Phys. Rev. A*, 73(1):013819, 2006.
- [82] K. P. Nayak, P. N. Melentiev, M. Morinaga, F. Le Kien, V. I. Balykin, and K. Hakuta. Optical nanofiber as an efficient tool for manipulating and probing atomic fluorescence. *Optics express*, 15(9):5431 – 5438, 2007.
- [83] K. P. Nayak, F. Le Kien, M. Morinaga, and K. Hakuta. Antibunching and bunching of photons in resonance fluorescence from a few atoms into guided modes of an optical nanofiber. *Phys. Rev. A*, 79(2):021801, 2009.
- [84] M. J. Morrissey, K. Deasy, Y. Wu, S. Chakrabarti, and S. Nic Chormaic. Tapered optical fibers as tools for probing magneto-optical trap characteristics. *Review of scientific instruments*, 80(5):053102, 2009.
- [85] S. T. Dawkins, R. Mitsch, D. Reitz, E. Vetsch, and A. Rauschenbeutel. Dispersive optical interface based on nanofiber-trapped atoms. *Phys. rev. lett.*, 107(24):243601, 2011.
- [86] D. Reitz, C. Sayrin, R. Mitsch, P. Schneeweiss, and A. Rauschenbeutel. Coherence properties of nanofiber-trapped cesium atoms. *Phys. rev. lett.*, 110(24):243603, 2013.
- [87] L. Russell, R. Kumar, V. B. Tiwari, and S. Nic Chormaic. Measurements on release–recapture of cold  $85\text{Rb}$  atoms using an optical nanofibre in a magneto-optical trap. *Optics Communications*, 309:313 – 317, 2013.



- 
- [88] R. Kumar, V. Gokhroo, V. B. Tiwari, and S. Nic Chormaic. Temperature measurement of cold atoms using transient absorption of a resonant probe through an optical nanofibre. *Journal of Optics*, 18(11):115401, 2016.
- [89] A. Stiebeiner, O. Rehband, R. Garcia-Fernandez, and A. Rauschenbeutel. Ultra-sensitive fluorescence spectroscopy of isolated surface-adsorbed molecules using an optical nanofiber. *Optics Express*, 17(24):21704 – 21711, 2009.
- [90] R. Yalla, F. Le Kien, M. Morinaga, and K. Hakuta. Efficient channeling of fluorescence photons from single quantum dots into guided modes of optical nanofiber. *Phys. Rev. Lett.*, 109(6):063602, 2012.
- [91] T. Schröder, M. Fujiwara, T. Noda, Hong-Quan Zhao, O. Benson, and Sh. Takeuchi. A nanodiamond-tapered fiber system with high single-mode coupling efficiency. *Optics express*, 20(10):10490 – 10497, 2012.
- [92] L. Liebermeister, F. Petersen, A. v Münchow, D. Burchardt, J. Hermelbracht, T. Tashima, A. W. Schell, O. Benson, Th. Meinhardt, A. Krueger, et al. Tapered fiber coupling of single photons emitted by a deterministically positioned single nitrogen vacancy center. *App. Phys. Lett.*, 104(3):031101, 2014.
- [93] S. E. Skelton, M. Sergides, R. Patel, E. Karczewska, O. M. Maragó, and P. H. Jones. Evanescent wave optical trapping and transport of micro-and nanoparticles on tapered optical fibers. *Journal of Quantitative Spectroscopy and Radiative Transfer*, 113(18):2512 – 2520, 2012.
- [94] G. Brambilla, G. Senthil Murugan, J. S. Wilkinson, and D. J. Richardson. Optical manipulation of microspheres along a subwavelength optical wire. *Optics letters*, 32(20):3041 – 3043, 2007.
- [95] F. Le Kien and A. Rauschenbeutel. Negative azimuthal force of nanofiber-guided light on a particle. *Phys. Rev. A*, 88(6):063845, 2013.
- [96] J. P. Burke, Sai-Tak Chu, G. W. Bryant, C. J. Williams, and P. S. Julienne. Designing neutral-atom nanotraps with integrated optical waveguides. *Phys. Rev. A*, 65:043411, 2002.
- [97] Y. B. Ovchinnikov, S. V. Shul’ga, and V. I. Balykin. An atomic trap based on evanescent light waves. *Journal of Physics B: Atomic, Molecular and Optical Physics*, 24(14):3173, 1991.
- [98] C. Lacroûte, K. S. Choi, A. Goban, D. J. Alton, D. Ding, N. P. Stern, and H. J. Kimble. A state-insensitive, compensated nanofiber trap. *New J. Phys.*, 14(2):023056, 2012.
- [99] M. C. Frawley, A. Petcu-Colan, V. G. Truong, and S. Nic Chormaic. Higher order mode propagation in an optical nanofiber. *Optics Communications*, 285(23):4648 – 4654, 2012.

- [100] S. Ravets, J. E. Hoffman, L. A. Orozco, S. L. Rolston, G. Beadie, and F. K. Fatemi. A low-loss photonic silica nanofiber for higher-order modes. *Opt. Express*, 21(15):18325 – 18335, 2013.
- [101] H. J. Butt, K. Graf, and M. Kappl. *Physics and chemistry of interfaces*. John Wiley & Sons, 2013.
- [102] L. Van Der Sneppen, C. Gooijer, W. Ubachs, and F. Ariese. Evanescent-wave cavity ring-down detection of cytochrome c on surface-modified prisms. *Sensors and Actuators B: Chemical*, 139(2):505 – 510, 2009.
- [103] D. Axelrod. Cell-substrate contacts illuminated by total internal reflection fluorescence. *Journal of Cell Biology*, 89(1):141 – 145, 1981.
- [104] D. Axelrod. Total internal reflection fluorescence microscopy in cell biology. *Traffic*, 2(11):764 – 774, 2001.
- [105] S. Kawata and T. Sugiura. Movement of micrometer-sized particles in the evanescent field of a laser beam. *Optics letters*, 17(11):772 – 774, 1992.
- [106] M. Oheim and F. Schapper. Non-linear evanescent field imaging. *Journal of Physics D: Applied Physics*, 38(10):R185, 2005.
- [107] E. Betzig and J. K. Trautman. Near-field optics: Microscopy, spectroscopy, and surface modification beyond the diffraction limit. *Science*, 257(5067):189 – 195, 1992.
- [108] M. Gu and P. Chun Ke. Effect of depolarization of scattered evanescent waves on particle-trapped near-field scanning optical microscopy. *App. Phys. Lett.*, 75(2):175 – 177, 1999.
- [109] D. Ganic, X. Gan, and M. Gu. Near-field imaging by a micro-particle: a model for conversion of evanescent photons into propagating photons. *Opt. Express*, 12(22):5325 – 5335, 2004.
- [110] T. Čižmár, M. Šiler, M. Šerý, P. Zemánek, V. Garcés-Chávez, and K. Dholakia. Optical sorting and detection of submicrometer objects in a motional standing wave. *Phys. Rev. B*, 74:035105, 2006.
- [111] M. Lester and M. Nieto-Vesperinas. Optical forces on microparticles in an evanescent laser field. *Opt. Lett.*, 24(14):936 – 938, 1999.
- [112] D. E. Chang, J. S. Douglas, A. González-Tudela, C. L. Hung, and H. J. Kimble. Colloquium: Quantum matter built from nanoscopic lattices of atoms and photons. *Reviews of Modern Physics*, 90(3):031002, 2018.
- [113] D. E. Chang, L. Jiang, A. V. Gorshkov, and H. J. Kimble. Cavity QED with atomic mirrors. *New J. Phys.*, 14(6):063003, 2012.

- 
- [114] P. Lodahl, S. Mahmoodian, S. Stobbe, A. Rauschenbeutel, Ph. Schneeweiss, J. Volz, H. Pichler, and P. Zoller. Chiral quantum optics. *Nature*, 541(7638):473 – 480, 2017.
- [115] S. Barik, A. Karasahin, C. Flower, T. Cai, H. Miyake, W. De Gottardi, M. Hafezi, and E. Waks. A topological quantum optics interface. *Science*, 359(6376):666 – 668, 2018.
- [116] J. D. Jackson. *Classical Electrodynamics*. Wiley, 3rd ed. edition, 1999.
- [117] M. Born and E. Wolf. *Principles of Optics*. Cambridge University Press, 7 edition, 1999.
- [118] O. Di Stefano, S. Savasta, and R. Girlanda. Three-dimensional electromagnetic field quantization in absorbing and dispersive bounded dielectrics. *Phys. Rev. A*, 61:023803, 2000.
- [119] D. Marcuse. *Light Transmission Optics*. Krieger, Malabar, FL, 1989.
- [120] A. W. Snyder and J. D. Love. *Optical Waveguide Theory*. Chapman and Hall, New York, 1983.
- [121] K. Okamoto. *Fundamentals of Optical Waveguides*. Elsevier, New York, 2006.
- [122] T. Søndergaard and B. Tromborg. General theory for spontaneous emission in active dielectric microstructures: Example of a fiber amplifier. *Phys. Rev. A*, 64(3):033812, 2001.
- [123] C. T. Tai. *Dyadic Green functions in electromagnetic theory*. Institute of Electrical & Electronics Engineers (IEEE), 1994.
- [124] G. L. Klimchitskaya, U. Mohideen, and V. M. Mostepanenko. The casimir force between real materials: Experiment and theory. *Rev. Mod. Phys.*, 81:1827 – 1885, 2009.
- [125] H. Hoinkes. The physical interaction potential of gas atoms with single-crystal surfaces, determined from gas-surface diffraction experiments. *Rev. Mod. Phys.*, 52:933 – 970, 1980.
- [126] F. Le Kien and A. Rauschenbeutel. Nanofiber-mediated chiral radiative coupling between two atoms. *Phys. Rev. A*, 95:023838, 2017.
- [127] V. Weisskopf and E. P. Wigner. Calculation of the natural brightness of spectral lines on the basis of Dirac’s theory. *Z. Phys.*, 63:54 – 73, 1930.
- [128] L. Allen and J. H. Eberly. *Optical Resonance and Two-level Atoms*. Dover Publications, Inc., Mineola, NY, 1987.
- [129] H. Shibayama, A. Torii, K. Shibata, Y. Eto, H. Saito, and T. Hirano. Phase separation dynamics of two-component Bose-Einstein condensates in various optical trap shapes. In *JSAP-OSA Joint Symposia 2017 Abstracts*, pages 7–9. Optical Society of America, 2017.

- 
- [130] B. W. Shore. *The Coherent Theory of Atomic Excitation*. Wiley, New York, 1990.
- [131] V. V. Klimov and M. Ducloy. Spontaneous emission rate of an excited atom placed near a nanofiber. *Phys. Rev. A*, 69(1):013812, 2004.
- [132] S. Chang and V. Minogin. Density-matrix approach to dynamics of multilevel atoms in laser fields. *Physics Reports*, 365(2):65 – 143, 2002.
- [133] F. Le Kien, T. Ray, T. Nieddu, Th. Busch, and S. Nic Chormaic. Enhancement of the quadrupole interaction of an atom with the guided light of an ultrathin optical fiber. *Phys. Rev. A*, 97:013821, 2018.
- [134] W. B. Yan, W. Y. Ni, J. Zhang, F. Y. Zhang, and H. Fan. Tunable single-photon diode by chiral quantum physics. *Phys. Rev. A*, 98:043852, 2018.
- [135] D. Kornovan, M. Petrov, and I. Iorsh. Noninverse dynamics of a quantum emitter coupled to a fully anisotropic environment. *Phys. Rev. A*, 100:033840, 2019.
- [136] M. J. Mehl and W. L. Schaich. The Van der Waals interaction between an atom and a solid. *Surface Science*, 99(3):553 – 569, 1980.
- [137] A. M. Marvin and F. Toigo. Van der Waals interaction between a point particle and a metallic surface. I. Theory. *Phys. Rev. A*, 25(2):782, 1982.
- [138] M. Boustimi, J. Baudon, P. Candori, and J. Robert. Van der Waals interaction between an atom and a metallic nanowire. *Phys. Rev. B*, 65(15):155402, 2002.
- [139] M. Boustimi, J. Baudon, and J. Robert. Molecules interacting with a metallic nanowire. *Phys. Rev. B*, 67(4):045407, 2003.
- [140] C. Eberlein and R. Zietal. Force on a neutral atom near conducting microstructures. *Phys. Rev. A*, 75(3):032516, 2007.
- [141] C. Eberlein and R. Zietal. Retarded Casimir-Polder force on an atom near reflecting microstructures. *Phys. Rev. A*, 80(1):012504, 2009.
- [142] V. G. Minogin and S. Nic Chormaic. Manifestation of the Van der Waals surface interaction in the spontaneous emission of atoms into an optical nanofiber. *Laser Physics*, 20(1):32 – 37, 2010.
- [143] M. C. Frawley, S. Nic Chormaic, and V. G. Minogin. The Van der Waals interaction of an atom with the convex surface of a nanocylinder. *Physica Scripta*, 85(5):058103, 2012.
- [144] H. J. Metcalf and P. van der Straten. Laser cooling and trapping of atoms. *JOSA B*, 20(5):887 – 908, 2003.
- [145] H. J. Metcalf and P. Van der Straten. Laser cooling and trapping of neutral atoms. *The Optics Encyclopedia: Basic Foundations and Practical Applications*, 2007.

- 
- [146] V. I. Balykin, V. G. Minogin, and V. S. Letokhov. Electromagnetic trapping of cold atoms. *Reports on Progress in Physics*, 63(9):1429, 2000.
- [147] A. P. Kazantsev, G. I. Surdutovich, and V. P. Yakovlev. *Mechanical action of light on atoms*. World Scientific, 1990.
- [148] L. D. Barron. *Molecular light scattering and optical activity*. Cambridge University Press, 2009.
- [149] R. R. Q. P. T. Oude Weernink, P. Barcellona, and S. Y. Buhmann. Lateral Casimir-Polder forces by breaking time-reversal symmetry. *Phys. Rev. A*, 97(3):032507, 2018.
- [150] F. Le Kien, Th. Busch, V. G. Truong, and S. Nic Chormaic. Higher-order modes of vacuum-clad ultrathin optical fibers. *Phys. Rev. A*, 96(2):023835, 2017.
- [151] S. A. Hassani Gangaraj, G. W. Hanson, M. Antezza, and M. G. Silveirinha. Spontaneous lateral atomic recoil force close to a photonic topological material. *Phys. Rev. B*, 97(20):201108, 2018.
- [152] M. G. Silveirinha, S. A. Hassani Gangaraj, G. W. Hanson, and M. Antezza. Fluctuation-induced forces on an atom near a photonic topological material. *Phys. Rev. A*, 97(2):022509, 2018.
- [153] D. Barredo. S. d. léséleuc, v. lienhard, t. lahaye, and a. browaeys. *Science*, 354:1021, 2016.
- [154] M. Endres, H. Bernien, A. Keesling, H. Levine, E. R. Anschuetz, A. Krajenbrink, C. Senko, V. Vuletic, M. Greiner, and M. D. Lukin. Atom-by-atom assembly of defect-free one-dimensional cold atom arrays. *Science*, 354(6315):1024–1027, 2016.
- [155] M. Lewenstein, A. Sanpera, V. Ahufinger, B. Damski, A. Sen, and U. Sen. Ultracold atomic gases in optical lattices: mimicking condensed matter physics and beyond. *Advances in Physics*, 56(2):243 – 379, 2007.
- [156] I. Bloch, J. Dalibard, and W. Zwerger. Many-body physics with ultracold gases. *Rev. Mod. Phys.*, 80:885–964, 2008.
- [157] I. Bloch, J. Dalibard, and S. Nascimbene. Quantum simulations with ultracold quantum gases. *Nature Physics*, 8(4):267 – 276, 2012.
- [158] G. Thalhammer, G. Barontini, L. De Sarlo, J. Catani, F. Minardi, and M. Inguscio. Double species Bose-Einstein Condensate with tunable interspecies interactions. *Phys. Rev. Lett.*, 100:210402, 2008.
- [159] S. B. Papp, J. M. Pino, and C. E. Wieman. Tunable miscibility in a dual-species Bose-Einstein Condensate. *Phys. Rev. Lett.*, 101:040402, 2008.

- 
- [160] K. Kasamatsu and K. Sakashita. Stripes and honeycomb lattice of quantized vortices in rotating two-component Bose-Einstein condensates. *Phys. Rev. A*, 97:053622, 2018.
- [161] L. Mingarelli and R. Barnett. Exotic vortex lattices in binary repulsive superfluids. *Phys. Rev. Lett.*, 122:045301, 2019.
- [162] J. R. Abo-Shaeer, C. Raman, J. M. Vogels, and W. Ketterle. Observation of vortex lattices in Bose-Einstein Condensates. *Science*, 292(5516):476 – 479, 2001.
- [163] S. W. Su, S. C. Gou, I. K. Liu, I. B. Spielman, L. Santos, A. Acus, A. Mekys, J. Ruseckas, and G. Juzeliūnas. Position-dependent spin-orbit coupling for ultracold atoms. *New J. Phys.*, 17(3):033045, 2015.
- [164] V. E. Lembessis. Artificial gauge potentials for neutral atoms: an application in evanescent light fields. *J. Opt. Soc. Am. B*, 31(6):1322 – 1329, 2014.
- [165] M. Mochol and K. Sacha. Artificial magnetic field induced by an evanescent wave. *Scientific Reports*, 5(1):7672, 2015.
- [166] R. Sachdeva and Th. Busch. Creating superfluid vortex rings in artificial magnetic fields. *Phys. Rev. A*, 95:033615, 2017.
- [167] J. Schloss, P. Barnett, R. Sachdeva, and Th. Busch. Controlled creation of three-dimensional vortex structures in Bose-Einstein condensates using artificial magnetic fields. *Phys. Rev. A*, 102(4):043325, 2020.
- [168] V. E. Lembessis, A. Alqarni, S. Alshamari, A. Siddig, and O. M. Aldossary. Artificial gauge magnetic and electric fields for free two-level atoms interacting with optical Ferris wheel light fields. *J. Opt. Soc. Am. B*, 34(6):1122 – 1129, 2017.
- [169] C. J. Pethick and H. Smith. *Bose-Einstein condensation in dilute gases*. Cambridge university press, 2008.
- [170] J. Dalibard, F. Gerbier, G. Juzeliūnas, and P. Öhberg. Colloquium: Artificial gauge potentials for neutral atoms. *Rev. Mod. Phys.*, 83:1523–1543, 2011.